Programa de Doctorado en Ingeniería Matemática, Estadística e Investigación Operativa

por la

Universidad Complutense de Madrid

y la

Universidad Politécnica de Madrid

Numerical Simulations of Metallurgical Processes with a Lagrange-Galerkin Methodology

Tesis Doctoral

Mario Armando Freire Torres

Director

Jaime Carpio Huertas

Año

2023

UNIVERSIDAD POLITÉCNICA DE MADRID
Escuela Técnica Superior de Ingenieros Industriales

Doctoral Degree in Mathematical Engineering, Statistics and Operations Research

Numerical Simulations of Metallurgical Processes with a Lagrange-Galerkin Methodology

DOCTORAL THESIS

Submitted for the degree of Doctor by:

Mario Armando Freire Torres
Master of Mathematical Engineering and Computing

Under the supervision of:
Dr. Jaime Carpio Huertas

Madrid, 2023

Title: Numerical Simulations of Metallurgical Processes with a Lagrange-Galerkin Methodology

Author: Mario Armando Freire Torres

Doctoral Programme: Mathematical Engineering, Statistics and Operations Research

Thesis Supervision:

Dr. Jaime Carpio Huertas, Full Professor, Escuela Técnica Superior de Ingenieros Industriales - Universidad Politécnica de Madrid(Supervisor)

External Reviewers:

Thesis Defense Committee:

Thesis Defense Date:

This thesis has been partially supported by *Secretaría de Educación Superior, Ciencia, Tecnología e Innovación* of Republic of Ecuador for Doctoral Studies through official letter SENESCYT-SDFC-DSEFC-2017-3854-O (Award Resolution 106-2017).

A mi familia: Marujita, Marito, Mónica, Fernando, Andrea, Carlos y David.

Acknowledgement

First and foremost, I extend my deepest gratitude to my tutor and director, Dr. Jaime Carpio Huertas. His unwavering patience and insightful guidance throughout my doctoral journey were instrumental in shaping this thesis. I am particularly grateful for his encouragement during challenging moments and his meticulous revisions that helped me refine my arguments.

I also want to express my sincere appreciation to Dr. Manuel Colera Rico, for his invaluable data analysis support and critical feedback, which significantly strengthened my research.

Finally, my heartfelt gratitude to Dr. Salvador Jiménez Burillo, Coordinator of the Doctoral Program, for his invaluable guidance and support in navigating the program's bureaucratic complexities. His patience and expertise were instrumental in my success.

Abstract

In this work, we present a novel finite element method to resolve the thermal variables that develop in welding processes. The mathematical model developed is based on the formulation of the enthalpy within the energy conservation equation, which is simultaneously valid for solid, liquid and mixed (mushy region) phases. As part of the description of our work, two models were developed, one that is isothermal and the other non-isothermal, which were considered to correspondingly relate the enthalpy variable with the temperature variable. For greater precision in the description of the research work developed, quadratic triangular elements were used with the application of an anisotropic adaptive meshing for discretization in the space of the governing equation, and a BDF2 type scheme (Backward Differentiation Formula, of order 2), to achieve discretization in time. The system of equations of a non-linear nature can be solved by adapting a Newton-type algorithm, the two versions of which are detailed in this document, the θ-Newton algorithm, which considers the dimensionless temperature θ as the main variable to calculate. This approach is the most used by various authors in the literature. On the other hand, we have the h-Newton method, which considers the enthalpy h as the main variable to calculate. The main structure of this thesis lies in the latter.

In order to verify its validity, several experiments of a numerical nature were developed, where the robustness and efficiency of the h-Newton type method is tested, resulting in good convergence of the solution, both for isothermal and non-isothermal type fusion. On the other hand, it is worth mentioning that the θ-Newton type method can only be used in the case of non-isothermal fusion, and converges in the case of a high temperature range or a step small enough. The various numerical experiments developed showed that the developed method is capable of capturing discontinuities and sharp fronts in the solution without having to add any type of numerical dissipation. On the other hand, we verified in much more detail the convergence and efficiency of the constructed method, for which we carried out comparative tests with two of the most used methods in the literature, which work with thermomechanical models based on enthalpy. These are Bermúdez-Moreno and Nedjar.

The results show that our h-Newton method is much more efficient in terms of computational time. To achieve a more realistic model, we complete the method developed previously with the Navier-Stokes equations. These help us find the values of the velocity and pressure of both the liquid phase and the mixed phase. It is worth highlighting the inclusion of two terms of utmost importance to model both the phenomenon of natural convection and to model the phenomenon of the flow of the liquid zone through porous media. For our purpose, we use the Boussinesq model and the Darcy model, respectively. Finally, in the last part of this research, we develop an adaptation of our full enthalpy-based model to determine the various steel-phases that can be found in a heat treatment study for steel. This resulted in the appearance of the austenite, martensite, bainite, ferrite and pearlite phases, whose constitutions depend on the variable temperature.

Resumen

En este trabajo, presentamos un novedoso método de elementos finitos para resolver las variables térmicas que se desarrollan en los procesos de soldadura. El modelo matemático desarrollado está basado en la formulación de la entalpía dentro de la ecuación de conservación de la energía, la cual es simultáneamente válida tanto para las fases sólida, líquida y mixta (región blanda). Como parte de la descripción de nuestro trabajo, se desarrollaron dos modelos, isotérmico y no isotérmico, los cuales fueron considerados para relacionar correspondientemente la variable entalpía con la variable temperatura. Para mayor precisión en la descripción del trabajo de investigación desarrollado, se emplearon elementos triangulares cuadráticos con la aplicación de un mallado adaptativo anisótropo para la discretización en el espacio de la ecuación gobernante, y un esquema de tipo BDF2 (Fórmula de Diferenciación hacia atrás, de orden 2), para conseguir la discretización en el tiempo. El sistema de ecuaciones de naturaleza no lineal se pudo resolver mediante la adaptación de un algoritmo de tipo Newton, cuyas dos versiones se detallan en este documento, el algoritmo θ tipo Newton, el cual considera a la temperatura adimensional θ como la variable principal a calcular. Este enfoque es el más empleado por diversos autores dentro de la literatura. Por otro lado, tenemos al algoritmo h tipo Newton, el cual considera a la entalpía h como la variable principal a calcular. En este último radica la estructura principal de esta tesis.

Para comprobar su validez, se desarrollaron varios experimentos numéricos, donde se pudo comprobar la robustez y eficiencia del método h tipo Newton, dando como resultado la buena convergencia de la solución, tanto para fusión isotérmica como no isotérmica. Por otro lado, cabe mencionar que el método θ tipo Newton solamente puede ser empleado en el caso de fusión no isotérmica, y converge en el caso de un elevado rango de temperatura o de un paso lo suficientemente pequeño. Los diversos experimentos numéricos desarrollados, mostraron que el método desarrollado es capaz de capturar las discontinuidades y frentes agudos en la solución sin tener que añadir ningún tipo de disipación numérica. Por otro lado, se ha comprobado con detalle la convergencia y eficiencia del método construido, para lo cual, hicimos pruebas comparativas con dos de los métodos más usados en la literatura, que trabajan con modelos termomecánicos basados en entalpía. Estos son el de Bermúdez-Moreno y el de Nedjar.

Los resultados arrojaron que nuestro método h tipo Newton es más eficiente en términos de tiempo computacional. Para lograr un modelo más realista, completamos el método con las ecuaciones de Navier-Stokes. Estas nos ayudan a encontrar los valores de la velocidad y de la presión tanto de la fase líquida, como de la fase mixta. Cabe destacar la inclusión de dos términos de suma importancia para modelar tanto el fenómeno de la convección natural como para modelar el fenómeno del flujo de la zona líquida a través de medios porosos. Para el efecto, empleamos el modelo de Boussinesq, y el modelo de Darcy, respectivamente. Finalmente, en la última parte de esta investigación, desarrollamos una adaptación de nuestro modelo completo basado en entalpías, para determinar las diversas fases del acero que se pueden encontrar en un estudio de tratamiento térmico para el acero. Esto dio como resultado el aparecimiento de las fases austenita, martensita, bainita, ferrita y perlita, cuyas constituciones dependen de la variable temperatura.

Contents

List of Figures

Chapter 1

Introduction

1.1 Motivation

Metallurgy is a field of science and engineering that deals with the study of metals and their properties, extraction, processing, and refining. In today's world, metallurgy plays a crucial role in various industries such as automotive, aerospace, construction, and electronics, among others. The demand for high-quality metals is increasing due to the growing needs of these industries, making solving metallurgical problems a significant challenge. The metallurgical problems facing us today range from the need for stronger and more durable metals to the search for environmentally sustainable methods of production. With the increasing global population and the demand for advanced technology, the challenges facing the metallurgical industry are only growing. However, these challenges are also an opportunity to improve current practices and develop new, innovative solutions (Dieter 1988; Smallman and Bishop 1999; Brandt and Warner 2004; Seetharaman 2005; Abbaschian and Reed-Hill 2009).

The motivation to solve metallurgical problems today comes from the realization that successful resolution of these challenges is critical to the advancement of various industries and the overall development of our society. Addressing metallurgical problems requires a multidisciplinary approach that involves the collaboration of scientists, engineers, and technicians to find practical and effective solutions. The pursuit of solving metallurgical problems requires continuous research and innovation, which has the potential to drive progress and create significant positive impacts on the economy, the environment, and society as a whole (Instituto Nacional de Ciencia y Tecnología Metalúrgicas 2022; Asociación Española de Metalurgia y Materiales 2023).

Metallurgical problems are complex and often involve intricate physical and chemical phenomena. Mathematical modelling provides a powerful tool to understand these complex processes and optimize them for improved performance and efficiency. Mathematical models allow scientists and engineers to investigate and predict the behaviour of metals under different processing conditions and to identify potential issues before they occur. The use of mathematical models in metallurgical research has become increasingly important in recent years because of significant advances in computational power and numerical methods. These

models can simulate various metallurgical processes such as solidification, heat transfer, and diffusion, providing valuable insights into the underlying physics and chemistry. They also enable the optimization of process parameters to improve product quality, reduce waste, and lower production costs (R.W. Cahn 1996a; R.W. Cahn 1996b; R.W. Cahn 1996c).

The main motivation of this thesis is to make a contribution to the resolution of some metallurgical problems using cutting-edge mathematical and physical models. Mathematical modeling can and should reduce the need for expensive experimentation in both time and money, thus providing a solution to problems in an efficient and profitable way, and allows scientists, engineers and technicians to investigate complex processes both in size and shape that are difficult or very difficult to experience in situ. Furthermore, the construction of new robust, reliable and efficient models can and should help improve the predictive and preventive capabilities of the metallurgical industry, which leads to product improvement from an aesthetic, functional, environmental and cost point of view. Finally, we can conclude that the motivation mainly lies in the significant progress in the field, which will direct a metallurgical industry towards the path of sustainability and efficiency.

The three main metallurgical processes used in industry are as follows:

- Welding: Definitions are used to join metallic parts generally through the application of heat. This technique was discovered during efforts to manipulate iron into useful shapes. Welded blades were developed in the first millennium C.E., the most famous being those produced by Arab armourers at Damascus, Syria. The process of carburising iron to produce hard steel was known at this time, but the resultant steel was very brittle. The welding technique, which involved interlayering relatively soft and tough iron with high carbon material, followed by hammer forging, produced a strong and tough blade (Encyclopaedia Britannica 2023e).
- Casting-Foundry: Consists of pouring molten metal into a mould, where it solidifies into the shape of the mould. The process was well established in the Bronze Age (beginning c. 3000 BC), when it was used to form most of the bronze pieces now found in museums. It is particularly valuable for the economical production of complex shapes, ranging from mass-produced parts for automobiles to one-of-a-kind production of statues, jewellery, or massive machinery (Encyclopaedia Britannica 2023a).
- Heat Treatment: Change in the properties of materials such as metals or glass by processes involving heating. It is used to harden, soften, or modify other properties of materials that have different crystal structures at low and high temperatures. The type of transformation depends on the temperature at which the material is heated, how fast it is heated, how long it is kept heated, what temperature it is first cooled to, and how fast it is cooled. For example, quenching hardens steel by heating it to high temperatures and then quickly immersing it in room temperature oil, water, or salt brine to prevent carbon atoms from moving through the crystal structure and forming carbides, which soften the metal. The two main approaches to softening a metal (to restore its ductility) are annealing, in which its temperature is slowly raised, held for some time, and slowly cooled, and tempering, in which it is slowly heated in an oil bath and held for some hours (Encyclopaedia Britannica 2023b).

1.2 General objective

To develop a Lagrange-Galerkin numerical scheme with anisotropic mesh refinement for metallurgical problems.

1.3 Specific objectives

- To optimize the Lagrange-Galerkin numerical scheme with anisotropic mesh refinement for metallurgical problems.
- To apply the developed and optimized code to solve a particular set of metallurgical problems present in the industry.

1.4 Structure

Each chapter developed in this thesis is designed to be published as an independent article that also shows the parts of the whole that make up this research work. The following articles and book chapters are related to the chapters of this thesis as follows:

1. Chapter 2: An Enthalpy Model for Thermal Phenomena.
    - (Journal paper - JCR Q1 Category: Mathematics): M. Freire-Torres et al. (July 2023). "Numerical Solution of Thermal Phenomena in Welding Problems". In: *Mathematics* 11 (13), p. 3009. ISSN: 2227-7390. DOI: 10.3390/math11133009.
2. Chapter 3: Comparison of Enthalpy Methods for Stefan Problems.
    - (Paper ready to submit): M. Colera, M. Freire-Torres, J. Carpio. "Comparison of implicit enthalpy methods for Stefan problems".
3. Chapter 4: Navier-Stokes Equations to improve the Enthalpy Model.
    - (Book chapter): M. Freire-Torres and J. Carpio (2023). "Contribution to Mathematical Modeling and Numerical Simulation of Welding Processes". In: Springer International Publishing, pp. 24–29. DOI: 10.1007/978-3-031-38563-6_4.
    - (Proceedings paper): M. Freire-Torres and J. Carpio (2022). "Contribución al modelado matemático y la simulación numérica de procesos de soldadura". In: Universidad Nacional de Educación a Distancia (España). DOI: 10.5944/bicim2022.306.
4. Chapter 5: The Enthalpy Model applied to Heat Treatment.
    - (Paper in preparation): M. Freire-Torres, M. Colera, J. Carpio. "Heat treatment in steels applying an enthalpy model".

Chapter 2

An Enthalpy Model for Thermal Phenomena

2.1 Introduction

To begin, we must mention that Chapter 2 of this thesis is totally based on the published article by (Freire-Torres et al. 2023).

Welding, one of the most important metallurgical processes in the industry, joins parts of complex structures, offering significant economic and logistical advantages. It is defined as the fusion of two or more metal parts, either with or without a filler metal. This process uses high-power heat sources that cause a number of problems, such as residual stresses, deformations, porosity, internal and external fractures, and microdefects. These problems can greatly affect the structural and design integrity of the welded joints. To reduce costs and improve the welding process, numerical tools are used to perform thermomechanical analysis. This analysis helps to understand and control the variables involved in the welding process (Easterling 1992; Karkhin 2018).

The phase change thermal welding process leads to the so-called two-phase Stefan problem (Meirmanov 1992). This process is governed in the whole domain by an enthalpy formulation of the energy conservation equation (Oleinik 1960; Kamenomostskaya 1961; White 1982), which relates the changes in time in enthalpy, h, with the changes in temperature, T. The conservation equation must be complemented with a constitutive relation between h and T, which depends on the model considered. In the case of pure metals, the transition between the solid and liquid phases takes place at a constant temperature T_F (isothermal melting model). However, in alloys, which are composed of metals with different melting temperatures, the transition occurs in a range of $[T_F, T_F + \Delta T]$ (non-isothermal melting model) (Turichin et al. 2022).

Many methods in the literature, such as (Piekarska and Kubiak 2011; Piekarska and Kubiak 2013; Danaila et al. 2014; Kubiak and Piekarska 2016; Wu et al. 2018; Rakotondrandisa et al. 2020; Díaz Moreno et al. 2021; Atta 2022), consider a non-isothermal melting model, express h and other variables as functions of T, and solve the equation for energy conservation in

terms of temperature. These are called *temperature-based* methods or *effective specific heat* methods. Their main drawback is that they cannot be applied to the isothermal melting model because some variables, such as enthalpy or liquid mass fraction, may take different values for the melting temperature T_F. As a remedy, *enthalpy-based* methods (Nedjar 2002; Barral et al. 2003; Bermúdez and Otero 2004) pose the energy conservation equation in terms of enthalpy, which always univocally defines the state (temperature and liquid mass fraction are single-valued functions of enthalpy) of the metal regardless of the melting model.

In both isothermal and non-isothermal models, the energy conservation equation has a strongly nonlinear nature and, in many cases, does not have an analytical solution. Therefore, this is precisely where numerical methods come in. For instance, the element-free Galerkin (Álvarez-Hostos et al. 2019), Petrov-Galerkin methods (Shibahara and Atluri 2011), the finite volume method (Piekarska and Kubiak 2011) and the finite element method (Anca et al. 2011; Freire-Torres et al. 2023) are employed for space–time discretization, while Newton-type methods (Nedjar 2002; Anca et al. 2011; Freire-Torres et al. 2023) and fixed-point-type methods such as the Bermúdez-Moreno algorithm (Barral et al. 2003; Bermúdez and Otero 2004).

In this first chapter, we develop a finite element method to solve the energy conservation equation considering the phase change that governs welding problems. The non-linear discretized equations are solved with two versions of the Newton method. The first one, called the θ-Newton algorithm, is the same one that solves the energy equation considering temperature as the main unknown variable as is carried out in most of the literature (Piekarska and Kubiak 2011; Piekarska and Kubiak 2013; Rakotondrandisa et al. 2020; Álvarez-Hostos et al. 2019; Shibahara and Atluri 2011; Anca et al. 2011). The second one, called the h-Newton algorithm, is one of the most important contributions of this thesis, and solves the energy conservation equation considering enthalpy as the main unknown variable (Nedjar 2002; Barral et al. 2003; Bermúdez and Otero 2004; Freire-Torres et al. 2023).

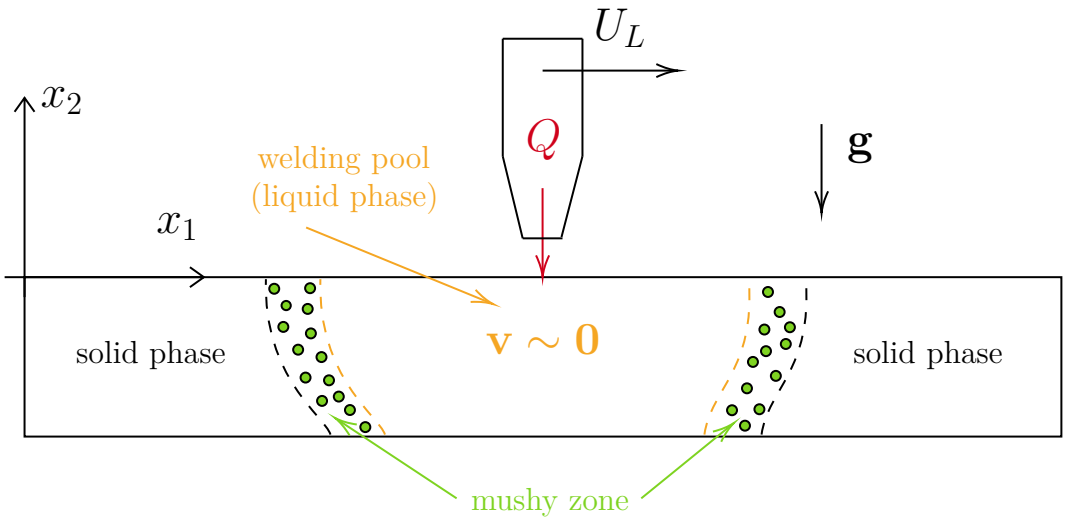

Figure 2.1: Simplified schematic of a welding problem, where we can see the three characteristic regions of the process.

2.2 Governing Equations

In this section, we present the equations that govern the welding phenomenon described above and shown schematically in Figure 2.1. Recall that there are three regions in the metal plate: solid, liquid, and mushy zone (where the solid and liquid phases coexist). As basic hypotheses of the model, we assume:

- Constant density ρ at the three regions, as in (Rakotondrandisa et al. 2020).
- The intensity of convective currents in the liquid zone is not significant; that is, the velocity $\mathbf{v} \sim \mathbf{0}$ at each material point. For our purpose, we consider problems at low Grashof number limit $\mathrm{Gr} \to 0$, so there is no motion caused by the buoyancy forces.
- Radiation and evaporation are not considered in this study.
- The equations of elasticity –which take into account deformations ans stresses in the material– and electromagnetism (Maxwell equations) –which model the effect of the laser-arc electric heat source– are not considered in this study.
- The specific heat coefficient and the thermal conductivity depend on the state of the material but not on the temperature. However, the present method can be easily extended to the more realistic case of temperature-dependent thermal coefficients.

2.2.1 Energy Conservation Equation

The metal plate is governed by the energy conservation equation (Nedjar 2002; Bermúdez and Otero 2004), without convective terms:

$$\rho \frac{\partial h}{\partial t} = \nabla \cdot (\lambda \nabla T) + Q, \qquad \text{in } \Omega, \tag{2.1}$$

where h is the enthalpy per unit mass, T is the temperature, λ is the thermal conductivity, Q is a volumetric heat source and Ω is the (fixed) domain occupied by the plate. We assume that the heat source Q is produced by a hybrid laser-arc source, which is capable of internally heating the material due to the Joule effect (Piekarska and Kubiak 2011; Piekarska and Kubiak 2013). The initial condition corresponds to a fully solid state at ambient temperature $T = T_0$, and the Dirichlet and Robin boundary conditions are defined in Γ_D and Γ_R, respectively (with $\partial\Omega = \Gamma_D \bigcup \Gamma_R$):

$$T = T_0 \ \text{ on } \Gamma_D, \qquad \text{and} \qquad -\lambda \frac{\partial T}{\partial \mathrm{n}} = \alpha (T - T_0) \ \text{ on } \Gamma_R, \tag{2.2}$$

where α is a convective coefficient and $\partial/\partial \mathrm{n}$ is the normal derivative. The enthalpy depends on the temperature and on the liquid mass fraction, Y_L, in such a way that $\mathrm{d}h = c\,\mathrm{d}T + H_F\,\mathrm{d}Y_L$, where c is the specific heat capacity and H_F is the latent heat of fusion. For pure metals, melting takes place in welding processes at a constant temperature T_F. In the case of constant values for latent heat of fusion, H_F, and for specific heat coefficients in the solid and liquid regions, c_S and c_L, respectively, the relation between enthalpy and temperature is given by

$$h \in h(T) = \begin{cases} c_S(T - T_0), & T < T_F, \\ [h_S,\ h_L], & T = T_F, \\ h_L + c_L(T - T_F), & T > T_F, \end{cases} \tag{2.3}$$

with $h_S = c_S(T_F - T_0)$ and $h_L = h_S + H_F$ the enthalpies of the solid and liquid regions at the melting temperature T_F, respectively. Note the choice $h(T_0) = 0$. Above, the notation $h \in [h_S, h_L]$ means that h may take any value in this interval. That is, the function $h(T)$ is multivalued at $T = T_F$, and therefore the state of the metal is not univocally defined by the temperature. This makes it impossible to numerically solve (2.1) and (2.2) with an isothermal model (2.3) in terms of temperature. However, the inverse function $T = T(h)$ is single-valued; hence, it is possible to solve these equations in terms of the enthalpy.

However, many references assume that the material is an alloy, a mixture of metals with different melting temperatures, and therefore the phase change takes place in a range of temperatures $[T_F, T_F + \Delta T]$. In these non-isothermal melting processes, the enthalpy can be written as a single-valued function in terms of temperature, i.e. $\mathrm{d}h = [c + H_F \mathrm{d}Y_L/\mathrm{d}T]\,\mathrm{d}T$, or shortly as $\mathrm{d}h = c_{\text{eff}}\,\mathrm{d}T$, where $c_{\text{eff}} = c + H_F \mathrm{d}Y_L/\mathrm{d}T$ is the *effective heat capacity*, which includes the heat released during the melting process; see, e.g. (Piekarska and Kubiak 2011; Piekarska and Kubiak 2013; Rakotondrandisa et al. 2020). In this chapter, we consider the following:

$$h = h(T) = \begin{cases} c_S(T - T_0), & T \leq T_F, \\ h_S + \dfrac{H_F}{\Delta T}(T - T_F), & T_F < T < T_F + \Delta T, \\ h_L + c_L(T - T_F), & T \geq T_F. \end{cases} \tag{2.4}$$

Note that $h(T_F + \Delta T) = h(T_F) + H_F$, so the non-isothermal melting model (2.4) requires the same energy as the isothermal melting model (2.3) for the phase change, and both models are equivalent if $\Delta T = 0$. Now, the enthalpy is a single value function of the temperature, so, in principle, this model makes it possible to employ this variable to solve equations (2.1) and (2.2), as carried out in many research papers. Nevertheless, we can see that the temperature variation required for the change in phase may be small, whereas the enthalpy variation is not. This makes Equations (2.1) and (2.2) numerically better conditioned when solved by setting the enthalpy as the main unknown variable than by setting the temperature, as will be shown in the numerical experiments.

Whenever we employ models (2.3) or (2.4), the thermal conductivity takes the form:

$$\lambda = \lambda(T) = \begin{cases} \lambda_S, & T \leq T_F, \\ \lambda_S + (\lambda_L - \lambda_S)\dfrac{T - T_F}{\Delta T}, & T_F < T < T_F + \Delta T, \\ \lambda_L, & T \geq T_F + \Delta T, \end{cases} \tag{2.5}$$

making the diffusion term in (2.1) non-linear. To manipulate this non-linearity, we use the Kirchhoff transformation (Özisik 1989), which consists of defining a new variable u such that:

$$\mathrm{d}u = \lambda(T)\mathrm{d}T, \quad u(T_0) = 0. \tag{2.6}$$

In that case, (2.1) and (2.2) read:

$$\rho\frac{\partial h}{\partial t} = \Delta u + Q \qquad \text{in } \Omega, \tag{2.7}$$

$$T\Big|_{t=0} = T_0 \qquad \text{in } \Omega, \tag{2.8}$$

$$T = T_0 \qquad \text{on } \Gamma_D, \tag{2.9}$$

$$-\frac{\partial u}{\partial \mathrm{n}} = \alpha(T - T_0) \quad \text{on } \Gamma_R. \tag{2.10}$$

For physical reasons, T is continuous in Ω, and hence is Kirchhoff's variable u. On the other hand, due to changes in phase, h, λ, and Y_L may present discontinuities (isothermal melting model) or very sharp variations (non-isothermal melting model).

2.2.2 Non-Dimensional Formulation

To have a better understanding of the physical phenomenon, it is always convenient to formulate the problem in a non-dimensional form. In this way, we can evaluate the order of magnitude of each term in the equations and see which are the relevant (non-dimensional) parameters that characterise the problem. The non-dimensional variables are denoted with the asterisk (*) symbol and defined as:

$$\begin{cases} \mathbf{x}^* = \dfrac{\mathbf{x}}{L_0},\ t^* = \dfrac{U_0}{L_0}t, \\ \\ \theta = \dfrac{T - T_0}{T_F - T_0},\ u^* = \dfrac{u}{\lambda_S(T_F - T_0)},\ h^* = \dfrac{h}{c_S(T_F - T_0)},\ Q^* = \dfrac{QL_0}{\rho c_S(T_F - T_0)U_0}, \end{cases} \tag{2.11}$$

where L_0 is the characteristic length (that is, that of the longest boundary) and U_0 is the characteristic velocity (that of the moving source). With the definitions established in (2.11), (2.7)–(2.10) are written in the following dimensionless form:

$$\frac{\partial h^*}{\partial t^*} = \frac{1}{\mathrm{Pe}}\Delta^* u^* + Q^* \quad \text{in } \Omega, \tag{2.12}$$

$$\theta\Big|_{t^*=0} = 0 \qquad \text{in } \Omega, \tag{2.13}$$

$$\theta = 0 \qquad \text{on } \Gamma_D, \tag{2.14}$$

$$-\frac{\partial u^*}{\partial \mathrm{n}^*} = \mathrm{Nu}\ \theta \qquad \text{on } \Gamma_R, \tag{2.15}$$

where the Péclet and Nusselt numbers are defined as:

$$\mathrm{Pe} = \frac{\rho c_S L_0 U_0}{\lambda_S}, \qquad \mathrm{Nu} = \frac{\alpha L_0}{\lambda_S}. \tag{2.16}$$

Two more dimensionless numbers have transcendental importance in thermal processes involving a change in phase: the Stefan number, Ste, defined as the ratio of the sensible heat and latent heat at solid, and the dimensionless temperature width, ΔT^*, at which the phase change takes place; that is:

$$\mathrm{Ste} = \frac{c_S(T_F - T_0)}{H_F}, \qquad \Delta T^* = \frac{\Delta T}{T_F - T_0}. \tag{2.17}$$

With the above definitions and (2.4) and (2.5), the (dimensionless) enthalpy, h^*, and the Kirchhoff variable, u^*, read in terms of θ as:

$$h^*(\theta),\ u^*(\theta) = \begin{cases} \theta, & \theta, & \theta \le 1, \\ 1 + \frac{\theta - 1}{\mathrm{Ste}\ \Delta T^*}, & 1 + (\theta - 1)\left[1 + \frac{\frac{\lambda_L}{\lambda_S} - 1}{2\Delta T^*}(\theta - 1)\right], & 1 < \theta < 1 + \Delta T^*, \\ \left(1 + \frac{1}{\mathrm{Ste}}\right) + \frac{c_L}{c_S}(\theta - 1 - \Delta T^*), & \frac{\lambda_L}{\lambda_S}(\theta - 1) + 1 - \frac{\Delta T^*}{2}\left(\frac{\lambda_L}{\lambda_S} - 1\right), & \theta \ge 1 + \Delta T^*. \end{cases} \tag{2.18}$$

We note that expressions in (2.18) are valid for isothermal and non-isothermal phase-change processes, but, in the first case (in which $\Delta T^* = 0$), the definition of $h^*(\theta)$ degenerates into a multivalued function. However, the inverse of the enthalpy function, $\theta(h^*)$, can be easily defined, and therefore also $u^*(h^*)$. The corresponding expressions are given by

$$\theta(h^*), u^*(h^*) = \begin{cases} h^*, & h^*, & h^* \le 1, \\ 1 + \mathrm{Ste}\ \Delta T^*\,(h^* - 1)\,, & 1 + \mathrm{Ste}\ \Delta T^*\,(h^* - 1)\left[1 + \frac{\frac{\lambda_L}{\lambda_S} - 1}{2}\mathrm{Ste}\,(h^* - 1)\right], & 1 < h^* < 1 + \frac{1}{\mathrm{Ste}}, \\ \left(h^* - 1 - \frac{1}{\mathrm{Ste}}\right)\frac{c_S}{c_L} + 1 + \Delta T^* & 1 + \frac{\Delta T^*}{2}\left(\frac{\lambda_L}{\lambda_S} + 1\right) + \frac{\lambda_L}{\lambda_S}\frac{c_S}{c_L}\left(h* - 1 - \frac{1}{\mathrm{Ste}}\right), & h^* \ge 1 + \frac{1}{\mathrm{Ste}}. \end{cases} \tag{2.19}$$

Now, the expressions in (2.19) do not degenerate; that is, the functions $\theta(h^*)$ and $u^*(h^*)$ are single valued even if $\Delta T^* = 0$. This property makes non-linear (2.12) numerically better conditioned when solved (via, e.g. a Newton method) considering the enthalpy as main unknown variable.

Moreover, the mass fraction of the liquid Y_L can also be defined in terms of enthalpy and does not depend on ΔT^*. Although it does not appear in this formulation, it can be used to visualise the free surfaces that separate the musky region from the solid phase ($Y_L = 0$) and the musky region from the liquid phase ($Y_L = 1$).

$$Y_L(h^*) = \begin{cases} 0, & h^* \le 1, \\ (h^* - 1)\mathrm{Ste}, & 1 < h^* < 1 + \dfrac{1}{\mathrm{Ste}}, \\ 1, & h^* \ge 1 + \dfrac{1}{\mathrm{Ste}}. \end{cases} \tag{2.20}$$

The expression above is valid for isothermal and non-isothermal phase-change processes.

From now on, we remove the asterisk (*) symbol to not overload the notation, and all variables that appear will be dimensionless unless otherwise stated.

It should be pointed out that the present thermal model also applies when there is a thermal shock. For this purpose, the heat source must be described by means of a hyperbolic tangent or a similar mathematical function to force a sudden change in the temperature. However, to find the mechanical stresses due to thermal effects and strain, it would be necessary to complement the thermal model with the equations of elasticity.

2.3 Numerical Discretization of the Problem

Once the mathematical model has been formulated, we design an algorithm based on a second-order time-marching scheme in combination with second-order local adaptative finite element discretization in space. More specifically, we first split the time interval of integration $[0,\ t_f]$ into subintervals $[t_{n-1},\ t_n]$ of constant length $\Delta t = t_n - t_{n-1}$. Then, we discretize (2.12) with a BDF2 formula:

$$\frac{3h^n - 4h^{n-1} + h^{n-2}}{2\Delta t} = \frac{1}{\mathrm{Pe}}\Delta u^n + Q^n, \quad \text{in } \Omega, \tag{2.21}$$

for $n = 2, ..., N_t$, with $N_t\Delta t = t_f$. At each time level t^n, the domain Ω is partitioned into a triangular mesh $\mathbb{T}_h^n$, to which we associate the finite element space that accompanies it.

$$V_{h0}^n = \{\varphi_h \in C^0(\mathbb{R}^2) : \varphi_h|_K \in P_2(K),\ \ \forall K \in \mathbb{T}_h^n \ \text{ and } \ \varphi_h|_{\Gamma_D} = 0\}, \tag{2.22}$$

where $P_2(K)$ is the space of quadratic polynomials on an element K. That is, V_{h0}^n is the space of continuous and quadratic polynomials (defined piecewise at the mesh elements) that vanish at the Dirichlet boundary Γ_D. Note from (2.14) and (2.18) that h, θ, and u also vanish at Γ_D. Therefore, we can approximate these variables as:

$$h_h^n(\mathbf{x}) = \sum_{i=1}^{N^n} h_i^n\varphi_i(\mathbf{x}), \quad \theta_h^n(\mathbf{x}) = \sum_{i=1}^{N^n} \theta_i^n\varphi_i(\mathbf{x}), \ \text{ and } \ u_h^n(\mathbf{x}) = \sum_{i=1}^{N^n} u_i^n\varphi_i(\mathbf{x}), \tag{2.23}$$

where N^n is the number of mesh nodes (excluding those at Γ_D), h_i^n, θ_i^n, and u_i^n are the values of h^n, θ^n, and u^n at these nodes, and $\varphi_i(\mathbf{x})$ are the corresponding Lagrangian basis functions.

With the considerations above, (2.21) reads in weak form as:

$$\begin{aligned} &3\int_\Omega h_h^n\varphi_h d\mathrm{x} + \frac{2\Delta t}{\mathrm{Pe}}\int_\Omega \nabla u_h^n\cdot\nabla\varphi_h d\mathrm{x} + \frac{2\Delta t\mathrm{Nu}}{\mathrm{Pe}}\int_{\Gamma_R}\theta_h^n\varphi_h d\mathrm{s} = \\ &= \int_\Omega 2\Delta t Q^n\varphi_h d\mathrm{x} + \int_\Omega (4h_h^{n-1} - h_h^{n-2})\varphi_h d\mathrm{x}, \ \ \forall\varphi_h \in V_{h0}^n. \end{aligned} \tag{2.24}$$

Equation (2.24) can be rewritten in matrix form to simplify the notation:

$$3\mathbf{M}\ \mathbf{h}^n + \frac{2\Delta t}{\mathrm{Pe}}\mathbf{K}\ \mathbf{u}^n + \frac{2\Delta t \mathrm{Nu}}{\mathrm{Pe}}\mathbf{M}_{\Gamma_R}\boldsymbol{\theta}^n = \mathbf{f}^n, \tag{2.25}$$

where the bold variables are vectors or matrices whose elements are defined by

$$\begin{aligned} &M_{ij} = (\varphi_i, \varphi_j)_\Omega, \quad K_{ij} = (\nabla\varphi_i, \nabla\varphi_j)_\Omega, \quad M_{\Gamma_R ij} = (\varphi_i, \varphi_j)_{\Gamma_R} \\ &f_i^n = (2\Delta t Q^n + 4h_h^{n-1} - h_h^{n-2}, \varphi_i)_\Omega, \end{aligned} \tag{2.26}$$

and with $(\cdot\ ,\ \cdot)$ the standard scalar product in the L^2 norm. Note that, due to the introduction of Kirchhoff's variable (2.6), the stiffness matrix is constant (whenever the mesh remains fixed), which greatly simplifies the solution algorithm.

2.3.1 The $\mathcal{X}$ - Newton Algorithm

The system (2.25) defines a non-linear problem due to the relations between the unknown variables of problem h_i^n, θ_i^n, and u_i^n. To approach its resolution, we have employed a Newton algorithm. We consider two versions of the latter. In the first, the θ -Newton algorithm, we set the (nodal) temperatures θ_i^n as the main unknowns and evaluate h_i^n and u_i^n through (2.18). In the second algorithm, the h-Newton algorithm, we set the (nodal) enthalpies h_i^n as the main unknowns and evaluate θ_i^n and u_i^n using (2.19). As both versions are formally identical, we introduce an abstract variable $\mathcal{X}$, which denotes θ or h, depending on the case, and we call the method the $\mathcal{X}$-Newton algorithm.

Let $\boldsymbol{\mathcal{X}}_k^n$ denote the vector of unknowns in the k-th iteration. The residual and Jacobian values of (2.25) are:

$$\begin{aligned} \mathbf{b}_k^n &= 3\mathbf{M}\ \mathbf{h}_k^n + \frac{2\Delta t}{\mathrm{Pe}}\mathbf{K}\ \mathbf{u}_k^n + \frac{2\Delta t \mathrm{Nu}}{\mathrm{Pe}}\mathbf{M}_{\Gamma_R}\boldsymbol{\theta}_k^n - \mathbf{f}^n, \\ \mathbf{J}_k^n &= 3\mathbf{M}\ \mathbf{D}_k^h + \frac{2\Delta t}{\mathrm{Pe}}\mathbf{K}\ \mathbf{D}_k^u + \frac{2\Delta t \mathrm{Nu}}{\mathrm{Pe}}\mathbf{M}_{\Gamma_R}\ \mathbf{D}_k^\theta. \end{aligned}$$

where $h_{k,i}^n = h(\mathcal{X}_{k,i}^n)$, $\theta_{k,i}^n = \theta(\mathcal{X}_{k,i}^n)$, $u_{k,i}^n = u(\mathcal{X}_{k,i}^n)$ are evaluated by (2.18) or (2.19); $\mathbf{D}_k^\phi$ (with ϕ denoting h, θ, or u) is the diagonal matrix

$$D_{k,ij}^\phi = \left.\frac{d\phi}{d\mathcal{X}}\right|_{\mathcal{X}_{k,i}^n} \delta_{ij}, \tag{2.27}$$

δ_{ij} is the Kronecker delta, and the derivatives $d\phi/d\mathcal{X}$ are easily computed from expressions (2.18) or (2.19). Then, the value of $\boldsymbol{\mathcal{X}}_{k+1}^n$ at the next iteration $k+1$ is given by solving the following.

$$\mathbf{J}_k^n \boldsymbol{\Delta\mathcal{X}}_{k+1}^n = -\mathbf{b}_k^n, \quad \boldsymbol{\mathcal{X}}_{k+1}^n = \boldsymbol{\mathcal{X}}_k^n + \boldsymbol{\Delta\mathcal{X}}_{k+1}^n.$$

Iterations are stopped when the norm of $\boldsymbol{\Delta\mathcal{X}}_{k+1}^n$ is within a tolerance of 10^{-10}. The Jacobian has to be evaluated at each iteration. However, since the finite element matrices $\mathbf{M}$, $\mathbf{K}$, $\mathbf{M}_{\Gamma_R}$ are constant and only the diagonal matrices $\mathbf{D}_k^\phi$ need to be recomputed, this is not an expensive operation.

The relations (2.19) are based on the major assumption that the specific heat and thermal conductivity do not depend on the temperature. However, in more realistic cases, this assumption is not true, and there is no analytical expression for the relations $\theta(h)$ and $u(h)$ required by the h-Newton method. Instead, one disposes of analytical (nonlinear) expressions for $h(\theta)$ and $u(\theta)$, e.g. NASA polynomials (McBride et al. 2002). In these cases, it is straightforward to obtain θ from h (and hence also u from h) by solving equation $h = h(\theta)$, for example, with the aid of a Newton algorithm. Since the function $h(\theta)$ is piecewise monotone and smooth, the cost of this operation should be negligible. On the other hand, the matrices $\mathbf{D}_k^\theta$ and $\mathbf{D}_k^u$ defined by (2.27) can be easily calculated in the h-Newton algorithm as:

$$D_{k,ij}^\theta = \left.\frac{d\theta}{dh}\right|_{h_{k,i}^n} \delta_{ij} = \left[\left.\frac{dh}{d\theta}\right|_{\theta_{k,i}^n}\right]^{-1} \delta_{ij}, \quad \text{and} \quad D_{k,ij}^u = \left.\frac{du}{dh}\right|_{h_{k,i}^n} \delta_{ij} = \left.\frac{du}{d\theta}\right|_{\theta_{k,i}^n} \left[\left.\frac{dh}{d\theta}\right|_{\theta_{k,i}^n}\right]^{-1} \delta_{ij}.$$

We note that, although there is no analytical expression, the function $\theta(h)$ is single-valued and therefore $d\theta/dh|_{h_{k,i}^n} = \left[dh/d\theta|_{\theta_{k,i}^n}\right]^{-1}$ is finite.

2.3.2 Mesh Refinement

To conclude with the section dedicated to the discretization and numerical resolution of the equations, we provide a brief description of the local anisotropic mesh refinement technique employed here; the reader is referred to (Carpio and Prieto 2014; Carpio et al. 2016; Carpio et al. 2019) for more details. With this technique, we define at each time level t^n a mesh triangulation $\mathbb{T}_h^n$ so that the solution is computed within a given accuracy employing the minimum possible number of degrees of freedom (mesh nodes).

As shown in Figure (2.2), an anisotropic element K can be defined by the lengths of the semiaxes $\lambda_{1,K} \geq \lambda_{2,K}$ of the circumscribed ellipse E, and by the corresponding orthogonal directions $\mathbf{r}_{1,K}$ and $\mathbf{r}_{2,K}$. The element size is $|K| = 3\sqrt{3}/4\ \lambda_{1,K}\lambda_{2,K}$, and the aspect ratio is defined as $s_K = \lambda_{1,K}/\lambda_{2,K}$. To employ an automatic mesh generator, we must define a metric tensor $\mathbf{M}_K$ such that:

$$\mathbf{M}_K = \left(\frac{|\widehat{K}|}{|K|}\right) \mathbf{R}_K \mathbf{S}_K^{-1} \mathbf{R}_K^T, \tag{2.28}$$

with $\mathbf{R}_K = \{\mathbf{r}_{1,K},\ \mathbf{r}_{2,K}\}$, $\mathbf{S}_K = \text{diag}\,\{s_K,\ 1/s_k\}$ and $|\widehat{K}|$ the size of the generated element

when $\mathbf{M}_K$ is the unity tensor. The latter parameter depends on the specific mesh generator; in this work, we employ BAMG (Hecht 2006), for which $|\widehat{K}| = \sqrt{3}/4$.

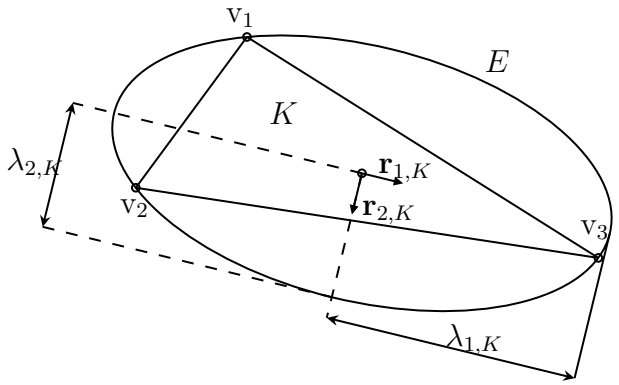

Figure 2.2: Fundamental parameters of an anisotropic element K.

The optimal orientation $\mathbf{R}_K^*$ and the shape $\mathbf{S}_K^*$ of the element K can be calculated from the Hessian matrix $\mathbf{H}_K$ of the solution h_h^n. More specifically, if $g_{i,K}$ are the eigenvalues (with $|g_{1,K}| < |g_{2,K}|$) and $\mathbf{l}_{i,K}$ are the corresponding eigenvectors, we obtain:

$$s_K^* = \left(|g_{2,K}|/|g_{1,K}|\right)^{1/2}, \quad \mathbf{r}_{i,K}^* = \mathbf{l}_{i,K}, \quad \text{for } i = 1,\ 2. \tag{2.29}$$

Finally, the optimal size $|K^*|$ for each element K is calculated to minimise the number of mesh elements under a condition of the form $\eta^n = \left(\sum_K (\eta_K^n)^2\right)^{1/2} \leq \text{Tol}$, where η_K is an estimate of the error on K. In particular,

$$\eta_K^n = \left(\int_K \left[h^n - \Pi_{h1} h^n\right]^2 \ d\text{x}\right)^{1/2}, \tag{2.30}$$

with $\Pi_{h1} h^n$ being the continuous piecewise linear interpolation of h^n at the mesh vertices, and

$$|K^*| = |K| \left(\frac{\text{Tol}^2}{\sum\limits_{K \in \mathbb{T}_h^n} (\eta_K^n)^{1/2}}\right)^{1/3} (\eta_K^n)^{-1/2}. \tag{2.31}$$

The variables $|K^*|$, $\mathbf{R}_K^*$, and $\mathbf{S}_K^*$ define a metric tensor $\mathbf{M}^*$ via equation (2.28), which is sent to BAMG (Hecht 2006) to generate a new mesh $\mathbb{T}_h^{n*}$.

Hence, at each time level t^n, we have a solution computed on $\mathbb{T}_h^n$ with an estimated error η^n and a new (more optimal) mesh $\mathbb{T}_h^{n*}$. If $\eta^n > \text{Tol}$, we set $\mathbb{T}_h^n = \mathbb{T}_h^{n*}$ and recompute the solution at t^n. Otherwise, we accept the solution at time t_n and set $\mathbb{T}_h^{n+1} = \mathbb{T}_h^{n*}$. In practice, if the time step size is moderate, the solution computed at t^n is seldom rejected, and thus the CPU time does not increase substantially with the present local mesh adaptation algorithm.

It is not strictly necessary to adapt the mesh at each iteration. Indeed, some authors prefer to keep the mesh fixed until the time step is rejected because the space error is higher than the tolerance. However, we prefer to update the mesh at each time level in order to have a better tracking of the borders of the phase-change region. Furthermore, the number of rejected time steps is smaller if the mesh is updated at each time level.

2.4 Numerical results

In this section, we show the results of several numerical experiments to address the performance of the present method. All tests were carried out on an i7-8700 CPU computer with 16GB DDR3 RAM @1.3 GHz and Ubuntu 20.02.4 LTS operating system using the C programming language.

2.4.1 Test I: Convergence and computational cost analysis

2.4.1.1 Introduction to the analytical solution of the energy equation

To begin, we consider the 1D version of Equation (2.7), that is:

$$\frac{\partial h}{\partial t} - \frac{1}{\mathrm{Pe}}\frac{\partial^2 u}{\partial x^2} = Q, \tag{2.32}$$

in the domain $[-1/2, 1/2]$. The initial condition is $h(x, 0) = 0$, the boundary conditions are $h(\pm 1/2, t) = 0$, and the heat source is:

$$Q(x,t) = \frac{A}{t_0} e^{-t/t_0} \cos(\pi x) + \frac{A\pi^2}{\mathrm{Pe}}(1 - e^{-t/t_0}) \cos(\pi x), \tag{2.33}$$

with $A > 1$ and $t_0 > 0$. Note that $Q(x, t) \geq 0$, so we can expect the temperature to increase and a phase change to appear eventually.

Initially, the whole material is solid. In that case, $\mathrm{d}u = \mathrm{d}h$ according to (2.19), and hence, Equation (2.32) reads

$$\frac{\partial h}{\partial t} - \frac{1}{\mathrm{Pe}}\frac{\partial^2 h}{\partial x^2} = Q. \tag{2.34}$$

It is easy to verify that an analytical solution of (2.34) is:

$$h(x,t) = A(1 - e^{-t/t_0}) \cos(\pi x), \tag{2.35}$$

with the given initial and boundary conditions. This solution is valid for $t \leq t_m$, where t_m is the first time level at which there exists a point at which melting occurs. Since the initiation of melting in the material is given by the condition $h = 1$ and the enthalpy is maximum at $x = 0$,

$$t_m = t_0 \ln\left(\frac{A}{A-1}\right). \tag{2.36}$$

It is difficult to obtain an analytical solution for $t > t_m$. However, for $t \to \infty$, the heat source is constant in time,

$$Q^\infty(x) := Q(x, +\infty) = \frac{A\pi^2}{\mathrm{Pe}} \cos(\pi x), \tag{2.37}$$

so we can expect a steady state solution, $h^\infty(x)$. Due to the boundary conditions, there must exist a region at which the material is solid. In this region, the enthalpy is governed by,

$$-\frac{1}{\mathrm{Pe}} \frac{\partial^2 h^\infty}{\partial x^2} = Q^\infty, \tag{2.38}$$

and, since $h = 0$ at the boundaries, the solution is:

$$h^\infty(x) = A \cos(\pi x). \tag{2.39}$$

This is valid only for the points such that $h^\infty \leq 1$, i.e. for $|x| > x_{LS} := \arccos(1/A)/\pi$. At the rest of the domain, due to the action of the source, the material is liquid. In that case, Equation (2.32) yields $\mathrm{d}u = \beta \mathrm{d}h$, with $\beta = (\lambda_L c_S)/(\lambda_S c_L)$, and Equation (2.32) reads,

$$-\frac{\beta}{\mathrm{Pe}} \frac{\partial^2 h^\infty}{\partial x^2} = Q^\infty. \tag{2.40}$$

Note that, at the interface with the solid region $x = \pm x_{LS}$, $h^\infty = 1 + 1/\mathrm{Ste}$, because the material is at the melting temperature. Hence, the solution of (2.40) is:

$$h^\infty(x) = \frac{A}{\beta} \cos(\pi x) + 1 + \frac{1}{\mathrm{Ste}} - \frac{1}{\beta}. \tag{2.41}$$

Summarizing,

- For $t \leq t_m$, all the material is solid state and the solution is given by Equation (2.35).
- For $t \to \infty$, the solution is given by Equation (2.39), if $|x| > \arccos(1/A)/\pi$ (solid state), and by the Equation (2.41) othewise (liquid state).

2.4.1.2 Numerical solution of the energy equation

The first test is used to verify that the numerical solution is correct and to analyse the convergence properties and the computational cost of the method. The test is defined by the domain $[-1/2, 1/2]^2$, a heat source according to Equation (2.33), with $A = 1.5$ and $t_0 = 0.5$, initial condition $h = 0$, homogeneous Dirichlet conditions $h = 0$ at $x_1 = \pm 1/2$, homogeneous Neumann conditions $\mathrm{d}u/\mathrm{d}x_2 = 0$ at $x_2 = \pm 1/2$, and the dimensionless parameters,

$$\text{Ste} = 0.5, \quad \text{Pe} = 20, \quad c_S/c_L = 0.75, \quad \lambda_S/\lambda_L = 1.5.$$

Here we employ the h-Newton solver. We show in section 2.4.1.1 that, for $t < t_m := t_0 \ln(A/(A-1)) \simeq 0.55$.

Figure (2.3) shows the numerical solution for several instants in time. As can be seen, the agreement with the theoretical solution at the fully solid state is very good. Then, a phase change appears and the solution evolves into a steady state solution. For large t, we see that the numerical solution agrees again very well with the theoretical steady-state solution, not only for the values of the solution but also for the position of the phase front.

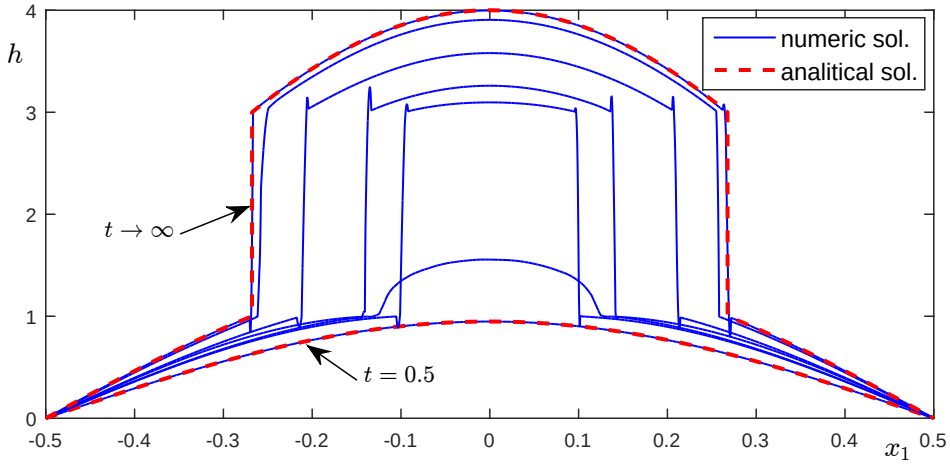

Figure 2.3: Numerical solution of Test I for $t = 0.5, 1, 3, 5, 10, 20, 40$ at the line $x_2 = 0$.

On the other hand, Figure (2.4) (left) shows the convergence of the L^2 error between the theoretical and numerical solution, e_{L^2}, with respect to the mesh size, defined as $\text{h} := \sqrt{|\Omega|/\text{NE}}$, with NE the number of elements. The error is evaluated at $t = 0.5 < t_m$, when the solution is still smooth. Here, we use a uniform mesh and a time step $\Delta t = 0.001$. As can be seen, we obtain the expected $\mathcal{O}(\text{h}^3)$ convergence rate.

Similarly, Figure (2.4) (right) illustrates the dependence of the L^2 error on the time step. Here, we set a tolerance for space $\text{Tol} = 0.1$. We can verify that the expected $\mathcal{O}(\Delta t^2)$ convergence rate is achieved.

Finally, Figure (2.5) shows the evolution of the number of elements and the accumulated CPU time with respect to the solved instant of time t. Here, we employ different tolerances for mesh adaptation and a time step $\Delta t = 0.001$. As can be seen, the number of elements increases slowly since $t = 0$. At $t = t_m$, melting begins to take place, and the number of elements starts to increase more quickly. Finally, for $t \gtrsim 1.3$, the evolution of the phase front is more stable and the number of elements remains constant. Since the number of elements increases to $t \gtrsim 1.3$, so does the time needed to solve each instant of time. We can verify this point by observing the slope of the curve of the accumulated CPU time.

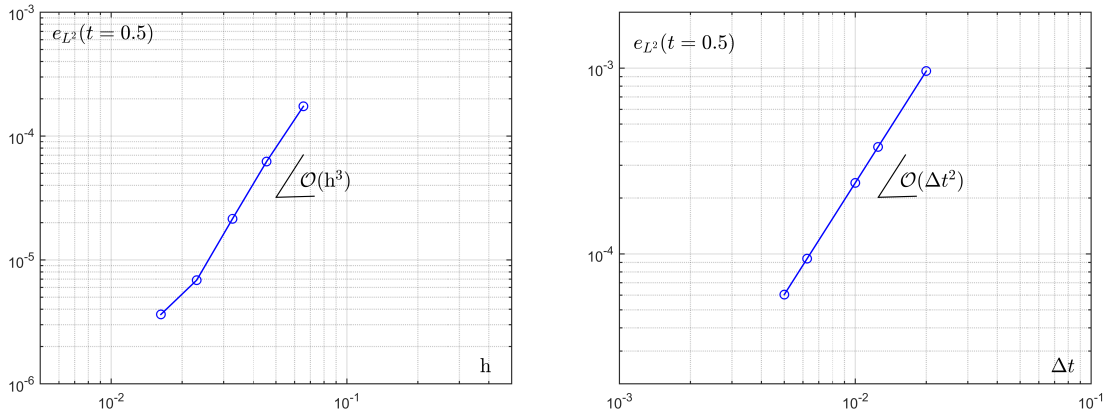

Figure 2.4: Convergence of the L^2 error with respect to the mesh size (left) and the time step (right).

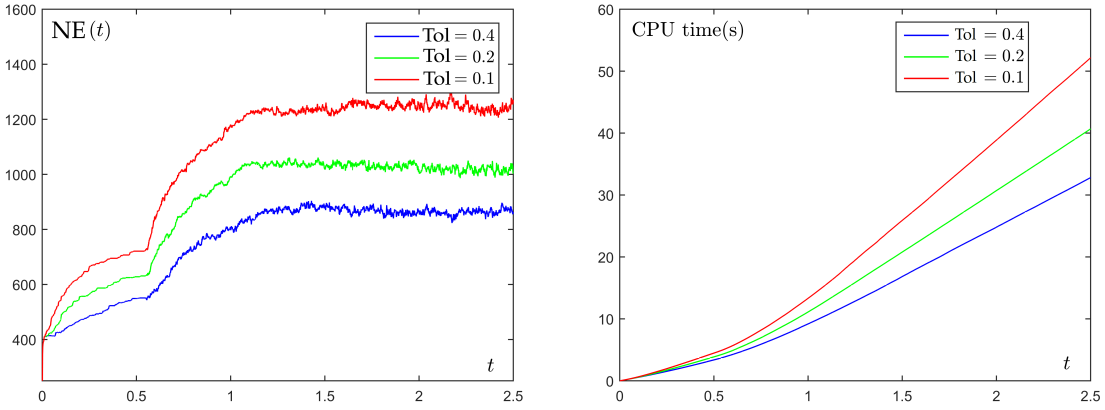

Figure 2.5: Evolution of the number of elements (left) and of the accumulated CPU time (right) with respect to the solved instant of time.

2.4.2 Test II: Gaussian-type heat source

To evaluate the two numerical strategies (the θ-Newton method or the h-Newton method, depending on the unknown considered) in the resolution of the welding problem, we present an example defined by the rectangular domain $\Omega = [0, 2.5] \times [-1, 0]$, with boundary $\partial\Omega \equiv \Gamma_1 \cup \Gamma_2 \cup \Gamma_3 \cup \Gamma_4$, as can be seen in Figure (2.6). We consider an initial condition $\theta = 0$, Dirichlet boundary conditions on $\Gamma_D \equiv \Gamma_1 \cup \Gamma_2 \cup \Gamma_4$, where the temperature is set to the ambient one, and a Robin condition on $\Gamma_R \equiv \Gamma_3$, where there is a loss of heat by convection; recall Equations (2.13)– (2.15). The numerical integration will take place for $0 \leq t \leq 2.5$ with $\Delta t = 0.01$.

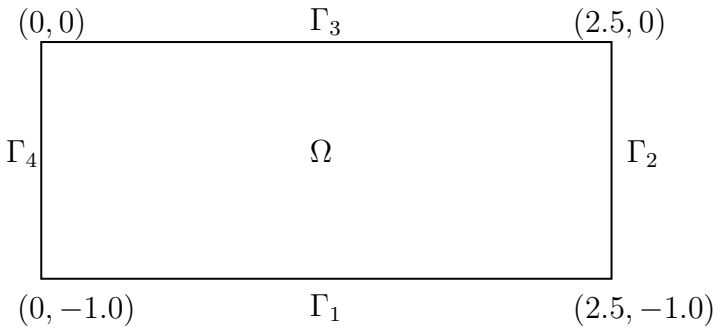

Figure 2.6: Domain and boundaries associated with the welding problem.

With the heat source Q, we take a Gaussian-type function moving from left to right with constant velocity v^0. Furthermore, to obtain more valuable information on the physical process under study, we consider that the heat source only acts up to the instant $t = 1.0$ so as to analyze the behavior of the system with $(0 < t \leq 1)$ and without $(1 < t \leq 2.5)$ a heat source:

$$Q(x_1, x_2, t) = \begin{cases} Q^0 \exp\left(-100\left(x_1 - \left(x_1^0 + v^0 t\right)\right)^2 - 25\left(x_2 - x_2^0\right)^2\right)\left(1 - e^{-5t}\right), & 0 \leq t \leq 1, \\ 0, & 1 < t \leq 2.5, \end{cases} \tag{2.42}$$

with $Q^0 = 50.0$, $v^0 = 1.5$, $x_1^0 = 0.5$, and $x_2^0 = -0.5$.

Finally, the values of dimensionless parameters are computed from the physical magnitudes of (Piekarska and Kubiak 2011; Piekarska and Kubiak 2013):

$$\mathrm{Pe} = 20, \quad \mathrm{Nu} = 10, \quad c_S/c_L = 0.75, \quad \lambda_S/\lambda_L = 1.5. \tag{2.43}$$

Figure (2.9) shows the solution for different values of the Stefan number at three different instants in time. Here, we employ the isothermal melting model (2.3). The upper panels represent the thermodynamic variables (enthalpy h, temperature θ, and mass fraction of liquid Y_L) at the line $x_2 = -0.5$, whereas the bottom panels show the border between the pure solid and pure liquid zones ($Y_L = 0$ and $Y_L = 1$, respectively).

As can be seen in the Figure (2.9), the mushy region is negligible when the Stefan number is large. However, as the latter decreases, the mushy region becomes more relevant and the method must be more accurate to capture it. This is due to the fact that a smaller Stefan number implies a larger $h_L - h_S$; i.e. more energy is needed for the phase change. As a consequence, for the same heat source and the same time level—i.e. same energy transferred to the material—the proportion of the material that is yet in phase change state is larger. In all cases, after the heat source goes out at $t = 1$, the mushy region tends to disappear and the transition between solid and liquid becomes a discontinuity for the enthalpy variable. At

the discontinuity, the material is at the melting temperature, so the jump in the enthalpy equals $h_L - h_S = 1/\text{Ste}$, as can be verified in the figure. Furthermore, Figure (2.7) shows the evolution of the mesh for the case $\text{Ste} = 0.25$ considered before. We can see that, due to the use of anisotropic mesh adaptation techniques, the elements are refined at the border of the mushy region, which is the region at which the variations in the solution are more noticeable, and also that they are aligned with the latter.

On the other hand, Figure (2.8) considers a fixed Stefan number $\text{Ste} = 0.5$ and non-isothermal melting model (2.4) with different values for the temperature width ΔT. We can see that, as ΔT increases, the solution smooths out (especially in the enthalpy variable h and liquid mass fraction Y_L) and the mushy region becomes larger. This is to be expected since, for a continuous temperature field, it is impossible to have a discontinuity in the enthalpy with the non-isothermal melting model. Indeed, for the same range of temperatures, the variation in the enthalpy is less abrupt for larger ΔT, hence the fact that the enthalpy smooths out with this parameter. Moreover, when the heat source is not applied (i.e. from $t = 1$ to $t = 2.5$), the size of the mushy region increases, something that is opposite to the physics of the problem for $\Delta T = 0$, shown in Figure (2.9), where an abrupt transition between the solid and liquid zone tends to appear when time goes on.

Apart from the physical insights of the results, we are interested in proving that solving for the enthalpy (i.e. the h-Newton method) is more robust than solving for the temperature (i.e. the θ-method). For that purpose, Figure (2.10) shows a convergence study of the θ-method for different values of Ste, Δt, and ΔT. More specifically, it shows for which cases the θ-method is able to obtain a solution and for which ones it fails. It is interesting to see that, for sufficiently large melting temperature width ΔT, the method converges irrespective of the time step.

This threshold ΔT increases with $1/\text{Ste}$, i.e. with the enthalpy variation between liquid and solid states. For smaller ΔT, the time step Δt has to be sufficiently small; otherwise, the method fails to converge. It seems that the maximum Δt is approximately proportional to ΔT. Hence, for this particular problem and boundary conditions, the convergence criterion for the θ-method can be summarized as

$$\Delta T \gtrsim \min\left(\frac{1}{3\text{Ste}},\ 10\Delta t\right). \tag{2.44}$$

For other problems, we may expect to find a qualitatively similar convergence criterion. Conversely, the h-Newton converged for all the cases shown in Figure (2.10). This proves numerically that solving for the enthalpy is more robust than solving for the temperature. This a consequence of the fact that relations (2.18) are ill-conditioned for temperatures close to the melting range, in the sense that small variations in θ may cause large variations in the enthalpy, and, hence, convergence is more difficult. The slope of the curve $h(\theta)$ at the melting temperature range is proportional to $1/(\Delta T\text{Ste})$, and, thus, convergence is more difficult when ΔT and/or Ste are smaller, as can be verified in the figure. On the contrary, relations (2.19) are always well conditioned irrespective of ΔT and $1/\text{Ste}$, making convergence much easier when solving for the enthalpy. Finally, it must be pointed out that, although there are some spurious oscillations, the discontinuities in the solutions shown in previous figures are well captured without the need of any kind of artificial viscosity.

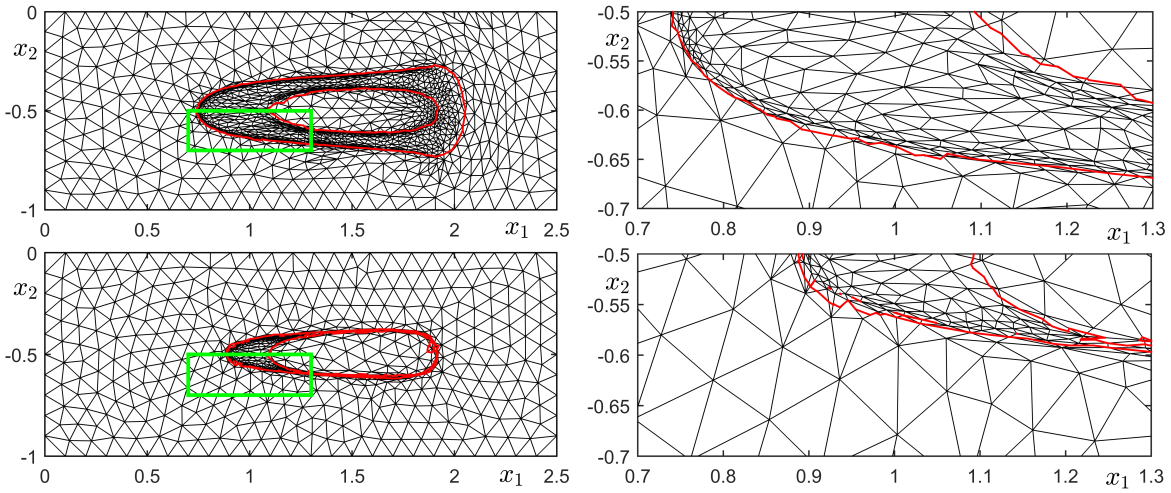

Figure 2.7: Discretization mesh for Ste $= 0.25$ at $t = 1.0$ (top) and $t = 2.5$ (bottom).

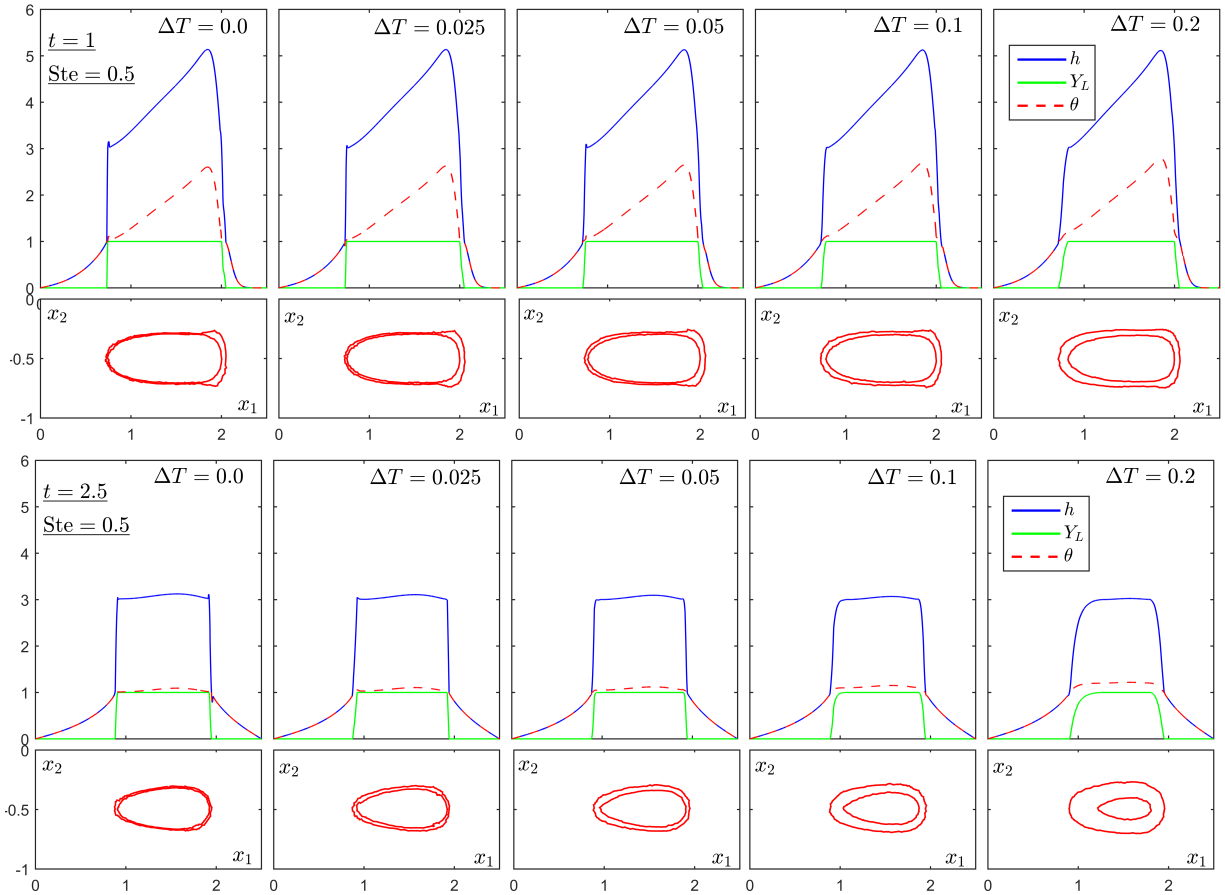

Figure 2.8: Solutions obtained for Ste $= 0.5$ and different values of the range of temperatures ΔT where the phase change takes place. The heat source acts for $t \leq 1$.

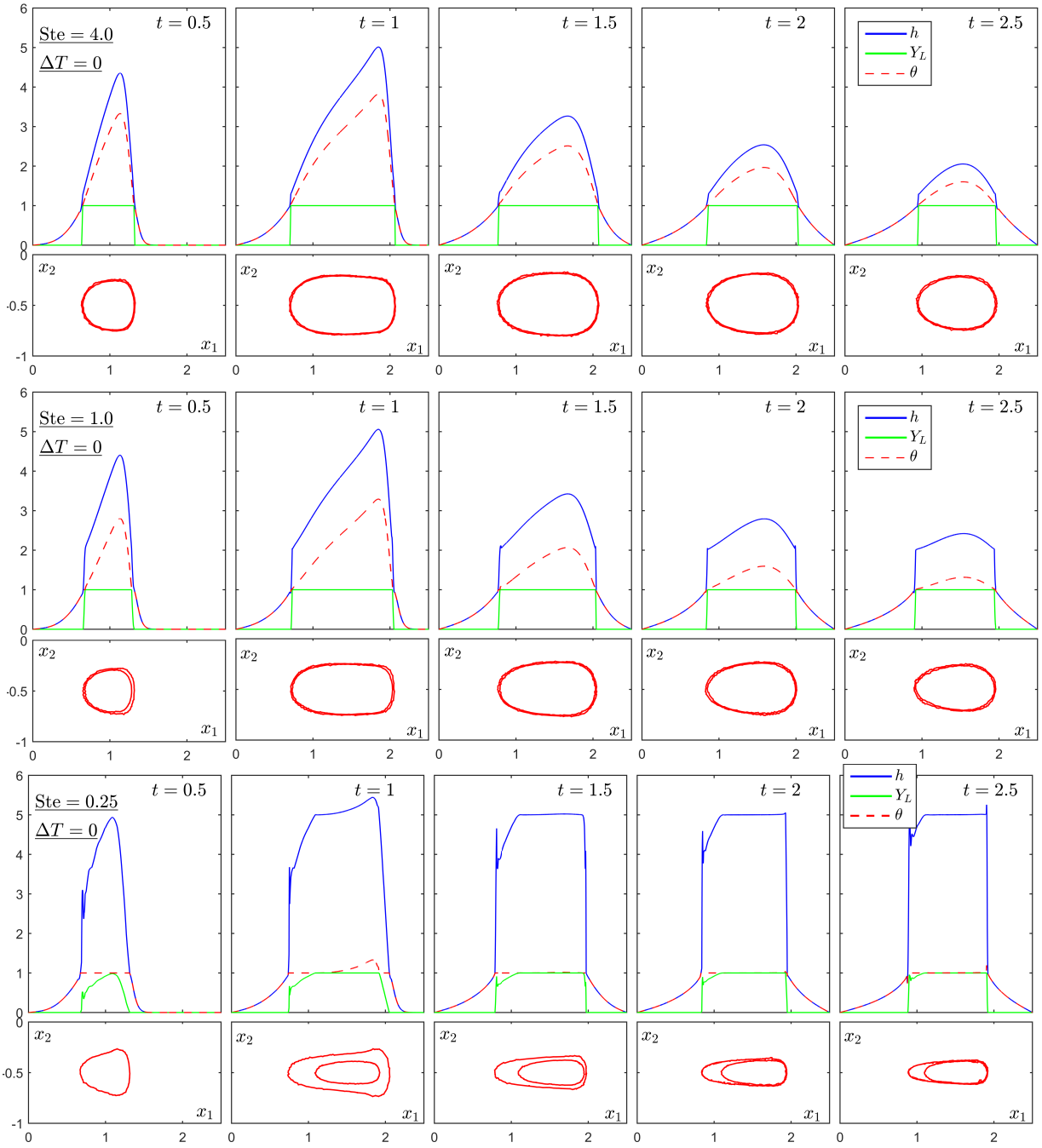

Figure 2.9: Solutions obtained for different values of the Stefan number and $\Delta T = 0$. The heat source acts for $t \leq 1$.

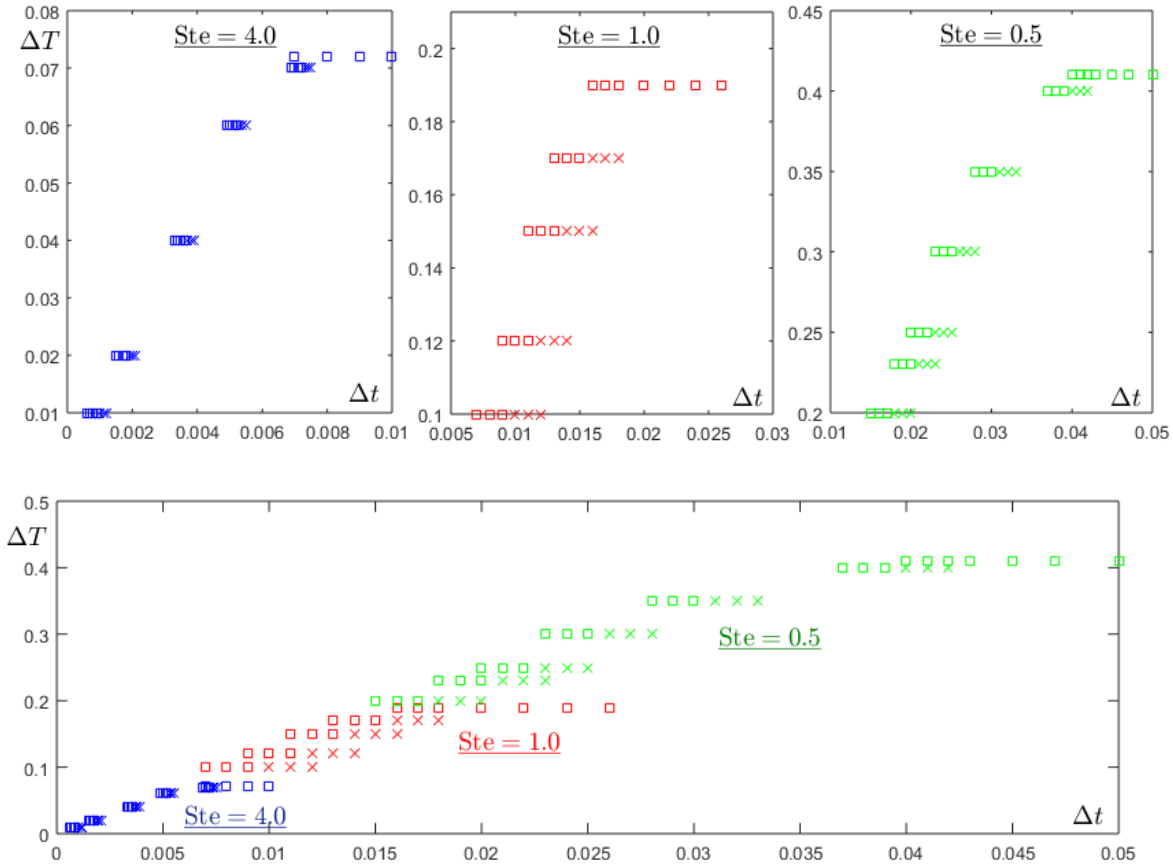

Figure 2.10: Convergence study of the θ-method. Legend: ($\times$) method failed; ($\square$) method succeeded.

Chapter 3

Comparison of Enthalpy Methods for Stefan Problems

3.1 Introduction

To begin, this Chapter 3 of this thesis is totally based in the article ready to submit: M. Colera, M. Freire-Torres, J. Carpio. "Comparison of implicit enthalpy methods for Stefan problems".

Stefan problems, or problems involving phase change, are present in many fields of science and engineering, such as welding of metallic alloys (Nedjar 2002; Bermúdez and Otero 2004; Anca et al. 2011; Piekarska and Kubiak 2011; Piekarska and Kubiak 2013; Freire-Torres et al. 2023), ice melting (Hutter et al. 1990; Sleptsov et al. 2018), chemical etching (Vuik and Cuvelier 1985), evaporation of droplets (Mitchell et al. 2011; Muelas et al. 2020), dendritic solidification (Fried and Veeser 2001), cryosurgical treatment of tumors (Pudjaprasetya 2013) and desalination of sea ice (Griewank and Notz 2013). These problems are characterized by the presence of one or several moving boundaries that separate the coexisting phases, and whose positions are not known a priori. Also, depending on the conditions of the problem, there may exist a zone, called *mushy region* (Atthey 1975), in which the physical body is still experimenting the phase change.

Although there are theoretical results for some specific problems (Gupta 2018), in general one must resource to numerical methods in order to find a solution. Depending on how the phase change boundaries are treated, the methods are divided in two families (Piqueras et al. 2020; Prakash et al. 2021). First, we distinguish *front-tracking* methods, in which the position of the moving boundary is updated continuously, e.g. the variable space grid method (Kutluay et al. 1997) and the heat balance integral method (Caldwell and Chan 2000). The main disadvantage of these methods is that remeshing is needed, and that they are more difficult to apply when there is a mushy region or when the change of phase is not isothermal (Nedjar 2002).

Secondly, *fixed-mesh* methods do not need to explicitly track the moving boundaries. Instead, the location of the phase front is obtained from the values of the solution, e.g. from the

enthalpy. For instance, boundary immobilization methods (Kutluay and Esen 2004; Mitchell and Vynnycky 2014; Piqueras et al. 2020) transform the problem equation in such a way that the phase interface remains fixed, and isotherm migration methods (Kutluay and Esen 2004) write the variables as functions of time and temperature, instead of time and space. These methods may not be adequate if the variables involved in the Stefan problem appear also in equations related to other physical processes. Effective specific heat methods (Piekarska and Kubiak 2011; Piekarska and Kubiak 2013) solve the classical heat equation –written in terms of the temperature– in the entire domain, replacing the specific heat by a fictitious coefficient –effective specific heat– that accounts for the latent heat released in the phase front. Heat-flow methods (Anca et al. 2011) also solve the classical heat equation in terms of the temperature in the entire domain, with the difference that they add a volumetric heat source involving the latent heat and depending on the liquid mass fraction. Conversely, enthalpy methods (Voller and Cross 1981; Voller 1990; Voller et al. 1990; Caldwell and Chan 2000; Casella and Giangi 2001; Caldwell and Kwan 2004; Esen and Kutluay 2004; Onyejekwe and Onyejekwe 2011; Tarwidi 2019; Nedjar 2002; Bermúdez and Otero 2004; Freire-Torres et al. 2023), make use of the enthalpy formulation of the Stefan problem (White 1982), which describes the process in the whole domain by means of a single heat equation relating enthalpy and temperature. It is shown in (Freire-Torres et al. 2023) that specific heat methods are not valid for isothermal phase change, and that enthalpy methods are always more robust than the former. Despite fixed-mesh methods may present oscillations at the phase fronts (Voller and Cross 1981), they are very simple to implement and do not require specific treatment of the phase front and/or the mushy region.

As said before, enthalpy methods solve a heat equation involving enthalpy and temperature. Hence, when they are combined with an implicit time-marching scheme, a nonlinear system of equations must be solved with an iterative procedure. This system is difficult to solve because the enthalpy is given by an ill-conditioned function of the temperature, especially in the case of isothermal phase change, in which this function is multivalued. Every enthalpy method has its own iterative solution algorithm. It is worth remarking that, despite all the enthalpy methods solve the same equation, not all of them consider the *enthalpy* as main variable for the iterative procedure, but other variables such as the temperature or Kirchhoff's variable, as we shall see in Section 3.3. Of course, the efficient solution of the nonlinear system of equations is critical for the overall performance of the scheme. However, despite there are some reviews comparing the performance of the different fixed-mesh methods discussed above for the Stefan problem, such as (Voller et al. 1990; Caldwell and Kwan 2004; Javierre et al. 2006; Nazzi Ehms et al. 2019; Prakash et al. 2021), we are not aware of any work specifically discussing this important point. Hence, in this work we aim to describe and compare three different nonlinear solvers for implicit enthalpy methods for the Stefan problem, namely, (i) the h-Newton method introduced recently by (Freire-Torres et al. 2023), (ii) Nedjar's scheme (Nedjar 2002) and (iii) Bermudez–Moreno algorithm (Bermúdez and Otero 2004; Bermúdez and Moreno 1981).

3.2 Governing equations

Hereafter, we focus on a two-phase model describing the melting process in a solid. The physical body is governed by the energy conservation equation

$$\frac{\partial(\rho h)}{\partial t} = \nabla \cdot (\lambda \nabla T) + Q, \qquad \text{in } \Omega, \tag{3.1}$$

with ρ the density (which we assume to be constant and equal for both liquid and solid phases), h the enthalpy per mass unit, λ the thermal conductivity, T the temperature, Q a volumetric heat source –e.g. a laser-arc source, which is able to internally heat the material due to the Joule effect (Piekarska and Kubiak 2011; Piekarska and Kubiak 2013)– and Ω the physical domain. Heat transport due to convection is neglected, assuming low Grashof number limit. Initially, the body is in solid state at ambient temperature, $T = T_0$. We prescribe Dirichlet and Neumann conditions at the boundaries Γ_D and Γ_N, respectively, with $\partial\Omega = \Gamma_D \cup \Gamma_N$, i.e.

$$T = T_0 \;\; \text{ on } \Gamma_D, \qquad \lambda \frac{\partial T}{\partial \mathrm{n}} = q \;\; \text{ on } \Gamma_N, \tag{3.2}$$

where q is the heat flux which goes inside the domain Ω through Γ_N. An infinitesimal variation of enthalpy, $\mathrm{d}h$, can be written as the sum of two contributions: (i) the variation in the sensible enthalpy $\mathrm{d}h_{\text{sen}} := c\,\mathrm{d}T$, with c the specific heat, which is due to the change in temperature, and (ii) the variation in the latent enthalpy $\mathrm{d}h_{\text{lat}} := H_F \mathrm{d}Y_L$, with H_F the latent heat of fusion and Y_L the mass fraction of liquid, which accounts for the energy necessary for the phase change; hence, $\mathrm{d}h = \mathrm{d}h_{\text{sen}} + \mathrm{d}h_{\text{lat}}$. Here we assume that melting takes places at a constant temperature T_F. According to the definitions above, this model is usually described as:

$$Y_L \in \mathcal{Y}(T) := \begin{cases} 0, & T < T_F, \\ [0,1], & T = T_F, \\ 1, & T > T_F, \end{cases} \tag{3.3a}$$

$$h \in \mathcal{H}(T) := \begin{cases} c_S(T - T_0), & T < T_F, \\ [h_S, h_L], & T = T_F, \\ h_L + c_L(T - T_F), & T > T_F, \end{cases} \tag{3.3b}$$

with c_S and c_L the values of c at the solid and liquid phases, which are assumed to be independent of T, $h_S := c_S(T_F - T_0)$ and $h_L = h_S + H_F$ the enthalpies of the solid and liquid states at the melting temperature, and $h = h_S + H_F Y_L$ for $T = T_F$.

Above, the notation $h \in [h_S, h_L]$ (likewise $Y_L \in [0,1]$) means that the enthalpy can take any value inside this interval for $T = T_F$, that is, the function $\mathcal{H}(T)$ is multivalued. This implies that the isothermal melting model can not be univocally described by temperature. To circumvent this drawback, enthalpy methods (Voller and Cross 1981; Voller 1990; Voller et al. 1990; Caldwell and Chan 2000; Casella and Giangi 2001; Caldwell and Kwan 2004; Esen and Kutluay 2004; Onyejekwe and Onyejekwe 2011; Tarwidi 2019; Nedjar 2002; Bermúdez and Otero 2004; Freire-Torres et al. 2023) describe the model in terms of the enthalpy, viz.,

$$Y_L = Y_L(h) := \begin{cases} 0, & h \le h_S, \\ (h - h_S)/H_F, & h_S < h < h_L, \\ 1, & h \ge h_L, \end{cases} \quad T = T(h) := \begin{cases} T_0 + h/c_S, & h \le h_S, \\ T_F, & h_S < h < h_L, \\ T_F + (h - h_L)/c_L, & h \ge h_L, \end{cases} \tag{3.4a, 3.4b}$$

so that the model is univocally described by this variable and the single-valued functions $Y_L(h)$ and $T(h)$.

In addition, we employ Kirchhoff's transformation (see for instance (Özisik 1989)) to simplify the diffusion term in (3.1), which is in general nonlinear due to the thermal conductivity λ. The transformation consists on introducing a new variable u defined so that $\mathrm{d}u = \lambda(T)\mathrm{d}T$, and therefore $\nabla \cdot (\lambda \nabla T) = \nabla^2 u$. In the present case,

$$u = U(T) := \begin{cases} \lambda_S(T - T_0), & T \le T_F, \\ \lambda_S(T_F - T_0) + \lambda_L(T - T_F), & T > T_F, \end{cases} \tag{3.5}$$

with λ_S and λ_L the values of λ at the solid and liquid states, which we assume for simplicity to be independent of T.

3.2.1 Non-dimensional formulation

To have a better understanding of the physics behind the present problem, it is convenient to formulate the equations in a non-dimensional form. In this way, we can study the order of magnitude of the different terms in the governing equations and analyze which are the relevant parameters –non-dimensional numbers– that characterize the problem. In particular, we introduce the following non-dimensional variables:

$$\mathbf{x}^* = \frac{\mathbf{x}}{L_0}, \quad t^* = \frac{\lambda_S}{\rho c_S L_0^2} t, \quad \theta = \frac{T - T_0}{T_F - T_0}, \quad u^* = \frac{u}{\lambda_S(T_F - T_0)}, \quad h^* = \frac{h}{c_S(T_F - T_0)},$$
$$Q^* = Q \frac{\rho L_0^2}{\lambda_S(T_F - T_0)}, \quad q^* = q \frac{L_0}{\lambda_S(T_F - T_0)}, \tag{3.6}$$

where L_0 is a characteristic length (e.g. the maximum edge of the domain). With the definitions above, Equation (3.1) and the corresponding initial and boundary conditions are written in dimensionless form as:

$$\begin{cases} \dfrac{\partial h^*}{\partial t^*} = \Delta^* u^* + Q^* & \text{in } \Omega, \\ \theta = 0 & \text{in } \Omega \text{ at } t = 0 \\ \theta = 0 & \text{on } \Gamma_D \ \forall t \\ \dfrac{\partial u^*}{\partial \mathrm{n}} = q^* & \text{on } \Gamma_N \ \forall t \end{cases} \tag{3.7}$$

There is one more dimensionless number of transcendental importance in phase-change problems: the Stefan number, Ste, which is defined as the ratio of sensible heat to latent heat,

$$\mathrm{Ste} = \frac{c_S(T_F - T_0)}{H_F}. \tag{3.8}$$

Equations (3.3)-(3.4) read then:

$$Y_L \in \mathcal{Y}(\theta) = \begin{cases} 0, & \theta < 1, \\ [0,1], & \theta = 1, \\ 1, & \theta > 1, \end{cases} \tag{3.9a}$$

$$h^* \in \mathcal{H}(\theta) = \begin{cases} \theta, & \theta < 1, \\ \left[1, 1 + \dfrac{1}{\mathrm{Ste}}\right], & \theta = 1, \\ 1 + \dfrac{1}{\mathrm{Ste}} + \dfrac{c_L}{c_S}(\theta - 1), & \theta > 1, \end{cases} \tag{3.9b}$$

$$Y_L = Y_L(h^*) := \begin{cases} 0, & h^* \leq 1, \\ \mathrm{Ste}\,(h^* - 1), & 1 < h^* < 1 + \dfrac{1}{\mathrm{Ste}}, \\ 1, & h^* \geq 1 + \dfrac{1}{\mathrm{Ste}}, \end{cases} \tag{3.10a}$$

$$\theta = \Theta(h^*) = \begin{cases} h^*, & h^* \leq 1 \\ 1, & 1 < h^* < 1 + \dfrac{1}{\mathrm{Ste}}, \\ \left(h^* - 1 - \dfrac{1}{\mathrm{Ste}}\right)\dfrac{c_S}{c_L} + 1, & h^* \geq 1 + \dfrac{1}{\mathrm{Ste}}, \end{cases} \tag{3.10b}$$

whereas Kirchhoff's variable reads,

$$u^* = U(\theta) = \begin{cases} \theta, & \theta \leq 1, \\ \dfrac{\lambda_L}{\lambda_S}(\theta - 1) + 1, & \theta > 1. \end{cases} \tag{3.11}$$

Hereafter, we drop the asterisk (*) symbol so as not to overload the notation, and all the variables will be dimensionless unless otherwise stated.

3.2.2 Numerical discretization of the problem

Once the mathematical model has been formulated, we design an algorithm based on a second-order time-marching scheme in combination with second-order local adaptative finite element discretization in space. More specifically, we first split the time interval of integration $[0,\ t_f]$ into subintervals $[t_{n-1},\ t_n]$ of constant length $\Delta t = t_n - t_{n-1}$. Then, we discretize (3.7) with a BDF2 formula:

$$\frac{3h^n - 4h^{n-1} + h^{n-2}}{2\Delta t} = \Delta u^n + Q^n, \quad \text{in } \Omega, \tag{3.12}$$

for $n = 2, ..., N_t$, with $N_t \Delta t = t_f$. At each time level t^n, the domain Ω is partitioned into a triangular mesh $\mathbb{T}_h^n$, to which we associate the conforming finite element space

$$V_{h0}^n = \{\varphi_h \in C^0(\mathbb{R}^2) : \varphi_h|_K \in P_2(K), \ \ \forall K \in \mathbb{T}_h^n \ \text{ and } \ \varphi_h|_{\Gamma_D} = 0\}, \tag{3.13}$$

where $P_2(K)$ is the space of quadratic polynomials on an element K. That is, V_{h0}^n is the space of continuous and quadratic polynomials (defined piecewise at the mesh elements) that vanish at the Dirichlet part of the boundary Γ_D. Note from (3.7), (3.10) and (3.11) that h, θ

and u also vanish at Γ_D, so V_{h0}^n can be used to approximate the solution. In particular, we approximate h^n, θ^n and u^n by

$$h_h^n(\mathbf{x}) = \sum_{i=1}^{N^n} h_i^n \varphi_{hi}(\mathbf{x}), \quad \theta_h^n(\mathbf{x}) = \sum_{i=1}^{N^n} \theta_i^n \varphi_{hi}(\mathbf{x}), \quad \text{and} \quad u_h^n(\mathbf{x}) = \sum_{i=1}^{N^n} u_i^n \varphi_{hi}(\mathbf{x}), \tag{3.14}$$

where N^n is the number of mesh nodes (excluding those at Γ_D), h_i^n, θ_i^n, and u_i^n are the values of the variables at these nodes, and $\varphi_{hi}(\mathbf{x})$ are the corresponding Lagrangian basis functions.

With the considerations above, (3.12) reads in weak form as follows: find h_h^n, θ_h^n and $u_h^n \in V_{h0}^n$ such that

$$\begin{aligned} &\frac{3}{2}\int_\Omega h_h^n \varphi_h d\mathrm{x} + \Delta t \int_\Omega \nabla u_h^n \cdot \nabla \varphi_h d\mathrm{x} = \\ &\Delta t \int_\Omega Q^n \varphi_h d\mathrm{x} + \Delta t \int_{\Gamma_N} q^n \varphi_h d\mathrm{s} + \int_\Omega (2h_h^{n-1} - \frac{1}{2}h_h^{n-2})\varphi_h d\mathrm{x}, \quad \forall \varphi_h \in V_{h0}^n. \end{aligned} \tag{3.15}$$

The latter can be rewritten in matrix form to simplify the notation:

$$\frac{3}{2}\mathbf{M}\,\mathbf{h}^n + \Delta t\ \mathbf{K}\,\mathbf{u}^n = \mathbf{f}^n, \tag{3.16}$$

where the bold variables are vectors or matrices whose elements are defined by

$$\begin{aligned} &M_{ij} = (\varphi_{hi}, \varphi_{hj})_\Omega, \quad K_{ij} = (\nabla\varphi_{hi}, \nabla\varphi_{hj})_\Omega, \\ &f_i^n = (\Delta t\, Q^n + 2h_h^{n-1} - \frac{1}{2}h_h^{n-2}, \varphi_{hi})_\Omega + (\Delta t\, q^n, \varphi_{hi})_{\Gamma_N}, \end{aligned} \tag{3.17}$$

and with $(\cdot\ ,\ \cdot)$ the standard scalar product in the L^2 norm. Note that, due to the introduction of Kirchhoff's variable (3.11), the stiffness matrix is constant (whenever the mesh remains fixed), which greatly simplifies the solution algorithm.

In order to allow for a better resolution of the phase fronts, we have employed local, anisotropic, mesh refinement techniques (Dolejší and May 2022). The main goal of these is to define, at each time level t^n, a mesh triangulation such that the solution is computed within a given accuracy and the number of nodes is minimal. The specific implementation details and fundamentals are described in our previous work (Freire-Torres et al. 2023, Section 3.2) and in more detail in (Carpio and Prieto 2014).

3.3 Nonlinear solvers for implicit enthalpy methods

Equation (3.16), which stems from the numerical discretization of the original problem (3.7), represents a nonlinear system of algebraic equations due to the relations between unknown

variables h_i^n, θ_i^n, and u_i^n. Next we describe three different approaches for the solution of the latter, namely, the h-Newton method introduced recently by the present authors in (Freire-Torres et al. 2023), (ii) Nedjar's scheme (Nedjar 2002) and (iii) Bermudez–Moreno algorithm (Bermúdez and Otero 2004; Bermúdez and Moreno 1981).

3.3.1 h-Newton method

The first scheme, introduced in our previous work (Freire-Torres et al. 2023), makes use of the fact that the state of the body is univocally defined by the enthalpy, as shown in Equation (3.10). Hence, we can consider the nodal enthalpies as main unknowns and apply a standard Newton method to solve Equation (3.7). Whenever required, the nodal values of θ_i^n and u_i^n are computed from Equations (3.10b) and (3.11). In particular, the value of $\boldsymbol{h}_{(k+1)}^n$ at the iteration $k+1$ is obtained by solving

$$\mathbf{A}_{\mathrm{Nw}(k)}^n \boldsymbol{\Delta h}_{(k)}^n = -\mathbf{b}_{\mathrm{Nw}(k)}^n, \quad \boldsymbol{h}_{(k+1)}^n = \boldsymbol{h}_{(k)}^n + \boldsymbol{\Delta h}_{(k)}^n, \tag{3.18}$$

where the residual vector $\mathbf{b}_{\mathrm{Nw}(k)}^n$ and the Jacobian matrix $\mathbf{A}_{\mathrm{Nw}(k)}^n$ are obtained from (3.16), i.e.

$$\begin{cases} \mathbf{b}_{\mathrm{Nw}(k)}^n &= \frac{3}{2}\mathbf{M}\,\mathbf{h}_{(k)}^n + \Delta t\,\mathbf{K}\,\mathbf{u}_{(k)}^n - \mathbf{f}^n, \\ \mathbf{A}_{\mathrm{Nw}(k)}^n &= \frac{3}{2}\mathbf{M} + \Delta t\,\mathbf{K}\,\mathbf{D}_{\mathrm{Nw}(k)}^u, \end{cases} \tag{3.19}$$

$\mathbf{D}_{\mathrm{Nw}(k)}^u$ is the diagonal matrix is obtained from:

$$D_{\mathrm{Nw}(k),ij}^u = \left.\frac{du}{dh}\right|_{h_{(k),i}^n} \delta_{ij}, \tag{3.20}$$

and δ_{ij} is the Kronecker delta. The values of the derivatives in Equation (3.20) are obtained by applying the chain rule, which yields:

$$\frac{du}{dh} = \frac{du}{d\theta}\frac{d\theta}{dh} = \begin{cases} 1, & h \leq 1 \\ 0, & 1 < h < 1 + \dfrac{1}{\mathrm{Ste}}, \\ \dfrac{c_S}{c_L}\dfrac{\lambda_L}{\lambda_S}, & h \geq 1 + \dfrac{1}{\mathrm{Ste}}. \end{cases} \tag{3.21}$$

The h-Newton method is summarized in Algorithm 1.

Note from Equation (3.19) that, to update the Jacobian at each iteration, we only need to update the diagonal matrix $\mathbf{D}_{\mathrm{Nw}(k)}^u$ and to accordingly combine the columns of the mass and stiffness matrices $\mathbf{M}$ and $\mathbf{K}$. Hence, this operation has a negligible computational cost. However, unlike $\mathbf{M}$ and $\mathbf{K}$, the resulting Jacobian matrix is no longer symmetric, so one has to resource to iterative methods to solve (3.18) like BICGSTAB preconditioned with the diagonal.

Algorithm 1 h-Newton method

Data: $\mathbf{h}^{n-1}, \mathbf{h}^{n-2}$, Tol;
Result: $\mathbf{h}^n$, $\boldsymbol{\theta}^n$, $\mathbf{u}^n$;
initialize $\mathbf{h}^n_{(0)} = \mathbf{h}^{n-1}$, error $= +\infty$, $k = 0$;
evaluate $\boldsymbol{\theta}^n_{(0)} = \Theta(\boldsymbol{h}^n_{(0)})$, $\mathbf{u}^n_{(0)} = U(\boldsymbol{\theta}^n_{(0)})$;
while error $>$ Tol **do**
    solve $\mathbf{A}^n_{\mathrm{Nw}(k)}\ \boldsymbol{\Delta h}^n_{(k)} = -\mathbf{b}^n_{\mathrm{Nw}(k)}$;
    update $\mathbf{h}^n_{(k+1)} = \mathbf{h}^n_{(k)} + \boldsymbol{\Delta h}^n_{(k)}$;
    update $\boldsymbol{\theta}^n_{(k+1)} = \Theta(\boldsymbol{h}^n_{(k+1)})$;
    update $\mathbf{u}^n_{(k+1)} = U(\boldsymbol{\theta}^n_{(k+1)})$;
    calculate error $= \left\|\mathbf{b}^n_{\mathrm{Nw}(k)}\right\|_2$;
    increase $k = k + 1$;
end while
update $\mathbf{h}^n = \mathbf{h}^n_{(k)},\ \boldsymbol{\theta}^n = \boldsymbol{\theta}^n_{(k)},\ \mathbf{u}^n = \mathbf{u}^n_{(k)}$;

3.3.2 Nedjar's scheme

The second scheme was introduced by Nedjar in (Nedjar 2002). It is based the following linearization of Equation (3.10b):

$$\boldsymbol{\theta}^n_{(k+1)} = \boldsymbol{\theta}^n_{(k)} + \boldsymbol{\Delta\theta}^n_{(k)} = \Theta(\boldsymbol{h}^n_{(k)}) + \Theta'(\boldsymbol{h}^n_{(k)})\boldsymbol{\Delta h}^n_{(k)}, \tag{3.22}$$

which is equivalent to

$$\boldsymbol{\Delta h}^n_{(k)} = \frac{1}{\Theta'(\boldsymbol{h}^n_{(k)})}[\boldsymbol{\Delta\theta}^n_{(k)} + (\boldsymbol{\theta}^n_{(k)} - \Theta(\boldsymbol{h}^n_{(k)}))]. \tag{3.23}$$

This linearization is problematic at the melting point because of the factor $[\Theta'(\boldsymbol{h}^n_{(k)})]^{-1}$. Hence, it is relaxed by replacing the latter factor by a quantity μ constant in the entire domain and during the whole iterative process (Nedjar 2002), that is,

$$\boldsymbol{\Delta h}^n_{(k)} = \mu[\boldsymbol{\Delta\theta}^n_{(k)} + (\boldsymbol{\theta}^n_{(k)} - \Theta(\boldsymbol{h}^n_{(k)}))]. \tag{3.24}$$

Following (Nedjar 2002), we consider $\mu = \min\{1,\ c_L/c_S\}$. Similarly,

$$\boldsymbol{\Delta u}^n_{(k)} = \mathbf{D}^u_{\mathrm{Nd}(k)}\boldsymbol{\Delta\theta}^n_{(k)}, \quad D^u_{\mathrm{Nd}(k),ij} = \left.\frac{du}{d\theta}\right|_{\theta^n_{(k),i}} \delta_{ij}. \tag{3.25}$$

Now we seek an increment of temperature such that:

$$\frac{3}{2}\mathbf{M}\ (\mathbf{h}^n_{(k)} + \boldsymbol{\Delta}\mathbf{h}^n_{(k)}) + \Delta t\mathbf{K}\ (\mathbf{u}^n_{(k)} + \boldsymbol{\Delta}\mathbf{u}^n_{(k)}) - \mathbf{f}^n = 0. \tag{3.26}$$

If we substitute Equations (3.24)-(3.25) in the equation above, we arrive at an iteration of the form

$$\mathbf{A}^n_{\mathrm{Nd}(k)}\boldsymbol{\Delta\theta}^n_{(k)} = -\mathbf{b}^n_{\mathrm{Nd}(k)}, \quad \boldsymbol{\theta}^n_{(k+1)} = \boldsymbol{\theta}^n_{(k)} + \boldsymbol{\Delta\theta}^n_{(k)}, \tag{3.27}$$

where the residual vector $\mathbf{b}^n_{\mathrm{Nd}(k)}$ and the Jacobian matrix $\mathbf{A}^n_{\mathrm{Nd}(k)}$ are given by

$$\begin{cases} \mathbf{b}^n_{\mathrm{Nd}(k)} & = \frac{3}{2}\mathbf{M}\ \mathbf{h}^n_{(k)} + \Delta t\,\mathbf{K}\ \mathbf{u}^n_{(k)} - \mathbf{f}^n + \frac{3}{2}\mathbf{M}\mu(\boldsymbol{\theta}^n_{(k)} - \Theta(\mathbf{h}^n_{(k)})), \\ \mathbf{A}^n_{\mathrm{Nd}(k)} & = \frac{3}{2}\mu\mathbf{M} + \Delta t\,\mathbf{K}\ \mathbf{D}^u_{\mathrm{Nd}(k)}. \end{cases} \tag{3.28}$$

Nedjar's algorithm is presented schematically in Algorithm 2.

Algorithm 2 Nedjar's algorithm

Data: $\mathbf{h}^{n-1}$, $\mathbf{h}^{n-2}$, Tol, μ;
Result: $\mathbf{h}^n$, $\boldsymbol{\theta}^n$, $\mathbf{u}^n$;
initialize $\mathbf{h}^n_{(0)} = \mathbf{h}^{n-1}$, error $= +\infty$, $k = 0$;
evaluate $\boldsymbol{\theta}^n_{(0)} = \Theta(\boldsymbol{h}^n_{(0)})$, $\mathbf{u}^n_{(0)} = U(\boldsymbol{\theta}^n_{(0)})$;
while error $>$ Tol **do**
    solve $\mathbf{A}^n_{\mathrm{Nd}(k)}\ \boldsymbol{\Delta\theta}^n_{(k)} = -\mathbf{b}^n_{\mathrm{Nd}(k)}$;
    update $\mathbf{h}^n_{(k+1)} = \mathbf{h}^n_{(k)} + \mu[\boldsymbol{\Delta\theta}^n_{(k)} + (\boldsymbol{\theta}^n_{(k)} - \ \Theta(\boldsymbol{h}^n_{(k)}))]$;
    update $\boldsymbol{\theta}^n_{(k+1)} = \boldsymbol{\theta}^n_{(k)} + \boldsymbol{\Delta\theta}^n_{(k)}$;
    update $\mathbf{u}^n_{(k+1)} = U(\boldsymbol{\theta}^n_{(k+1)})$;
    calculate error $= \|\mathbf{b}^n_{\mathrm{Nd}(k)}\|_2$;
    increase $k = k + 1$;
end while
update $\mathbf{h}^n = \mathbf{h}^n_{(k)}$, $\boldsymbol{\theta}^n = \boldsymbol{\theta}^n_{(k)}$, $\mathbf{u}^n = \mathbf{u}^n_{(k)}$;

3.3.3 Bermúdez–Moreno algorithm

A full explanation of the Bermúdez–Moreno algorithm and its detailed mathematical background can be found in (Bermúdez and Otero 2004; Bermúdez and Moreno 1981; Parés et al. 2002). Here, we only give a description of the fundamental ideas for its understanding and application. The algorithm is based on applying the Yosida regularization for multivalued operators. In particular, we start by computing the enthalpy as a function of Kirchhoff's variable, i.e.

$$h \in \mathcal{A}(u) := \mathcal{H}(U^{-1}(u)) = \begin{cases} u, & u < 1, \\ [1, 1 + 1/\mathrm{Ste}], & u = 1, \\ \left(1 + \dfrac{1}{\mathrm{Ste}}\right) + \dfrac{c_L}{c_S}\dfrac{\lambda_S}{\lambda_L}(u-1), & u > 1, \end{cases} \tag{3.29}$$

which results from manipulating Equations (3.9b) and (3.11). Note that the function $\mathcal{A}(u)$ is multivalued at $u = 1$.

We define a new variable $\beta = h^n - \omega u^n$, with $\omega > 0$ a user-defined parameter. This is equivalent to

$$\beta \in \mathcal{A}(u^n) - \omega u^n = (\mathcal{A} - \omega I)\, u^n := \mathcal{A}^\omega(u^n). \tag{3.30}$$

Then, we apply Yosida regularization to the multivalued operator $\mathcal{A}^\omega$:

$$A^\omega_\lambda(x) := \frac{x - [I + \lambda \mathcal{A}^\omega]^{-1}(x)}{\lambda}, \tag{3.31}$$

with $\lambda > 0$ another user-defined parameter. The regularized operator A^ω_λ is single-valued and reads, after some algebraic manipulations,

$$A^\omega_\lambda(x) = \begin{cases} \dfrac{(1-\omega)x}{1+\lambda(1-\omega)}, & x \leq 1 + \lambda(1-\omega), \\ \dfrac{x-1}{\lambda}, & 1 + \lambda(1-\omega) < x < 1 + \lambda\left(1 + \dfrac{1}{\mathrm{Ste}} - \omega\right), \\ \dfrac{(x-1)\left(\dfrac{\lambda_S}{\lambda_L}\dfrac{c_L}{c_S} - \omega\right) + \left(1 + \dfrac{1}{\mathrm{Ste}} - \omega\right)}{1 + \lambda\left(\dfrac{\lambda_S}{\lambda_L}\dfrac{c_L}{c_S} - \omega\right)}, & x \geq 1 + \lambda\left(1 + \dfrac{1}{\mathrm{Ste}} - \omega\right). \end{cases} \tag{3.32}$$

It is easy to verify that, following the definitions above,

$$\beta \in \mathcal{A}^\omega(u^n) \iff \beta = A^\omega_\lambda(u^n + \lambda\beta). \tag{3.33}$$

The latter relation is the keystone for the construction of the iterative Bermúdez–Moreno algorithm, because it implies that the solution of Equation (3.30), which seems difficult to be computed due to the multivalued character of $\mathcal{A}^\omega$, can indeed be found as the solution of the fixed point iteration $\beta = A^\omega_\lambda(u^n + \lambda\beta)$. The latter is guaranteed to converge if $\lambda\omega \leq 0.5$, so in practical cases we simply take $\lambda\omega = 0.5$ in order to have only one parameter.

Now we are able to pose Equation (3.16) in such a way that no multivalued operators appear. In particular, recalling that $\mathbf{h}^n = \boldsymbol{\beta} + \omega \mathbf{u}^n$, we have

$$\begin{cases} \frac{3}{2}\mathbf{M}\,(\boldsymbol{\beta} + \omega \mathbf{u}^n) + \Delta t \mathbf{K}\,\mathbf{u}^n = \mathbf{f}^n \\ \boldsymbol{\beta} = A^\omega_\lambda(\mathbf{u}^n + \lambda\boldsymbol{\beta}). \end{cases} \tag{3.34}$$

The latter equation is solved with the fixed point iteration

$$\mathbf{A}^n_{\mathrm{BM}} \boldsymbol{\Delta u}^n_{(k)} = -\mathbf{b}^n_{\mathrm{BM}(k)}, \quad \boldsymbol{u}^n_{(k+1)} = \boldsymbol{u}^n_{(k)} + \boldsymbol{\Delta u}^n_{(k)}, \quad \boldsymbol{\beta}_{(k+1)} = A^\omega_\lambda(\mathbf{u}^n_{(k+1)} + \lambda \boldsymbol{\beta}_{(k)}), \tag{3.35}$$

where the residual vector $\mathbf{b}^n_{\mathrm{BM}(k)}$ and the Jacobian matrix $\mathbf{A}^n_{\mathrm{BM}(k)}$ are given by

$$\begin{cases} \mathbf{b}^n_{\mathrm{BM}(k)} &= \frac{3}{2}\mathbf{M}\ (\boldsymbol{\beta} + \omega\mathbf{u}^n) + \Delta t\mathbf{K}\ \mathbf{u}^n_{(k)} - \mathbf{f}^n, \\ \mathbf{A}^n_{\mathrm{BM}} &= \frac{3}{2}\omega\mathbf{M} + \Delta t\mathbf{K}. \end{cases} \tag{3.36}$$

The Bermúdez–Moreno scheme is summarized in Algorithm 3.

Algorithm 3 Bermúdez–Moreno algorithm

Data: $\mathbf{h}^{n-1}$, $\mathbf{h}^{n-2}$, Tol, ω, $\lambda = 0.5/\omega$;
Result: $\mathbf{h}^n$, $\boldsymbol{\theta}^n$, $\mathbf{u}^n$;
initialize $\mathbf{h}^n_{(0)} = \mathbf{h}^{n-1}$, error $= +\infty$, $k = 0$;
evaluate $\boldsymbol{\theta}^n_{(0)} = \Theta(\boldsymbol{h}^n_{(0)})$, $\mathbf{u}^n_{(0)} = U(\boldsymbol{\theta}^n_{(0)})$, $\boldsymbol{\beta}_{(0)} = \mathbf{h}^n_{(0)} - \omega\mathbf{u}^n_{(0)}$;
while error $>$ Tol **do**
    solve $\mathbf{A}^n_{\mathrm{BM}}\ \boldsymbol{\Delta u}^n_{(k)} = -\mathbf{b}^n_{\mathrm{BM}(k)}$;
    update $\mathbf{u}^n_{(k+1)} = \mathbf{u}^n_{(k)} + \boldsymbol{\Delta u}^n_{(k)}$;
    update $\boldsymbol{\beta}_{(k+1)} = A^{\omega}_{\lambda}(\mathbf{u}^n_{(k+1)} + \lambda\boldsymbol{\beta}_{(k)})$;
    update $\boldsymbol{h}^n_{(k+1)} = \boldsymbol{\beta}_{(k+1)} + \omega\mathbf{u}^n_{(0)}$;
    update $\boldsymbol{\theta}^n_{(k+1)} = \Theta(\mathbf{h}^n_{(k+1)})$;
    calculate error $= \|\mathbf{b}^n_{\mathrm{BM}(k)}\|_2$;
    increase $k = k + 1$;
end while
update $\mathbf{h}^n = \mathbf{h}^n_{(k)}$, $\boldsymbol{\theta}^n = \boldsymbol{\theta}^n_{(k)}$, $\mathbf{u}^n = \mathbf{u}^n_{(k)}$;

The convergence of the Bermúdez–Moreno algorithm is usually slow, although the authors claim that the iterations are not very costly because the matrix $\mathbf{A}^n_{\mathrm{BM}}$ does not need to be recomputed at each iteration, and therefore it can be assembled and factorized only once at the beginning of the loop. In Carlos Parés et. al. (Parés et al. 2001; Parés et al. 2002) an effort was made to determine the optimal parameters λ and ω for which the algorithm has a higher convergence rate –considering also the case in which these parameters are replaced by space-time dependent functions–, but the results are not completely satisfactory.

3.4 Numerical results

To assess the performance of the three nonlinear solvers introduced in Section 3.3 for the solution of Stefan problem, we solve some tests in a rectangular domain $\Omega = [0, 2.5] \times [-1, 0]$, with boundary $\partial\Omega \equiv \Gamma_1 \cup \Gamma_2 \cup \Gamma_3 \cup \Gamma_4$, as can be seen in Figure 3.1. The numerical integration will take place for $0 \leq t \leq 2.5$ with a time step $\Delta t = 0.01$, and the dimensionless numbers relating the specific heat coefficient and thermal conductivity in the liquid and solid phases are

$$c_S/c_L = 0.75, \quad \lambda_S/\lambda_L = 1.5. \tag{3.37}$$

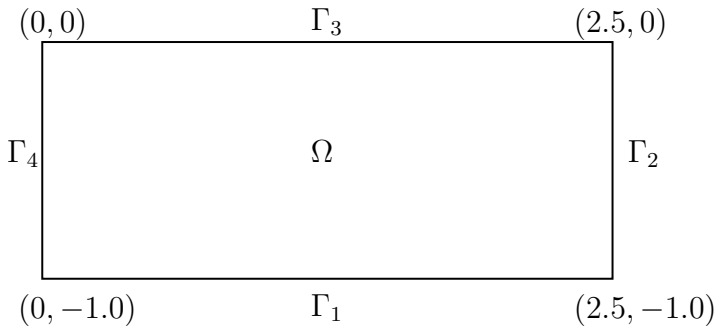

Figure 3.1: Domain and boundaries associated with the welding problem.

We consider two Stefan problems. The first one is characterized by a prescribed heat-flux q at the Neumann boundary, whereas the second is governed by a moving volumetric heat source Q. The first test shows a discontinuity between the solid and liquid zone, while the second test present a *mushy region* (Atthey 1975), a transient zone where the liquid and solid phases coexist, i.e. $0 < Y_L < 1$. We recall that the phase fronts that characterize the Stefan problem are given by the conditions $Y_L = 0$ or $Y_L = 1$, and that the liquid mass fraction can be computed from the enthalpy via Equation (3.10a).

The tests were carried out on an i7-8700 CPU computer with 16GB DDR3 RAM @1.3 GHz under Ubuntu 20.02.4 LTS operating system, and the codes were written in C programming language. In addition, an anisotropic mesh adaptation was used, as detailed in (Carpio and Prieto 2014; Carpio et al. 2016; Carpio et al. 2019; Freire-Torres and Carpio 2023).

3.4.1 Test I: Prescribed heat flux on the boundary

In the first test, a solid is initially at ambient temperature $\theta = 0$, and then a heat flux $q = 2$ is applied on the left boundary Γ_4. Additionally, we impose $q = 0$ on the horizontal boundaries, Γ_1 and Γ_3, and ambient temperature $\theta = 0$ on the right boundary Γ_2.

Due to the heat flux at $x_1 = 0$, the temperature of the solid at this location increases until some time t_m, when the melting temperature $\theta = 1$ is reached. Then, the liquid begins to form and, consequently, also a melting front $x_1 = X_{1m}(t)$ that travels to the right and that separates the liquid from the solid. We can observe this behavior in Figure 3.2, where the solution is plot for three different Stefan numbers and several instants of time. There is no mushy region at which liquid and solid coexist, but a sharp transition from solid to liquid across the phase front. Also note that the velocity of the moving front increases when the Stefan number is larger (or, equivalently, the latent heat of fusion H_F is smaller).

Figure 3.3 shows the mesh at time $t = 2$ for the case $\mathrm{Ste} = 0.25$, as well as a detail of the latter at the melting zone so we can observe its anisotropic character. The evolution of the number of mesh elements $\mathrm{NE}(t)$ with time is also shown. It is interesting to note that NE suddenly increases at $t = t_m$ due to the apparition of the melting front.

Now, we focus on the behavior of the three nonlinear solvers described in previous sections for the case of Test I. First, we consider $\omega = 5$ for the Bermúdez–Moreno algorithm, $\mu =$

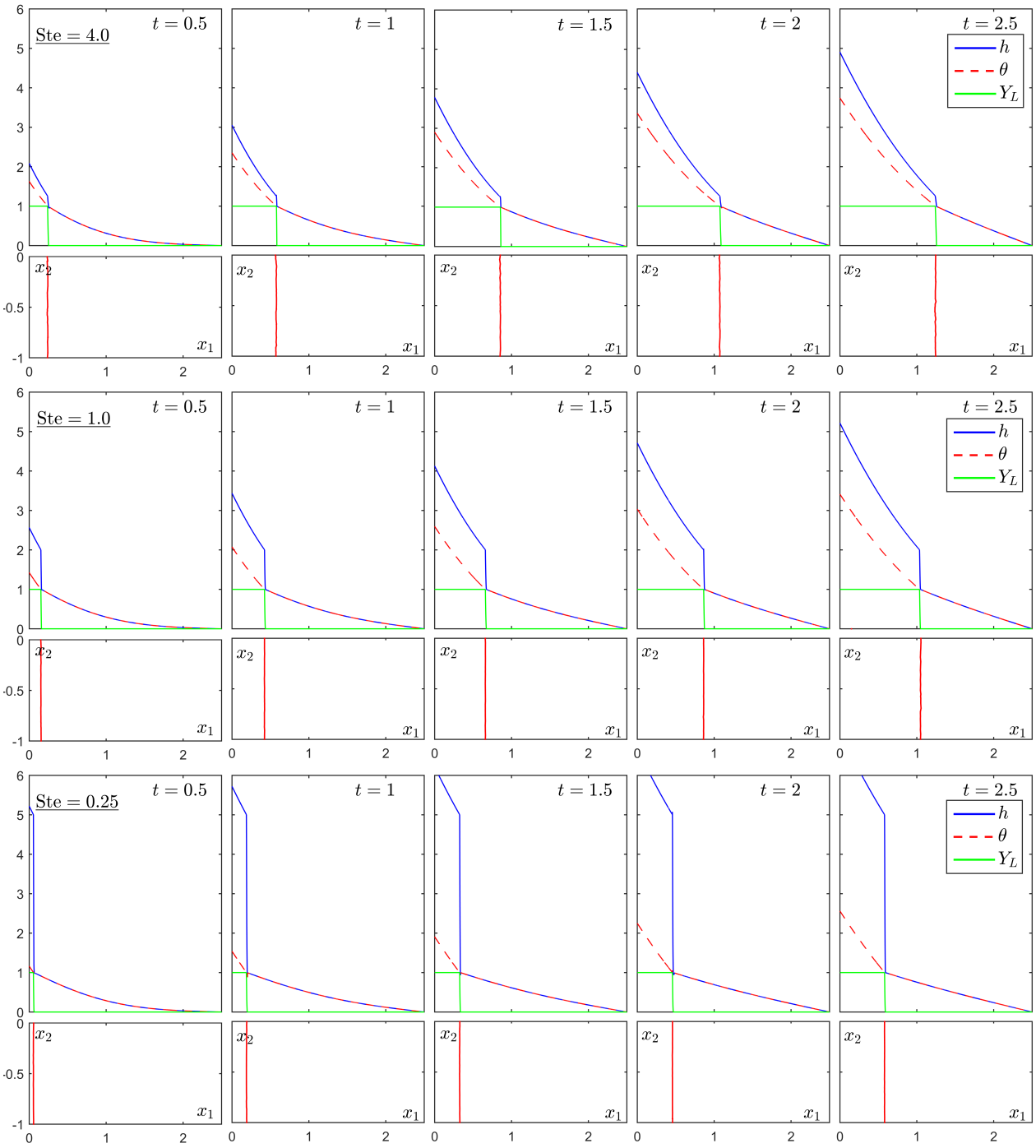

Figure 3.2: Numerical solutions of Test I obtained for different values of the Stefan number. The upper panels show the profiles of the thermodynamic variables along the line $x_2 = -0.5$, whereas the lower panels show the location of the phase front.

$\min\{1,\ c_L/c_S\} = 1$ for the Nedjar's scheme and the h-Newton method is parameter-free method. We study the number of iterations necessary to achieve a tolerance $\mathrm{Tol} = 10^{-7}$. As

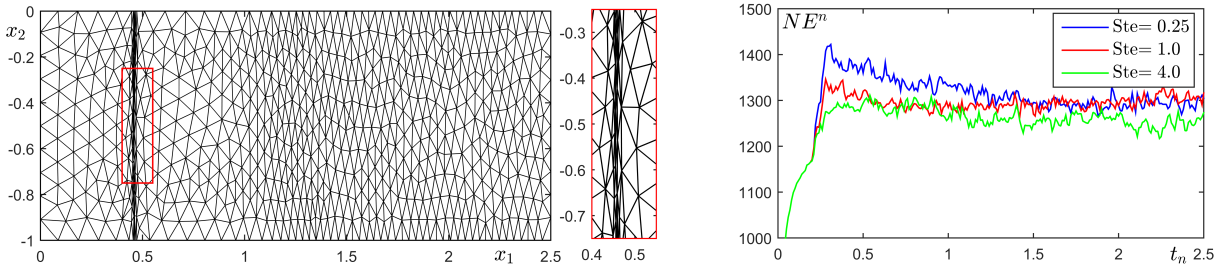

Figure 3.3: (Left): anisotropic mesh at time $t = 2.0$ for the case Ste= 0.25. (Right): evolution of the number of elements NE(t) with anisotropic mesh adaptation for different Stefan numbers.

can be seen in Figure 3.4, the number of iterations required by the Nedjar and Bermúdez–Moreno algorithms is much larger than that of the h-Newton. Moreover, with the Nedjar and Bermúdez–Moreno algorithms the number of iterations increases when the Stefan number is smaller (since the latter implies a higher jump in the enthalpies at the melting temperature, and therefore the nonlinearities are more relevant). Conversely, the h-Newton algorithm requires only about 4-6 iterations irrespective of the Stefan number.

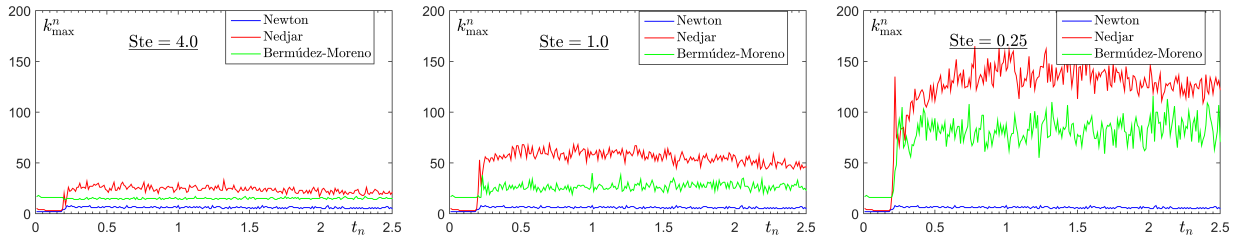

Figure 3.4: Number of required iterations at each time level for the h-Newton, Nedjar (with $\mu = 1$) and Bermúdez–Moreno (with $\omega = 5$) algorithms.

Furthermore, Figure 3.5 plots the norm of the residual for each iteration of the nonlinear solvers, for the case Ste $= 0.25$ and $t_n = 1$. It is observed that Nedjar and Bermúdez–Moreno algorithm converge very slowly, something expectable because relaxed Newton methods and fixed point iterations have only linear convergence (Parés et al. 2002; Walker and Ni 2011). In contrast, the h-Newton method converges quadratically and thus the residual decreases very quickly.

An unfortunate feature of the Nedjar and Bermúdez–Moreno algorithms is that they depend on a parameter (μ and ω, respectively), which have a great influence in the number of required iterations. To illustrate this point, Figure 3.6 represents the total number of iterations –i.e. the sum of required iterations at each solved time level– against the parameters μ^{-1} and ω. For the Nedjar algorithm the value $\mu = \min\{1,\ c_L/s_S\} = 1$ leads to the minimum of iterations for this method as in (Nedjar 2002) claim, values lightly larger than 1 makes that the algorithm does not converge (for instance $\mu = 1.5$). The Bermúdez–Moreno algorithm is also very sensitive to the parameter ω (Parés et al. 2001). There is an optimal value of ω, which depends on the problem and on the Stefan number, for which the total number of

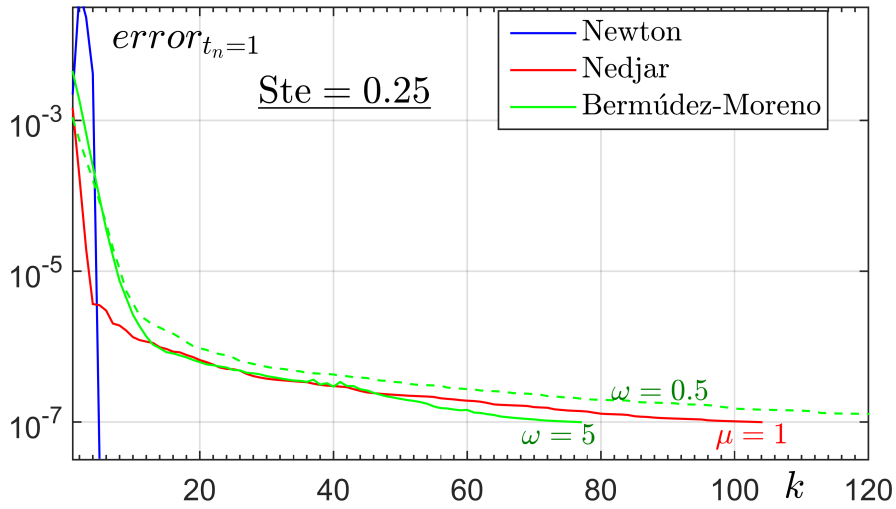

Figure 3.5: Residual norm at each iteration for the h-Newton, Nedjar (with $\mu = 1$) and Bermúdez–Moreno (with $\omega = 0.5$ and $\omega = 5$) algorithms for Ste $= 0.25$ and $t_n = 1$.

iterations is minimal. If ω is close to this optimal value, the Bermúdez–Moreno algorithm outperforms Nedjar's method; however, the h-Newton method still requires far less iterations.

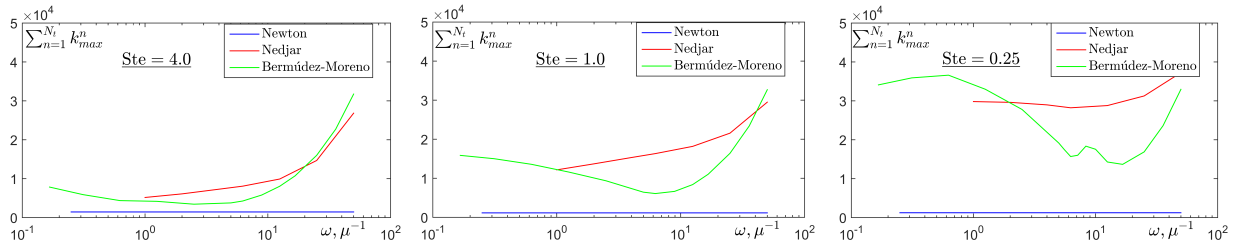

Figure 3.6: Total number of iterations as a function of μ^{-1} and ω in the Nedjar and Bermúdez-Moreno algorithm, respectively. The iterations of the h-Newton method (that does not depend on any parameter) is also plotted.

3.4.2 Test II: Volumetric heat source

In Test II, we consider a solid body (initially at ambient temperature) whose temperature at the left and right boundaries is kept constant and equal to the ambient one, i.e. $\theta = 0$ on $\Gamma_D \equiv \Gamma_2 \cup \Gamma_4$ and the rest of them adiabatic boundary condition $q = 0$ on $\Gamma_N \equiv \Gamma_1 \cup \Gamma_3$. For $0 \leq t \leq 1.5$, the solid is heated by a source Q that moves from left to the right with a constant velocity $v^0 = 1.0$. At $1.5 < t \leq 2.5$, the source is switched off. That is,

$$Q(x_1, x_2, t) = \begin{cases} Q_0 \exp\left(-10\left(x_1 - (x_1^0 + v^0 t)\right)^2 - 20\left(x_2 - x_2^0\right)^2\right)\left(1 - e^{-5t}\right), & 0 \leq t \leq 1.5, \\ 0, & 1.5 < t \leq 2.5, \end{cases} \tag{3.38}$$

with $Q_0 = 20.0$, $v^0 = 1.0$, $x_1^0 = 0.5$ and $x_2^0 = -0.5$.

As we have analyzed in the previous test the effect of the Stefan number on the solution, now we only show the results for the case Ste = 0.25, in which the differences between the three nonlinear solvers are more remarkable.

Figure 3.7 represents the solution for different instants of time. Unlike Test I, now there exists a mushy region in which solid and liquid phases coexist, and therefore there are two free surfaces. As time goes on, the mushy region tends to disappear (as can be seen more clearly for $t > 1.5$, when the heat source is switched off); then, the transition between liquid and solid becomes more abrupt and a discontinuity appears for the enthalpy variable.

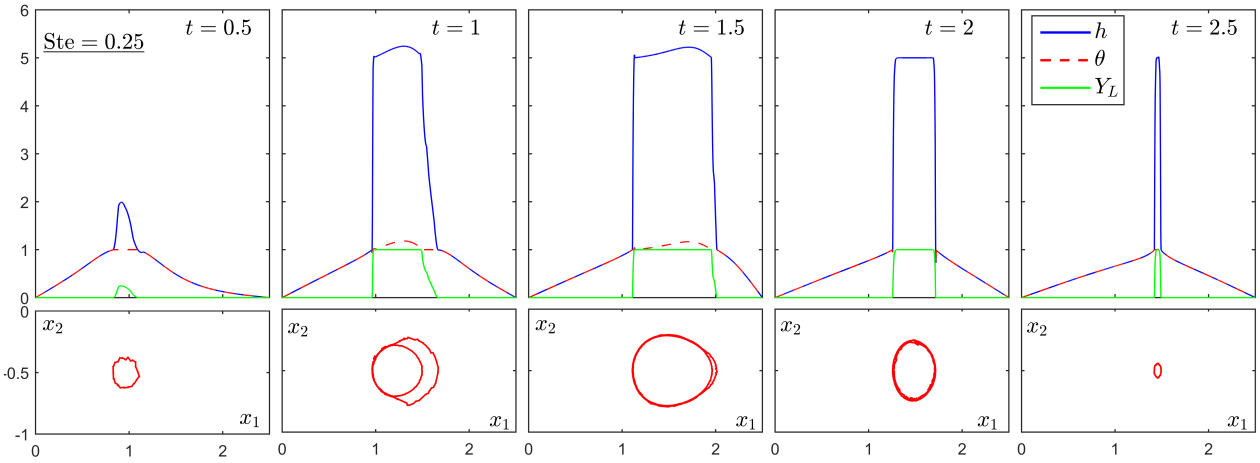

Figure 3.7: Numerical solutions of Test II obtained for Stefan number Ste= 0.25. The upper panels show the profiles of the thermodynamic variables along the line $x_2 = -0.5$, whereas the lower panels show the location of the phase front.

Furthermore, Figure 3.8 addresses the performance of each method. As happened with Test I, the number of iterations per solved time level is much smaller for the h-Newton method, since the convergence of the residual is much faster. Also, the Bermúdez–Moreno outperforms Nedjar's method when ω is close to the optimum; however, it still requires far more iterations than the h-Newton method.

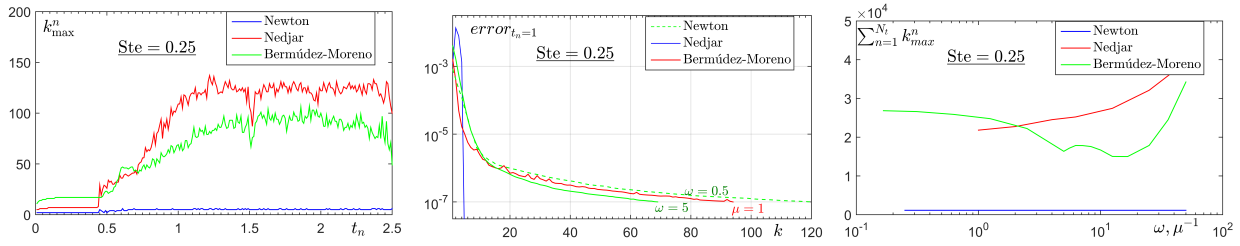

Figure 3.8: (Left:) Number of required iterations at each time level ($\mu = 1$ for the Nedjar algorithm an $\omega = 5$ for the Bermúdez–Moreno algorithm). (Middle:) Residual norm at each iteration for $t_n = 1$. (Right:) Total number of iterations as a function of μ and ω in the Nedjar and Bermúdez-Moreno algorithm, respectively.

Chapter 4

Navier-Stokes Equations to improve the Enthalpy Model

4.1 Introduction

To begin, we must mention that Chapter 4 of this thesis is partially based on the published book chapter by (Freire-Torres and Carpio 2023) and on the proceedings paper by (Freire-Torres and Carpio 2022)

In this chapter, we complete and improve the thermohydrodynamic model for the welding process, initially built, developed and optimized in Chapter 2 and verified its efficiency in Chapter 3. The improved model incorporates the equations of mass and momentum conservation (Navier-Stokes Equations) to better study the liquid zone within the molten metallic material. It also uses the Darcy model to study the mushy zone (where the liquid and solid zones coexist) as a porous medium, and the Boussinesq model to analyze the buoyancy terms, (Zhou and Tsai 2008; Piekarska and Kubiak 2011; Piekarska et al. 2011; Piekarska and Kubiak 2013). For the development of the numerical method, we will use the h-Newton solver, developed in Chapter 2 and verified its efficiency in comparison with other methods that have appeared in the literature, developed in Chapter 3.

4.2 Governing Equations

In this section, we present the equations that govern the welding phenomenon described above and shown schematically in Figure 4.1. Recall that there are three regions in the metal plate: solid, liquid, and mushy zone (where solid and liquid phases coexist). As basic hypotheses of the model, we assume:

- Constant density ρ at the three regions, as in (Rakotondrandisa et al. 2020).
- The intensity of convective currents in the liquid zone is significant; that is, the velocity $\mathbf{v}$ exists at each material point, which is why it is necessary to consider the mass and momentum equations (Navier-Stokes) for the movement of the fluid.

- The flow is Newtonian, laminar and incompressible.
- Iteractions between solid and liquid material are neglected.
- Radiation and evaporation are not considered in this study.
- Surface forces, e.g. shielding gas pressure or plasma pressure, are omitted in this work.
- The equations of elasticity—which take into account deformations and stresses in the material—and electromagnetism—which model the effect of the laser-arc heat source—are not considered in this study.
- The specific heat coefficient and the thermal conductivity depend on the state of the material but not on the temperature. Nevertheless, the present method can be easily extended to the more realistic case of temperature-dependent thermal coefficients.

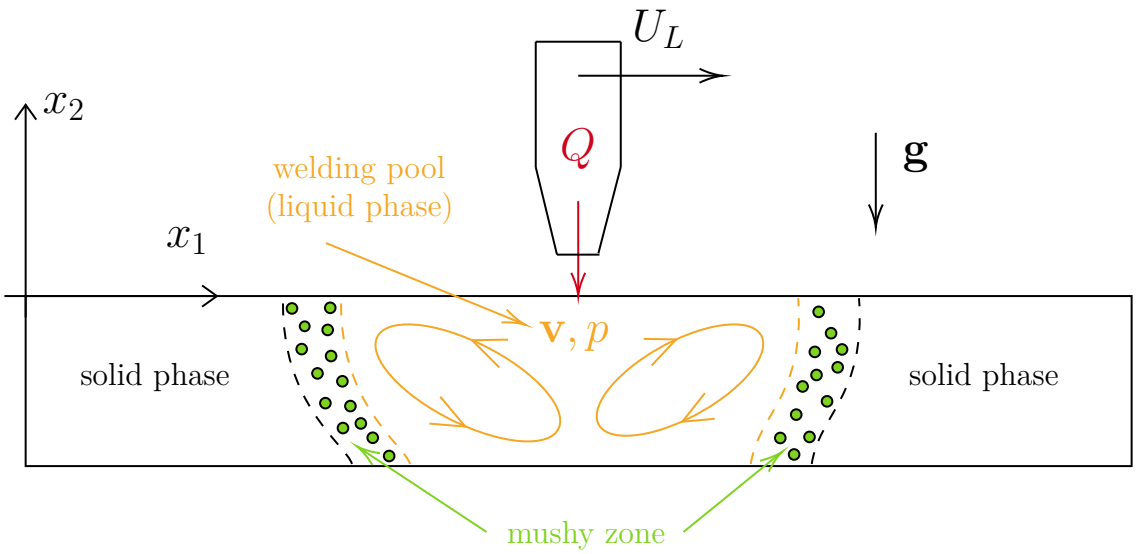

Figure 4.1: Simplified schematic of a welding problem, where we can see the three characteristic regions of the process, considering that there is a velocity field in the liquid phase, due to natural convection

4.2.1 Energy conservation equation

The energy conservation equation in terms of enthalpy is written in the form:

$$\frac{\partial(\rho h)}{\partial t} + \nabla \cdot (\rho h \mathbf{v}) = \nabla \cdot (\lambda \nabla T) + Q, \quad \text{in } \Omega, \tag{4.1}$$

where $\mathbf{v}$ is the velocity vector of each material point, λ is the thermal conductivity, and Q is a volumetric heat source due to a laser or electric power distribution. We assume in this work that λ is defined by parts, with constant value for solid λ_S $(T < T_F)$ and liquid λ_L $(T > T_F)$. On the other hand, we assume that the heat source Q is produced by a hybrid laser-arc source, which is able to internally heat the material due to the Joule effect (Piekarska and Kubiak

2011; Piekarska and Kubiak 2013). The initial condition corresponds to a fully solid state at ambient temperature $T = T_0$, and Dirichlet and Robin boundary conditions are defined on Γ_D and Γ_R, respectively (with $\partial\Omega = \Gamma_D \bigcup \Gamma_R$):

$$T = T_0 \ \text{ on } \Gamma_D, \qquad \text{and} \qquad -\lambda \frac{\partial T}{\partial \mathrm{n}} = \alpha(T - T_0) \ \text{ on } \Gamma_R, \tag{4.2}$$

where α is a convective coefficient and $\partial/\partial \mathrm{n}$ is the normal derivative.

The enthalpy depends on the temperature and on the liquid mass fraction, Y_L, in such a way that $\mathrm{d}h = c\,\mathrm{d}T + H_F\,\mathrm{d}Y_L$, where c is the specific heat capacity and H_F is the latent heat of fusion. For pure metals, melting takes place in welding processes at a constant temperature T_F. In the case of constant values for the latent heat of fusion, H_F, and for the specific heat coefficients at the solid and liquid regions, c_S and c_L, respectively, the relation between enthalpy and temperature is given by

$$h \in h(T) = \begin{cases} c_S(T - T_0), & T < T_F, \\ [h_S,\ h_L], & T = T_F, \\ h_L + c_L(T - T_F), & T > T_F, \end{cases} \tag{4.3}$$

with $h_S = c_S(T_F - T_0)$ and $h_L = h_S + H_F$ the enthalpies of the solid and liquid regions at the melting temperature T_F, respectively. Note the choice $h(T_0) = 0$. Above, the notation $h \in [h_S, h_L]$ means that h may take any value in this interval. That is, the function $h(T)$ is multi-valued at $T = T_F$, and, hence, the state of the metal is not univocally defined by the temperature. The definition of the enthalpy in (4.3) allows the temperature T and the mass fraction Y_L to be calculated as a single function of the enthalpy in a monotonically and univalued way, which constitutes a fundamental requirement for the numerical resolution of the equation.

$$Y_L = Y_L(h) := \begin{cases} 0, & h \le h_S, \\ (h - h_S)/H_F, & h_S < h < h_L, \\ 1, & h \ge h_L, \end{cases} \tag{4.4a}$$

$$T = T(h) := \begin{cases} T_0 + h/c_S, & h \le h_S, \\ T_F, & h_S < h < h_L, \\ T_F + (h - h_L)/c_L, & h \ge h_L, \end{cases} \tag{4.4b}$$

Furthermore, to facilitate the convergence of the h-Newton method, it is convenient to define the Kirchhoff's variable u, so that $\mathrm{d}u = \lambda(T)\mathrm{d}T$, which will be defined as:

$$u = u(T) := \begin{cases} \lambda_S(T - T_0), & T \le T_F, \\ \lambda_S(T_F - T_0) + \lambda_L(T - T_F), & T > T_F. \end{cases} \tag{4.5}$$

4.2.2 Mass and Momentum Conservation Equations

We begin by presenting the mass and momentum conservation equations for computing the velocity field of the liquid phase. We assume that the densities of the solid and liquid are equal and independent on temperature or the stress state of the solid.

For the momentum equation, we assume that the liquid is a Newtonian fluid with constant viscosity and retain the variation of density only in the buoyancy term according to the Boussinesq model in the melted zone. For fluid flow through porous media, we use the Darcy model.

Therefore, the mass and momentum conservation equations, with the aforementioned terms included, can be written as (Cho and Na 2009; Zhou and Tsai 2008; Piekarska and Kubiak 2011; Piekarska and Kubiak 2013):

$$\begin{cases} \nabla \cdot \mathbf{v} = 0, \\ \\ \rho \left(\dfrac{\partial \mathbf{v}}{\partial t} + \mathbf{v} \cdot \nabla \mathbf{v} \right) = -\nabla p + \mu \Delta \mathbf{v} - \rho \beta (T - T_F)\mathbf{g} - \dfrac{\mu}{\mathrm{K}} \mathbf{v}. \end{cases} \tag{4.6}$$

In the above system of equations 4.6, $\mathbf{v} = \{v_1, v_2, ..., v_d\}$ is the fluid velocity vector (where d=2,3 denotes the spatial dimension of the problem), $\mathbf{g}$ the gravity vector acceleration, p the hydrodynamic pressure, and T the temperature. Moreover, ρ is the constant density (for both liquid and solid), μ is the dynamic viscosity of fluid, β is the thermal expansion coefficient and T_F is the fusion temperature where the liquid phase starts to appear. Finally, K is the permeability of a porous medium that forms in the zone where the liquid and solid phases coexist at the melting temperature T_F (mushy zone). The permeability coefficient is modeled by the Carman-Kozeny law (Zhou and Tsai 2008), given by the equation.

$$\mathrm{K} = \mathrm{K}_0 \frac{{Y_L}^3}{(1 - Y_L)^2}, \quad \text{with} \quad \mathrm{K}_0 = \frac{{d_0}^2}{180}. \tag{4.7}$$

Here, we consider the mushy zone is composed of a regular matrix of spherical grains submerged into a liquid material, being Y_L the local mass fraction of liquid, K_0 the basic porous permeability and d_0 is the average diameter of the solid particle.

Equations (4.6) are valid in the whole domain, for the three zones which can appear in a welding problem (solid, liquid and mushy region). The solution in the solid phase $Y_L = 0$ is the trivial solution $\mathbf{v} = \mathbf{0}$ since $\mathrm{K} = 0$. For the pure liquid phase ($Y_L = 1$ and therefore $\mathrm{K} \to \infty$) we activate the Navier-Stokes equations. Finally, in the mushy zone, which is considered a porous media, due to the presence of liquid particles within a solid media, where the temperature is constant $T = T_F$, we have the Darcy equations.

The above equations must be completed with an initial condition at time $t = 0$, which will be homogeneous. Initially there will be only a solid phase with $\mathbf{v} = \mathbf{0}$. As boundary conditions, we will consider that the homogeneous conditions will be maintained over time, $\mathbf{v} = \mathbf{0}$ on $\partial\Omega$.

4.2.3 Non-Dimensional Formulation

To have a better understanding of the physical phenomenon, it is always convenient to formulate the problem in a non-dimensional form. In this way, we can evaluate the order of magnitude of each term in the equations and see which are the relevant (non-dimensional)

parameters that characterize the problem. The non-dimensional variables are denoted with the asterisk (*) symbol and defined as

$$\begin{cases} \mathbf{x}^* = \dfrac{\mathbf{x}}{L_0},\ \mathbf{v}^* = \dfrac{\mathbf{v}}{U_0},\ t^* = \dfrac{U_0}{L_0}t,\ p^* = \dfrac{p}{\rho U_0^2}, \\ \theta = \dfrac{T - T_0}{T_F - T_0},\ u^* = \dfrac{u}{\lambda_S(T_F - T_0)},\ h^* = \dfrac{h}{c_S(T_F - T_0)},\ Q^* = \dfrac{QL_0}{\rho c_S(T_F - T_0)U_0}, \end{cases} \tag{4.8}$$

where L_0 is a characteristic length (i.e. that of the longest boundary) and U_0 is a characteristic velocity (i.e. that of the moving source). With the definitions established in (4.8), the equations (4.1), (4.2), (4.4), (4.5), (4.6) and (4.7) are written in the following dimensionless form:

$$\frac{\partial h^*}{\partial t^*} + \nabla^* \cdot (\mathbf{v}^* h^*) = \frac{1}{\mathrm{Pe}}\Delta^* u^* + Q^* \qquad \text{in } \Omega, \tag{4.9}$$

$$\frac{\partial \mathbf{v}^*}{\partial t^*} + (\mathbf{v}^* \cdot \nabla^*)\mathbf{v}^* = -\nabla^* p^* + \frac{1}{\mathrm{Re}}\Delta^* \mathbf{v}^* + \frac{\mathrm{Gr}}{\mathrm{Re}^2}(\theta - 1)\mathbf{e_{x_2}} - \frac{1}{\mathrm{ReDa}}\frac{(1 - Y_L)^2}{Y_L^3}\mathbf{v}^* \qquad \text{in } \Omega, \tag{4.10}$$

$$\nabla^* \cdot \mathbf{v}^* = 0 \qquad \text{in } \Omega, \tag{4.11}$$

$$\theta\Big|_{t^*=0} = 0 \qquad \text{in } \Omega, \tag{4.12}$$

$$\mathbf{v}^*\Big|_{t^*=0} = \mathbf{0} \qquad \text{in } \Omega, \tag{4.13}$$

$$\theta = 0 \qquad \text{on } \Gamma_D, \tag{4.14}$$

$$\mathbf{v}^* = \mathbf{0} \qquad \text{on } \partial\Omega, \tag{4.15}$$

$$-\frac{\partial u^*}{\partial \mathrm{n}^*} = \mathrm{Nu}\ \theta \qquad \text{on } \Gamma_R, \tag{4.16}$$

where the Reynolds, Grashof, Darcy, Péclet and Nusselt numbers are defined as

$$\mathrm{Re} = \frac{\rho U_0 L_0}{\mu}, \quad \mathrm{Gr} = \frac{\rho^2 g\beta L_0^3(T_F - T_0)}{\mu^2}, \quad \mathrm{Da} = \frac{\mathrm{K}_0}{L_0^2}, \quad \mathrm{Pe} = \frac{\rho c_S L_0 U_0}{\lambda_S}, \quad \mathrm{Nu} = \frac{\alpha L_0}{\lambda_S}. \tag{4.17}$$

Two more dimensionless numbers have transcendental importance in thermal processes involving a change in phase: the Stefan number, Ste, defined as the ratio of the sensible heat.

$$\mathrm{Ste} = \frac{c_S(T_F - T_0)}{H_F}, \tag{4.18}$$

With the definitions above, the equations (4.4a), (4.4b) and (4.5), are rewritten as

$$Y_L = Y_L(h^*) := \begin{cases} 0, & h^* \leq 1, \\ \mathrm{Ste}\,(h^* - 1), & 1 < h^* < 1 + \dfrac{1}{\mathrm{Ste}}, \\ 1, & h^* \geq 1 + \dfrac{1}{\mathrm{Ste}}, \end{cases} \qquad \theta = \Theta(h^*) = \begin{cases} h^*, & h^* \leq 1 \\ 1, & 1 < h^* < 1 + \dfrac{1}{\mathrm{Ste}}, \\ \left(h^* - 1 - \dfrac{1}{\mathrm{Ste}}\right)\dfrac{c_S}{c_L} + 1, & h^* \geq 1 + \dfrac{1}{\mathrm{Ste}}, \end{cases} \tag{4.19a, 4.19b}$$

$$u^* = U(\theta) = \begin{cases} \theta, & \theta \leq 1, \\ \dfrac{\lambda_L}{\lambda_S}(\theta - 1) + 1, & \theta > 1. \end{cases} \tag{4.20}$$

4.3 Numerical Discretization of the Problem

Once the problem to be solved has been formulated mathematically, the steps to follow for numerical resolution will be indicated in this section of the document. We will use a conservative Lagrange-Galerkin formulation (Colera et al. 2020; Colera et al. 2021; Colera et al. 2022), within the spatial discretization framework of finite elements. To begin, we must introduce the weak formulation of the equations in partial derivatives to later move on to the discretization in time and space that will lead us to specific matrix problems.

4.3.1 Discretization and numerical resolution of the energy equation

We start by considering the energy equation (4.9), which we multiply by the test function φ and integrate in a moving domain $\widetilde{\Omega}$ with its respective Dirichlet boundary $\widetilde{\Gamma}_D$, and Robin boundary $\widetilde{\Gamma}_R$, to obtain the following integral-differential equation.

$$\frac{d}{dt}\int_{\widetilde{\Omega}} h\varphi dX + \frac{1}{\mathrm{Pe}}\int_{\widetilde{\Omega}} \nabla u \cdot \nabla\varphi dX + \frac{\mathrm{Nu}}{\mathrm{Pe}}\int_{\widetilde{\Gamma}_R} \theta\varphi dS = \int_{\widetilde{\Omega}} Q\varphi dX. \tag{4.21}$$

The $\widetilde{\Omega}$ domain of integration is a mobile domain that moves with the fluid particles inside it, so it is defined by the characteristic curves $\mathbf{X}(\mathbf{x}, t_n; t)$ of the convective operator of the problem and which is defined as.

$$\begin{cases} \dfrac{d\mathbf{X}(\mathbf{x}, t_n; t)}{dt} = \mathbf{v}(\mathbf{X}(\mathbf{x}, t_n; t)), \quad t \in [t, t_n] \\ \mathbf{X}(\mathbf{x}, t_n; t_n) = \mathbf{x}, \end{cases} \tag{4.22}$$

where $\mathbf{X}(\mathbf{x}, t_n; t)$ represents the position of the fluid particle for instants $t < t_n$ that at instant t_n will reach the point $\mathbf{x}$ of the Ω domain, as can be seen in figure 4.2. Therefore, the original domain corresponds to the instant of time t_n, being $\Omega \equiv \widetilde{\Omega}(t_n)$. Moreover, due to the boundary conditions that the velocity of the problem $\mathbf{v}|_{\partial\Omega} = \mathbf{0}$ must have, it follows that the domain will remain invariant $\Omega \equiv \widetilde{\Omega}(t)\ \forall t \leq t_n$. On the other hand, in the integro-differential

equation 4.21, the function φ vanishes at the Dirichlet boundary Γ_D and that $\mathrm{D}\varphi/\mathrm{D}t = 0$, that is, it remains constant along the characteristic curves $\mathbf{X}(\mathbf{x}, t_n; t)$.

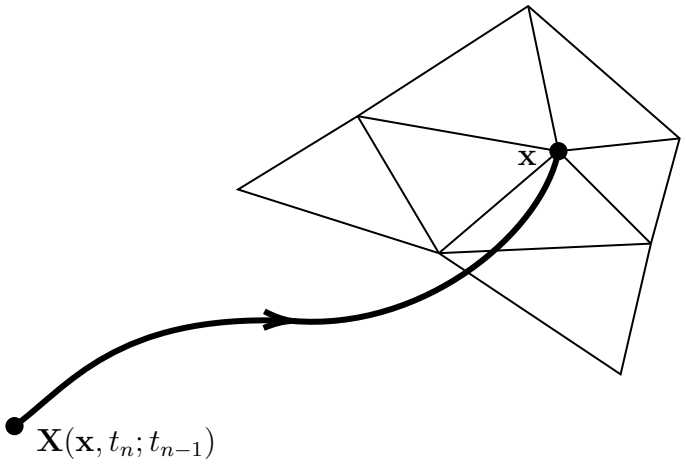

Figure 4.2: Schematic representation of the trajectory of the fluid particle that starts from $\mathbf{X}(\mathbf{x}, t_n; t_{n-1})$ to reach the point $\mathbf{x}$ at time t_n.

The next step is to discretize the equation (4.22) in time and then in space. As part of the temporal discretization, a second order BDF2 scheme (Backward Differentiation Formula Order 2) $\mathcal{O}(\Delta t^2)$ will be applied, obtaining the subsequent weak formulation of the problem. Once the variables for the previous instants t_{n-1} and t_{n-2}, we must find the unknown function $h(t_n) = h^n \in V_0$ that satisfies

$$\begin{cases} 3(h^n, \varphi)_\Omega + \dfrac{2\Delta t}{\mathrm{Pe}}(\nabla u^n, \nabla\varphi)_\Omega + \dfrac{2\Delta t \mathrm{Nu}}{\mathrm{Pe}}(\theta^n, \varphi)_{\Gamma_R} = \\ \\ = 2\Delta t(Q^n, \varphi)_\Omega + (4h^{n-1}(\mathbf{X}^{n-1}(\mathbf{x})) - h^{n-2}(\mathbf{X}^{n-2}(\mathbf{x})), \varphi)_\Omega, \quad \forall\varphi \in V_0, \end{cases} \tag{4.23}$$

where the standard dot product notation has been used to replace the integrals and compact notation has also been used to write the general expression $\mathbf{X}^{n-i}(\mathbf{x})$ as the foot of the curve characteristic at time t_{n-i}, $\mathbf{X}(\mathbf{x}) \equiv \mathbf{X}(\mathbf{x}, t_n; t_{n-i})$. These characteristic curves are calculated by a Runge-Kutta method of order 2 (whose order is consistent with the scheme used for the temporal discretization BDF2) using a linear extension of the velocity defined by the previous velocities $\mathbf{v}^{n-1}(\mathbf{x})$ and $\mathbf{v}^{n-2}(\mathbf{x})$. It is worth mentioning that the functional space V_0 has been introduced where both the solution to the problem and the test functions are contained:

$$V_0 = \{\phi \in H^1(\Omega) : \phi|_{\Gamma_D} = 0 \ \text{ and } \ \mathrm{D}\phi/\mathrm{D}t = 0\}. \tag{4.24}$$

Finally, to have a finite-dimensional problem, we must work with a discrete functional space V_h, associated with a triangulation or meshing of the Ω domain, denoted by $\mathbb{T}_h$. Quadratic piecewise polynomials construct the space V_h at each element $K \in \mathbb{T}_h$ of the triangulation. Now, we consider a basis $\{\varphi_i(\mathbf{x})\}_{i=1}^{N_n}$ of V_h, where each φ_i is the nodal basis function associated with node i of the mesh. Thus, we have to find the discrete unknown function h_h^n, θ_h^n, u_h^n, $Y_{Lh}^n \in V_h$ in such a way that satisfies the following:

$$h_h^n = \sum_{i=1}^{N^n} h_i^n \varphi_i(\mathbf{x}), \quad \theta_i^n = \theta(h_i^n), \quad Y_{Li}^n = Y_L(h_i^n), \quad u_i^n = u(\theta_i^n). \tag{4.25}$$

Equation (4.21) can be rewritten in matrix form to simplify the notation:

$$\begin{cases} 3\mathbf{M}\ \mathbf{h}^n + \dfrac{2\Delta t}{\mathrm{Pe}}\mathbf{K}\ \mathbf{u}^n + \dfrac{2\Delta t\mathrm{Nu}}{\mathrm{Pe}}\mathbf{M}_{\Gamma_R}\boldsymbol{\theta}^n = \mathbf{f}^n, \\ \theta_i^n = \theta(h_i^n) \quad \forall i = 1, 2, ..., N^n, \\ u_i^n = u(h_i^n) \quad \forall i = 1, 2, ..., N^n, \end{cases} \tag{4.26}$$

where the bold variables are vectors or matrices whose elements are defined by:

$$\begin{array}{l} M_{ij} = (\varphi_i, \varphi_j)_\Omega, \quad K_{ij} = (\nabla\varphi_i, \nabla\varphi_j)_\Omega, \quad M_{\Gamma_R ij} = (\varphi_i, \varphi_j)_{\Gamma_R} \\ f_i^n = (2\Delta t Q^n + 4h_h^{n-1}(\mathbf{X}^{n-1}(\mathbf{x})) - h_h^{n-2}(\mathbf{X}^{n-2}(\mathbf{x})), \varphi_i)_\Omega, \end{array} \tag{4.27}$$

and with $(\cdot\ ,\ \cdot)$ the standard scalar product in the L^2 norm. Note that, due to the introduction of Kirchhoff's variable (4.20), the stiffness matrix is constant (whenever the mesh remains fixed), which greatly simplifies the solution algorithm.

In order to solve the energy conservation equation, we use the h-Newton solver, developed in Chapter 2 to find the value of the enthalpy first, and then find the values of Kirchhoff's variable u and temperature θ.

With the definition of matrices (4.27), the Newton-type solving algorithm can be introduced, where the matrices and vectors of Newton's method are written as

$$\begin{array}{l} \mathbf{b}_k^n = 3\mathbf{M}\ \mathbf{h}_k^n + \dfrac{2\Delta t}{\mathrm{Pe}}\mathbf{K}\ \mathbf{u}_k^n + \dfrac{2\Delta t\mathrm{Nu}}{\mathrm{Pe}}\mathbf{M}_{\Gamma_R}\boldsymbol{\theta}_k^n - \mathbf{f}^n, \\ \mathbf{J}_k^n = 3\mathbf{M}\ \mathbf{D}_k^h + \dfrac{2\Delta t}{\mathrm{Pe}}\mathbf{K}\ \mathbf{D}_k^u + \dfrac{2\Delta t\mathrm{Nu}}{\mathrm{Pe}}\mathbf{M}_{\Gamma_R}\ \mathbf{D}_k^\theta, \end{array}$$

where $\theta_{k,i}^n = \theta(h_{k,i}^n)$, $u_{k,i}^n = u(h_{k,i}^n)$ are evaluated via (4.19) or (4.20); $\mathbf{D}_k^\phi$ (with ϕ denoting h, θ, or u) is the diagonal matrix:

$$D_{k,ij}^\phi = \left.\frac{d\phi}{dh}\right|_{h_{k,i}^n} \delta_{ij}, \tag{4.28}$$

where δ_{ij} is the Kronecker delta, and the derivatives $d\phi/dh$ are easily computed from expressions (4.19) and (4.20). Then, the value of $\mathbf{h}_{k+1}^n$ at the next iteration $k+1$ is given by solving

$$\mathbf{J}_k^n \boldsymbol{\Delta}\mathbf{h}_{k+1}^n = -\mathbf{b}_k^n, \quad \mathbf{h}_{k+1}^n = \mathbf{h}_k^n + \boldsymbol{\Delta}\mathbf{h}_{k+1}^n.$$

The iterations are stopped when the norm of $\boldsymbol{\Delta}\mathbf{h}_{k+1}^n$ is under a tolerance of 10^{-10}. The Jacobian has to be evaluated at each iteration. However, since the finite element matrices $\mathbf{M}$,

$\mathbf{K}$, $\mathbf{M}_{\Gamma_R}$ are constant, and only the diagonal matrices $\mathbf{D}_k^{\phi}$ need to be recomputed, this is not an expensive operation.

The matrices $\mathbf{D}_k^{\theta}$ and $\mathbf{D}_k^{u}$ defined by (4.28) can be readily calculated in the h-Newton algorithm as

$$D^{\theta}_{k,ij} = \left.\frac{d\theta}{dh}\right|_{h^n_{k,i}} \delta_{ij} = \left[\left.\frac{dh}{d\theta}\right|_{\theta^n_{k,i}}\right]^{-1} \delta_{ij}, \quad \text{and} \quad D^{u}_{k,ij} = \left.\frac{du}{dh}\right|_{h^n_{k,i}} \delta_{ij} = \left.\frac{du}{d\theta}\right|_{\theta^n_{k,i}} \left[\left.\frac{dh}{d\theta}\right|_{\theta^n_{k,i}}\right]^{-1} \delta_{ij}.$$

We note that, although there is no analytical expression, the function $\theta(h)$ is single-valued, and, therefore, $d\theta/dh|_{h^n_{k,i}} = \left[dh/d\theta|_{\theta^n_{k,i}}\right]^{-1}$ is finite.

4.3.2 Discretization and numerical resolution of the Navier-Stokes equations

The same formalism applied to the energy equation can be applied to the equations that determine fluid motion. Applying a Lagrange-Galerkin scheme, the nonlinear Navier-Stokes problem can be reduced to a linear Stokes problem, on which a temporal discretization scheme BDF2 is also applied. In this way, the resulting weak formulation implies finding for each t_n, the functions $\mathbf{v}^n \in (W_0)^2$ and $p^n \in L^2(\Omega)$, in such a way that it satisfies the following:

$$\begin{cases} 3(\mathbf{v}^n, \mathbf{w})_\Omega - 2\Delta t(p^n, \nabla\cdot\mathbf{w})_\Omega + \dfrac{2\Delta t}{\mathrm{Re}}(\nabla\mathbf{v}^n, \nabla\mathbf{w})_\Omega + \\ + \dfrac{2\Delta t}{\mathrm{ReDa}}\left(\dfrac{(1-Y_L^n)^2}{(Y_L^n)^3}\mathbf{v}^n, \mathbf{w}\right)_\Omega = (4\mathbf{v}^{n-1}(\mathbf{X}^{n-1}(\mathbf{x})) - \mathbf{v}^{n-2}(\mathbf{X}^{n-2}(\mathbf{x})), \mathbf{w})_\Omega + \\ + \dfrac{2\Delta t\mathrm{Gr}}{\mathrm{Re}^2}((\theta^n - 1)\mathbf{e}_{x_2}, \mathbf{w})_\Omega, \quad \forall \mathbf{w} \in (W_0)^2, \\ \\ (\nabla\cdot\mathbf{v}^n, q)_\Omega = 0, \quad \forall q \in L^2(\Omega), \end{cases} \tag{4.29}$$

where the functional space $W_0 = \{\phi \in H^1(\Omega) : \phi|_{\partial\Omega} = 0\}$ is defined in such a way that it takes into account the homogeneous boundary conditions for the velocity. From the resolution of the energy conservation equation, exposed previously, at known times t_n, the thermodynamic properties h^n (and jointly $\theta^n = \theta(h^n)$ and $Y_L^n = Y_L(h^n)$) are calculated, so the only unknowns of 4.29 are the velocity $\mathbf{v}^n$ and the pressure p^n. For the spatial discretization, finite elements of the Taylor-Hood $\mathbb{P}_2/\mathbb{P}_1$, will be used, quadratic for the velocity and linear for the pressure to satisfy the condition of Ladyzhenskaya-Babuska-Brezzi. Finally, the linear system of matrices generated by spatial discretization will be solved with a conjugate gradient algorithm with an Uzawa-type preconditioner (Glowinski and Pironneau 1979; Waters et al. 2004; Shu et al. 2020).

4.3.3 Mesh Refinement

To conclude with the section dedicated to the discretization and numerical resolution of the equations, we provide a brief description of the local anisotropic mesh refinement technique

employed here; the reader is referred to (Carpio and Prieto 2014; Carpio et al. 2016; Carpio et al. 2019; Freire-Torres and Carpio 2023) for more details. With this technique, we define at each time level t^n a mesh triangulation $\mathbb{T}_h^n$ so that the solution is computed within a given accuracy employing the minimum possible number of degrees of freedom (mesh nodes).

As shown in Figure (4.3), an anisotropic element K can be defined by the semiaxes lengths $\lambda_{1,K} \geq \lambda_{2,K}$ of the circumscribed ellipse E, and by the corresponding orthogonal directions $\mathbf{r}_{1,K}$ and $\mathbf{r}_{2,K}$. The element size is $|K| = 3\sqrt{3}/4\ \lambda_{1,K}\lambda_{2,K}$, and the aspect ratio is defined as $s_K = \lambda_{1,K}/\lambda_{2,K}$. In order to employ an automatic mesh generator, we must define a metric tensor $\mathbf{M}_K$ such that

$$\mathbf{M}_K = \left(\frac{|\widehat{K}|}{|K|}\right) \mathbf{R}_K \mathbf{S}_K^{-1} \mathbf{R}_K^T, \tag{4.30}$$

with $\mathbf{R}_K = \{\mathbf{r}_{1,K},\ \mathbf{r}_{2,K}\}$, $\mathbf{S}_K = \text{diag}\,\{s_K,\ 1/s_k\}$ and $|\widehat{K}|$ the size of the generated element when $\mathbf{M}_K$ is the unity tensor. The latter parameter depends on the specific mesh generator; in this work, we employ BAMG (Hecht 2006), for which $|\widehat{K}| = \sqrt{3}/4$.

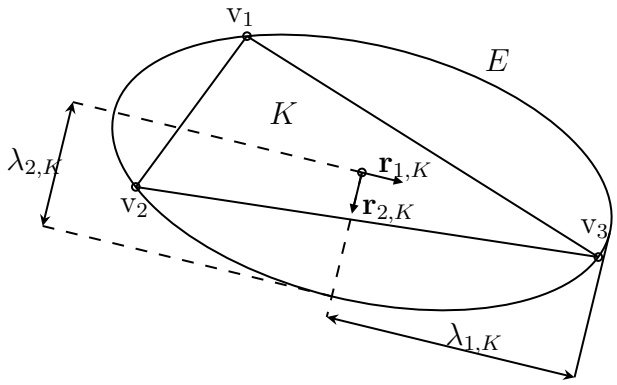

Figure 4.3: Fundamental parameters of an anisotropic element K.

The optimal orientation $\mathbf{R}_K^*$ and shape $\mathbf{S}_K^*$ of the element K can be computed from the Hessian matrix $\mathbf{H}_K$ of the solution h_h^n. More specifically, if $g_{i,K}$ are the eigenvalues (with $|g_{1,K}| < |g_{2,K}|$) and $\mathbf{l}_{i,K}$ are the corresponding eigenvectors, we obtain:

$$s_K^* = \left(|g_{2,K}|/|g_{1,K}|\right)^{1/2}, \quad \mathbf{r}_{i,K}^* = \mathbf{l}_{i,K}, \quad \text{for } i = 1,\ 2. \tag{4.31}$$

Finally the optimal size $|K^*|$ for each element K is computed so as to minimize the number of mesh elements under a condition of the form $\eta^n = \left(\sum_K (\eta_K^n)^2\right)^{1/2} \leq \text{Tol}$, where η_K is an estimation of the error on K. In particular,

$$\eta_K^n = \left(\int_K \left[h^n - \Pi_{h1} h^n\right]^2\ d\text{x}\right)^{1/2}, \tag{4.32}$$

with $\Pi_{h1} h^n$ being the continuous, piecewise linear interpolation of h^n at the mesh vertices,

and

$$|K^*| = |K| \left(\frac{\mathrm{Tol}^2}{\sum_{K \in \mathbb{T}_h^n} (\eta_K^n)^{1/2}} \right)^{1/3} (\eta_K^n)^{-1/2}. \tag{4.33}$$

The variables $|K^*|$, $\mathbf{R}_K^*$, and $\mathbf{S}_K^*$ define a metric tensor $\mathbf{M}^*$ via Equation (4.30), which is sent to BAMG (Hecht 2006) to generate a new mesh $\mathbb{T}_h^{n*}$.

Hence, at each time level t^n, we have a solution computed on $\mathbb{T}_h^n$ with an estimated error η^n and a new (more optimal) mesh $\mathbb{T}_h^{n*}$. If $\eta^n > \mathrm{Tol}$, we set $\mathbb{T}_h^n = \mathbb{T}_h^{n*}$ and recompute the solution at t^n. Otherwise, we accept the solution at time t_n and set $\mathbb{T}_h^{n+1} = \mathbb{T}_h^{n*}$. In practice, if the time step size is moderate, the solution computed at t^n is seldom rejected, and thus the CPU time does not increase substantially with the present local mesh adaptation algorithm.

It is not strictly necessary to adapt the mesh at each iteration. Indeed, some authors prefer to keep the mesh fixed until the time step is rejected because the space error is higher than the tolerance. However, we prefer to update the mesh at each time level in order to have a better tracking of the borders of the phase-change region. Furthermore, the number of rejected time steps is smaller if the mesh is updated at each time level.

4.4 Numerical tests

To finish this chapter, and to observe the optimal behavior of the designed numerical method, a numerical example is presented in a rectangular domain $\Omega = [0, 2.5] \times [-1, 0]$, with boundary $\partial\Omega \equiv \Gamma_1 \cup \Gamma_2 \cup \Gamma_3 \cup \Gamma_4$ as can be seen in figure 5.2, We will consider as boundary conditions: null velocity $\mathbf{v} = \mathbf{0}$ in all frontiers, and for the energy equation we will consider the Dirichlet type frontier $\Gamma_D \equiv \Gamma_1 \cup \Gamma_2 \cup \Gamma_4$ where the temperature will be set to the ambient $\theta = 0$ ($h = 0$ & $Y_L = 0$), and the Robin type boundary $\Gamma_R \equiv \Gamma_3$ where a loss of heat by convection to the environment will be considered. The numerical integration will take place between $0 \leq t \leq 5.0$, with a homogeneous initial condition $h = 0$ and $\mathbf{v} = \mathbf{0}$.

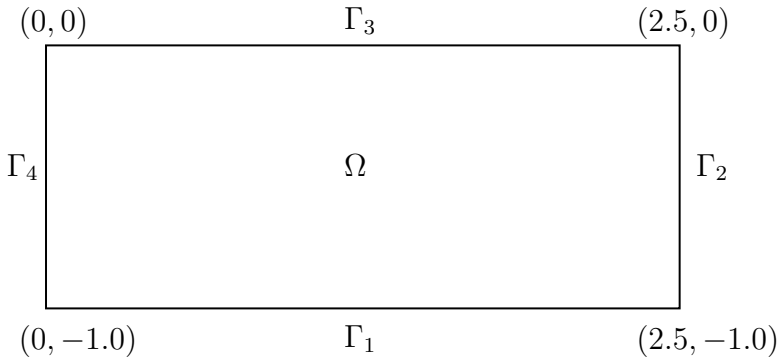

Figure 4.4: Domain and boundaries associated to the welding problem to resolve.

The heat source Q, defined at all points in the domain, will be a Gaussian-type distribution that will move from left to right of the domain at a constant velocity. Furthermore, to obtain

more valuable information on the physical process under study, we will consider that the heat source only acts up to the instant $t = 1.0$, analyzing the behavior of the system from then until the final time $t = 5.0$.

$$Q(x_1, x_2, t) = \begin{cases} Q_0 \exp\left(-50(x_1 - (x_{1_0} + v_{x_1 0} t))^2 - 10(x_2 - x_{2_0})^2\right)(1 - e^{-5t}), & 0 \leq t \leq 1.0, \\ 0, & 1.0 < t \leq 5.0, \end{cases} \tag{4.34}$$

with $Q_0 = 25.0$, $v_{x_1 0} = 1.5$, $x_{1_0} = 0.5$ and $x_{2_0} = -0.5$.

Finally, to completely define the problem, it is necessary to specify the set of dimensionless numbers that intervene in the mathematical model; for this purpose, the magnitudes with dimensions used in some literature (Piekarska and Kubiak 2011; Piekarska and Kubiak 2013) have been selected as a reference for their calculation. We note that the numbers Gr and Ste obtained are more conservative in these studies and that we have considered a higher number of Gr so that the fluid motion has more influence on temperature transport and a smaller number of Ste so that the non-linear effect has more relevance. The set of dimensionless parameters to be considered are the following:

$$\mathrm{Re} = 200, \quad \mathrm{Gr} = 10^6, \quad \mathrm{Da} = 10^{-4}, \quad \mathrm{Pe} = 40, \quad \mathrm{Nu} = 10. \tag{4.35}$$

Regarding the computational aspects, all the tests were carried out on an i7-8700 CPU computer with 16GB DDR3 RAM @1.3 GHz with the Ubuntu 20.02.4 LTS operating system, using the C programming language for its development.

4.4.1 Test I: $\mathrm{Ste} \to \infty, c_S/c_L = 1.0, \lambda_S/\lambda_L = 1.0$

To begin with this test, we perform a test where the Stefan number tends towards infinity and the ratios of specific heats and thermal conductivities are equal to one. This choice of parameters ensures a single-valued enthalpy, simplifying the problem to a linear one. By setting the non-dimensional variables equal according to equations (4.19b) and (4.20), finally we obtain ($u = \theta = h$), eliminating the multivalued nature of the enthalpy, we use the values $\mathrm{Tol} = 1 \times 10^{-3}$, $\mathrm{h_{max}} = 0.100$ and $\Delta t = 0.01$.

In Figures 4.5 and 4.6, we can see a graphical representation of the solution at some chosen time. The isolines that mark the border between the solid and liquid zone are represented in the inner part of the figures, together with the current blue lines that indicate where the fluid movement exists.

In the upper panel, a cut is represented by the line $x_2 = -0.5$ of the selected domain to observe the profiles of the problem's thermodynamic variables and the vertical component of the velocity field v_{x_2}.

According to the Figure 4.5 due to the infinite value of the Stefan number, there is no mushy region; on the other hand, the enthalpy h and temperature θ are equal along the time due to the constant value of the non-dimensional thermal coefficient equal to one.

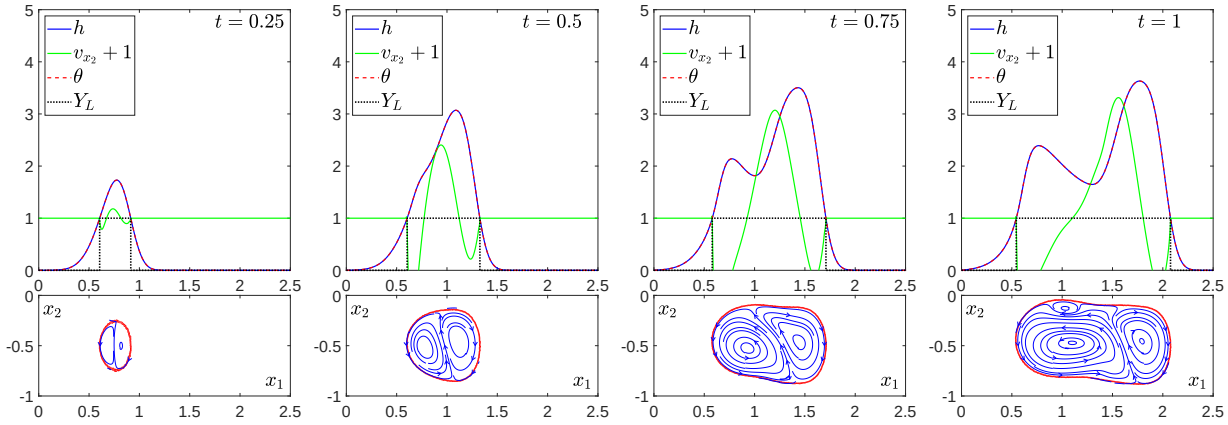

Figure 4.5: Solutions obtained in the first times $t \leq 1.0$ in which the external heat source Q is acting, for Test I.

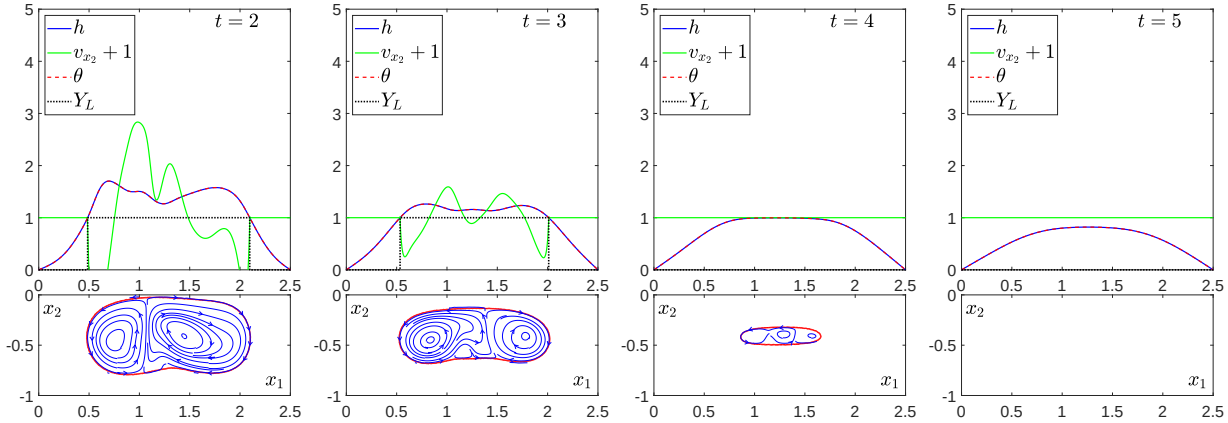

Figure 4.6: Solutions obtained in the final times $t > 1.0$ in which the external heat source Q is off, for Test I.

In the time interval of $[0; 1.0]$, we can observe the growth of the enthalpy h, the temperature θ, liquid fraction Y_L and the vertical component of the velocity field v_{x_2}, as the external heat source Q moves along the time, here we can see clearly differentiate only two phases, the liquid phase and the solid phase, without giving way to the development of the mushy zone, this is also confirmed by the value of the liquid fraction, which is either $Y_L = 0.0$ or $Y_L = 1.0$. On the other hand, in figure 4.6, with the abrupt cessation from external heat source Q, we can observe that the thermodynamic variables h, θ, v_{x_2} and Y_L decrease along the time interval $(1.0, 5.0]$, to such an extent that at time $t \sim 5.0$, the vertical component of the velocity field v_{x_2} disappears completely.

In the Figure 4.7; we can observe the anisotropic meshing for Test I, according to the parameters described in subsection about mesh adaptation; with the following variables to consider to proceed to the adaptation: tolerance equal to 8×10^{-2}, mesh size varies between $(0.010, 0.100)$, and time step equal 0.01; in this case in particular, given the anisotropic nature of the mesh fitting, the emergence and growth of a considerable number of elements in the region define the boundaries clearly between of the solid and liquid phases.

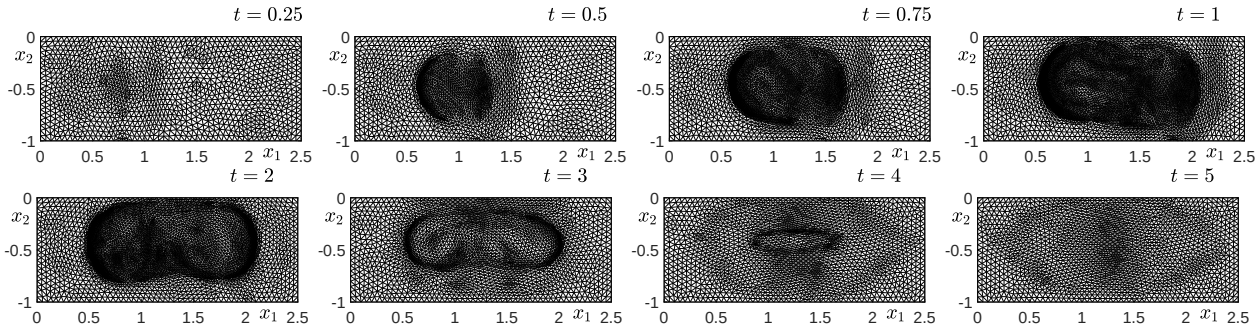

Figure 4.7: Evolution of the anisotropic meshing of Test I along the time with Tol $= 8 \times 10^{-2}$, $\mathrm{h_{max}} = 0.100$ and $\Delta t = 0.01$.

4.4.2 Test II: Ste $\to \infty, c_S/c_L = 0.75, \lambda_S/\lambda_L = 1.50$

As in Test I, we consider that the Stefan number also tends to infinity, with the difference that the ratios of the specific heats and thermal conductivities between are not equal to one, that implies that Test II is transformed into a non-linear problem. We use the values Tol $= 1 \times 10^{-3}$, $\mathrm{h_{max}} = 0.100$ and $\Delta t = 0.01$.

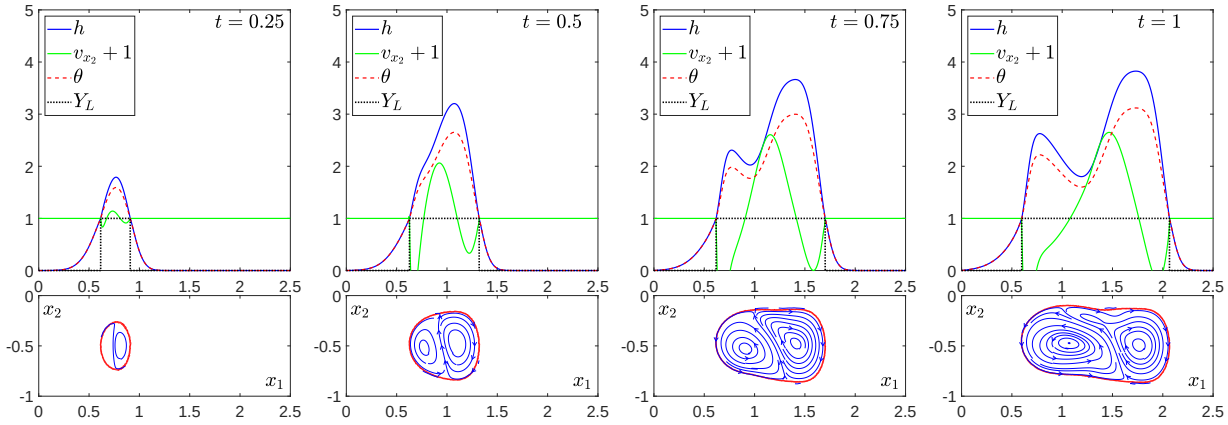

Figure 4.8: Solutions obtained in the first times $t \leq 1.0$ in which the external heat source Q is acting, for Test II.

In Figures 4.8 and 4.9, as in the Test I, the infinite value of the Stefan number implies that the mushy zone also does not exist; the main difference with the previous test is that the value of the non-dimensional thermodynamical variables u and θ depends on the enthalpy h value. It should also be noted as in Test I, the selection of the Stefan number tending to infinity causes only two phases to develop over time, the liquid and solid phases. On the other hand, in this test, unlike the previous one, there is a difference in the value of the enthalpy and the temperature increase in the time interval of $[0, 1.0]$, and decreases in the interval $(1.0, 5.0]$, at different rates; this effect is caused by the selection of different ratios of specific heats c_S/c_L and thermal conductivities λ_S/λ_L. In addition, it is worth mentioning that to end at time $t \sim 5.0$, practically the entire domain is in solid phase.

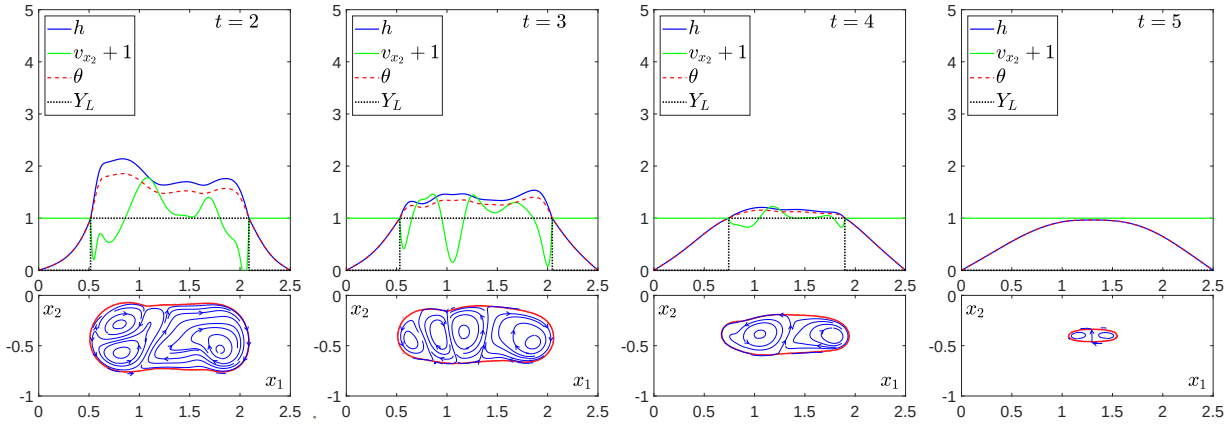

Figure 4.9: Solutions obtained in the final times $t > 1.0$ in which the external heat source Q is off, for Test II.

4.4.3 **Test III:** Ste $= 10.0, c_S/c_L = 0.75, \lambda_S/\lambda_L = 1.50$

In this test, we consider a finite value for the Stefan number. In Figure 4.10 and 4.11, we can see that the enthalpy h, temperature θ, liquid fraction Y_L and vertical component of the velocity field v_{x_2} profiles, are similar to those presented in the Test II, the main difference lies in the formation of the narrow mushy zone due to the finiteness of the Stefan number, specifically, equal to Ste $= 10.0$, we use the values Tol $= 1 \times 10^{-3}$, $\mathrm{h_{max}} = 0.100$ and $\Delta t = 0.01$. In this narrow mushy zone, we have that the liquid fraction Y_L, varies not only between 0 or 1, but also between its intermediate values.

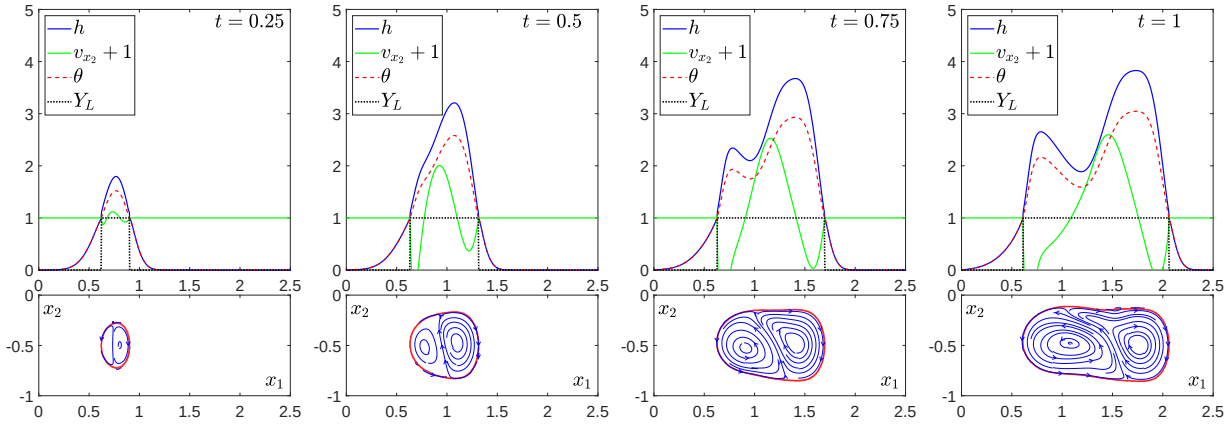

Figure 4.10: Solutions obtained in the first times $t \leq 1.0$ in which the external heat source Q is acting, for Test III.

In Figure 4.12, we can observe an amplification (in green) of the domain at the instant of time $t \sim 0.75$, at which, the appearance of the three zones clearly defined by the theory can be highlighted: the mushy zone M surrounded by the borders in red, liquid and solid $(0.0 < Y_L < 1.0)$; in turn, to its left, the pure liquid zone L containing the blue current lines $(Y_L = 1.0)$, and to its right, the pure solid zone S, $(Y_L = 0.0)$.

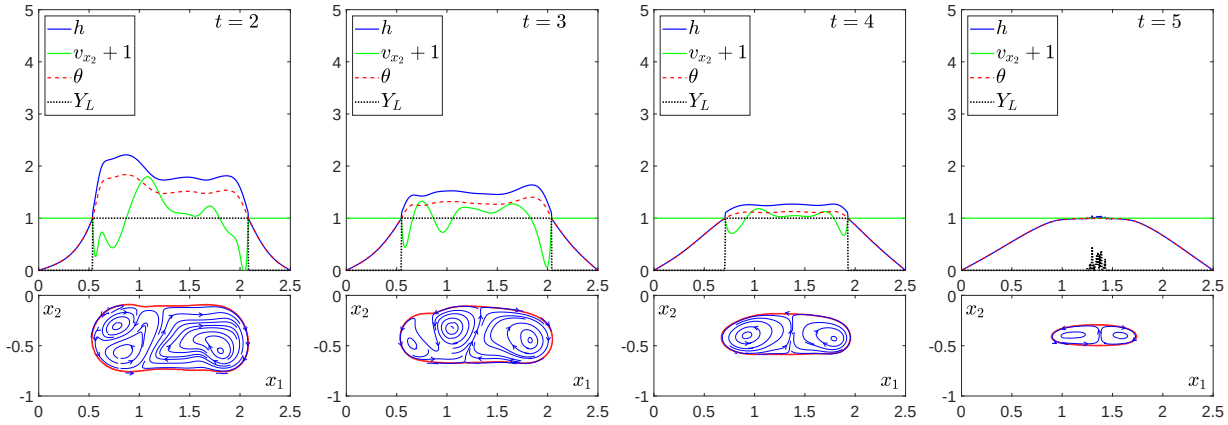

Figure 4.11: Solutions obtained in the final times $t > 1.0$ in which the external heat source Q is off, for Test III.

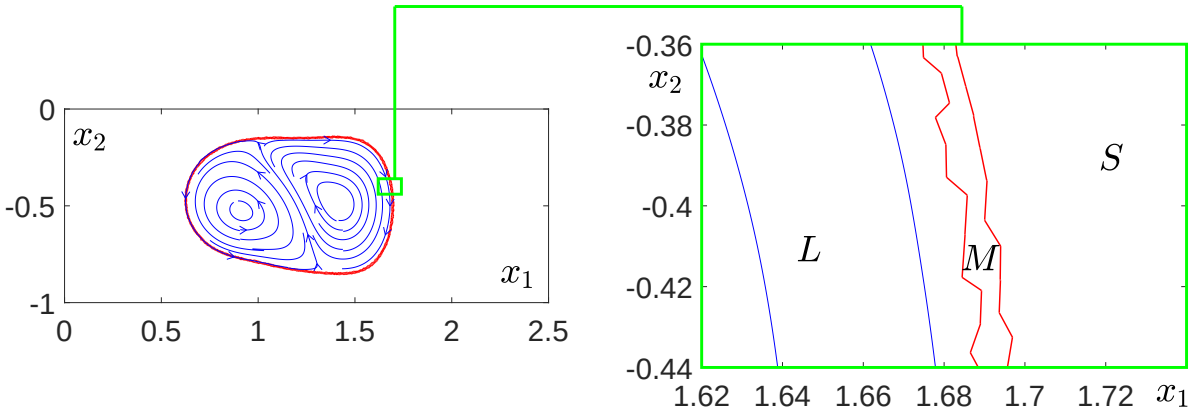

Figure 4.12: Amplification of the phases existing of the Test III at $t = 0.75$ in the domain when the development of the velocity field $\mathbf{v}$. We can see three main regions: L is the liquid zone, S is the solid zone and M is the mushy zone.

4.4.4 **Test IV:** Ste $= 1.0, c_S/c_L = 0.75, \lambda_S/\lambda_L = 1.50$

This test is similar to Test III, since with the presence of a finite Stefan number, this will give way to the formation of the three previously mentioned zones, it is worth mentioning that this mushy zone moves and is not stable along the time, it tends to disappear, according to the theory described in Stefan's problem (Barbu 2021; Pegler and Wykes 2021; Son and Park 2021; Nedjar 2002). We use the values Tol $= 1 \times 10^{-3}$, $\mathrm{h_{max}} = 0.100$ and $\Delta t = 0.01$.

Due to the existence of a finite Stefan number, according to equation (4.19a), the mushy zone appears again, but the difference is that this zone is wider because the value of the Stefan number is smaller Ste $= 1.0$, as can be clearly seen in Figure 4.13, when the domain reaches the times $t \sim 0.5$, $t \sim 0.75$ and $t \sim 1.0$.

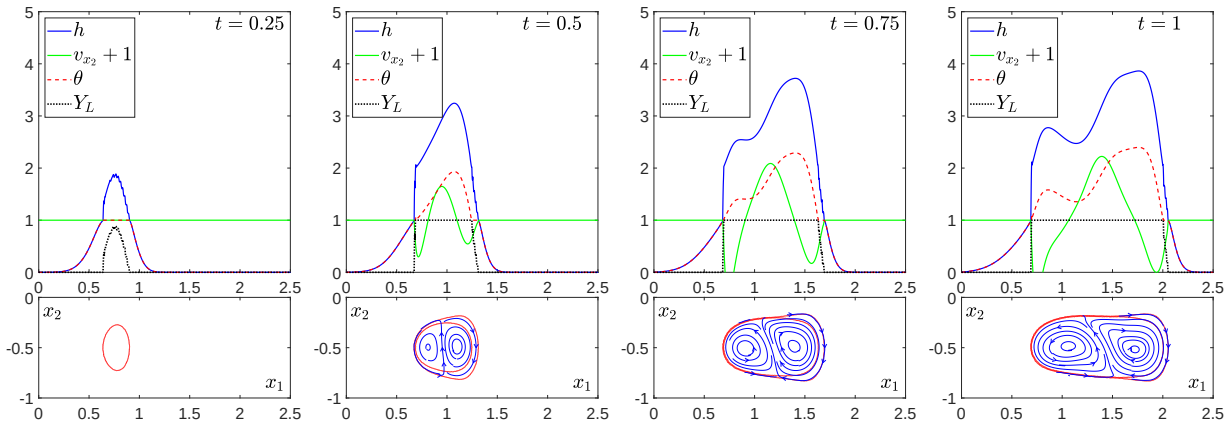

Figure 4.13: Solutions obtained in the first times $t \leq 1.0$ in which the external heat source Q is acting, for Test IV.

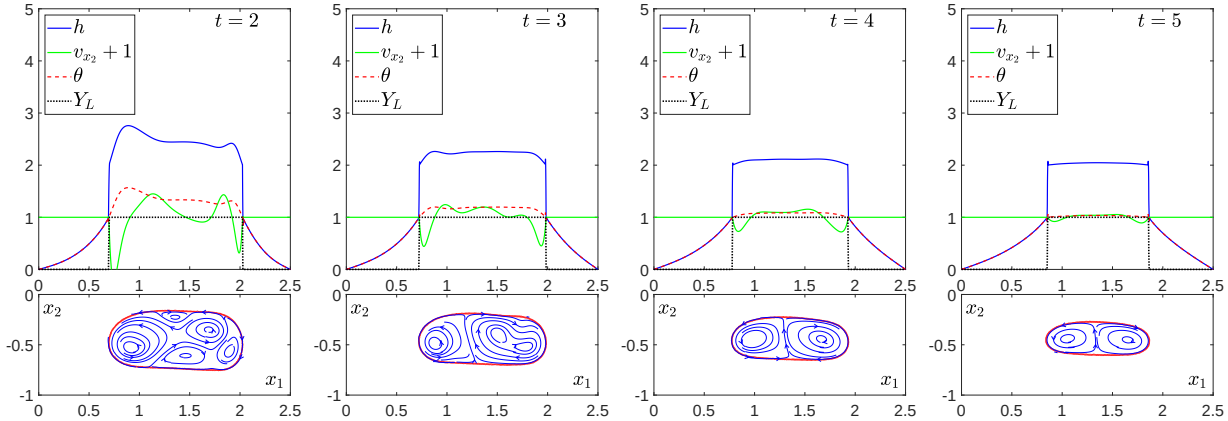

Figure 4.14: Solutions obtained in the final times $t > 1.0$ in which the external heat source Q is off, for Test IV.

4.4.5 Test V: $\mathrm{Ste} = 0.5, c_S/c_L = 0.75, \lambda_S/\lambda_L = 1.50$

The last test, given that the Stefan number $\mathrm{Ste} = 0.5$, this value causes the maximum expansion of the mushy zone, also, presents the greatest complication to find the solutions, for this purpose, the developed algorithms present the greatest number of internal iterations to solve the problem. We use the values $\mathrm{Tol} = 1 \times 10^{-3}$, $\mathrm{h_{max}} = 0.100$ and $\Delta t = 0.01$.

In Figure 4.15 represents the first instants of time where the external heat source Q is acting with $t \leq 1$. It can be seen that from $t \sim 0.25$, the heat supplied has managed to heat the solid until it reaches the melting temperature $\theta = 1$ in points of the domain, and the phase mixture zone begins to appear (mushy zone). The source in its movement continues to add heat, and at $t \sim 0.5$, the first zone of a pure liquid is observed at temperatures higher than those of fusion. From this moment on, the buoyancy terms cease to be null, and fluid movement begins. The presence of the 3 phases (solid, liquid, and mushy) is observed for longer times. In the front zone (where the external heat source is arriving), the fusion of the solid takes place, and it presents relatively smooth gradients in the enthalpy variable h. However, in the

rear part (from where the external heat source moves away), the resolidification of the formed liquid takes place, and very pronounced fronts are formed in the h variable around the lines that mark the mixing zone, and that causes the area where the phases coexist to be reduced.

Once the external heat source Q is turned off, the phenomenon of cooling and temperature homogenization begins, which can be seen in Figure 4.16. In a few moments, the area where the phase mixture exists begins to shrink drastically as a result of the resolidification of the material. This disappearance of the mixing zone can also be seen very well on the sides and in the upper area, where the fluid movement is slower. However, the lower zone is where the mixing zone is maintained until the last moments. As time progresses, the mixing zone completely disappears, leaving only the liquid phase and the solid phase, separated by a zone of discontinuity, which gradually reduces in size due to the heat that the zone loses. Nevertheless, the heat only flows at the edges because inside, where the liquid is, there is no heat conduction. After all, the area is already at the melting temperature $\theta = 1$.

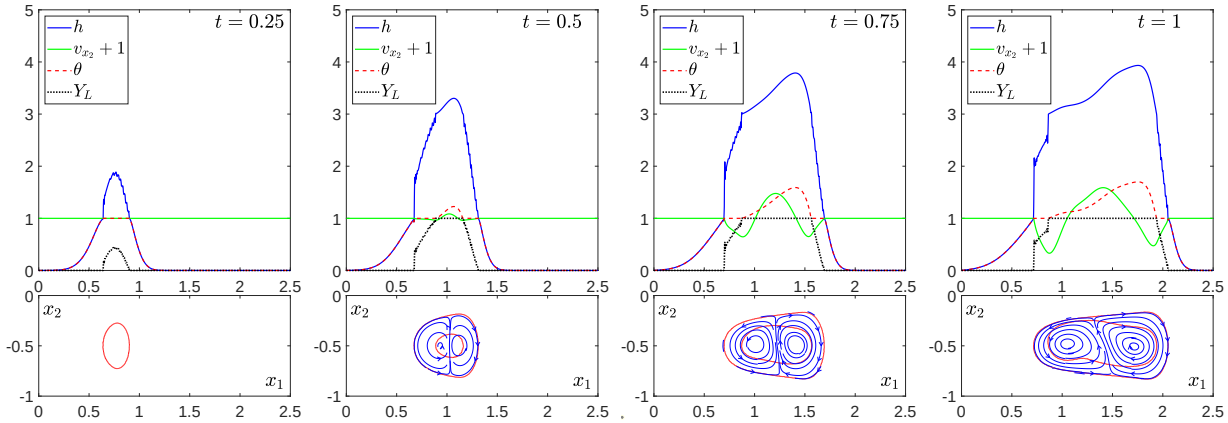

Figure 4.15: Solutions obtained in the first times $t \leq 1.0$ in which the external heat source Q is acting, for Test V.

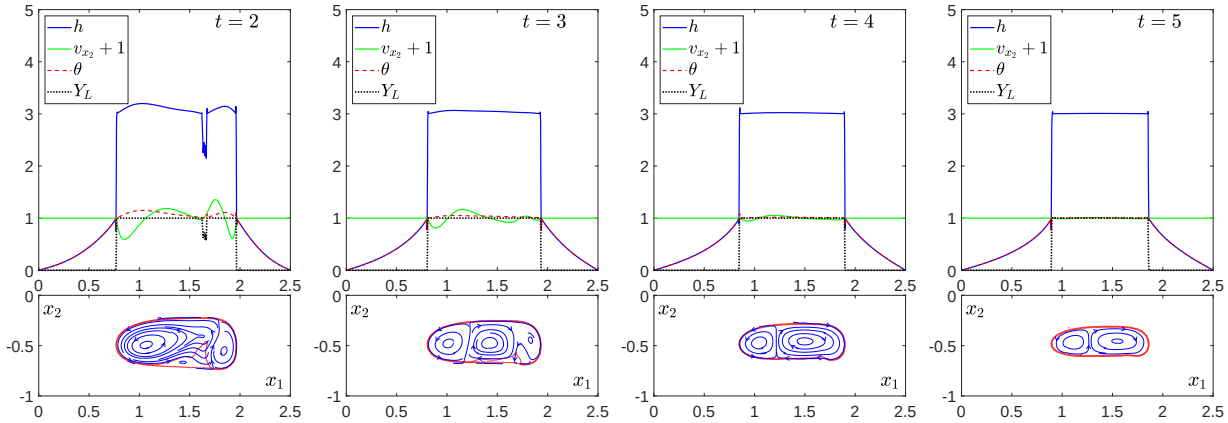

Figure 4.16: Solutions obtained in the final times $t > 1.0$ in which the external heat source Q is off, for Test V.

Chapter 5

The Enthalpy Model applied to Heat Treatment

5.1 Introduction

This chapter is in charge of applying the model developed in Chapters 2 and 4 of the present research to heat treatment problems. In other words, this chapter deals with the thermomechanical model and the numerical simulation of metallurgical phase transitions of steel during industrial heat treatment.

Steel is a metallic alloy of iron and carbon in which the carbon content ranges up to 2 percent (with a higher carbon content, the material is defined as cast iron). By far the most widely used material for building the world's infrastructure and industries, it is used to fabricate a great variety of products from sewing needles to oil tankers. In addition, the tools required to build and manufacture such articles usually made of steel. As an indication of the relative importance of this material, in 2013 the world's raw steel production was about 1.6 billion tons, while production of the next most important engineering metal, aluminum, was about 47 million tons. The main reasons for the popularity of steel are the relatively low cost of making, forming, and processing it, the abundance of its two raw materials (iron ore and scrap), and its unparalleled range of mechanical properties (Encyclopaedia Britannica 2023c).

Throughout the millennia of steelmaking knowledge, one of the most renowned applications of steel has been in legendary Asian swords, prized for both their strength and toughness. This well-deserved fame is largely due to the exceptional hardness achieved through a meticulous process of heating and cooling steel. However, hardness also implies fragility. To mitigate this, only one edge of the sword is typically hardened, while the other edge and the core retain ductility and impact resistance. This differential hardening results in a blade that is both incredibly sharp and resilient, capable of delivering both cutting and piercing blows without shattering. The confluence of resistance and hardness has elevated steel to the pinnacle of industrial and engineering materials for the past few centuries. Its unrivaled combination of properties makes it indispensable for a vast array of applications, from construction and manufacturing to transportation and energy production. The ability to manipulate

these properties through heat treatment is of paramount importance in the development of innovative products. By carefully controlling the heating and cooling cycles, steel can be tailored to meet the specific demands of a wide range of applications. This allows for the creation of materials that are not only strong and durable, but also cost-effective and readily available. As a result, heat treatment plays a vital role in enabling the large-scale production of high-quality steel products. Steel is a metal alloy that is basically composed of iron and, to a lesser extent, carbon, as well as other alloying elements. Industrial-type steel must contain between 0.2 and 2.1 percent carbon by weight within the composition. Together with other alloying elements such as chromium, molybdenum, and vanadium, carbon represents the main source of hardness that this alloy can obtain. It is necessary to control the amount of carbon present in the steel, since it will provide a perfect balance between hardness, toughness, ductility, and tensile strength (Díaz Moreno et al. 2021).

5.2 Governing Equations

In this section, we present the equations that govern the heat treatment. Recall that there are three regions in the metal plate: solid, liquid, and mushy zone (where solid and liquid phases coexist). As basic hypotheses of the model, we assume:

- Constant density ρ at the three regions, as in (Rakotondrandisa et al. 2020).
- The intensity of convective currents in the liquid zone is not significant; that is, the velocity $\mathbf{v} \sim \mathbf{0}$ at each material point, i.e. we consider problems at low Grashof number limit $\mathrm{Gr} \to 0$, so there is no motion caused by the buoyancy forces. Otherwise, mass and momentum equations for the fluid motion are not considered in this chapter.
- The flow is Newtonian, laminar and incompressible.
- Iteractions between solid and liquid material are neglected.
- Radiation and evaporation are not considered in this study.
- Surface forces, e.g. shielding gas pressure or plasma pressure, are omitted in this work.
- The equations of elasticity—which take into account deformations and stresses in the material—and electromagnetism—which model the effect of the laser-arc heat source—are not considered in this study.
- The specific heat coefficient and the thermal conductivity depend on the state of the material but not on the temperature. Nevertheless, the present method can be easily extended to the more realistic case of temperature-dependent thermal coefficients.
- The heat source Q applied in the heating stage comes mainly from two principal sources: Electrinal Resistance Heating and Electromagnetic Induction Heating.

5.2.1 Energy conservation equation

The energy conservation equation in terms of enthalpy is written in the form:

$$\frac{\partial(\rho h)}{\partial t} = \nabla \cdot (\lambda \nabla T) + Q, \qquad \text{in } \Omega, \tag{5.1}$$

where ρ is the density (which we assume to be constant and equal for both liquid and solid phases), h is the enthalpy per mass unit, λ is the thermal conductivity, and Q is a volumetric heat source due to a laser or electric power distribution. We assume in this work that λ is defined by parts, with constant value for solid λ_S ($T < T_F$) and liquid λ_L ($T > T_F$). On the other hand, we assume that the heat source Q is produced by a hybrid laser-arc source, which is able to internally heat the material due to the Joule effect (Piekarska and Kubiak 2011; Piekarska and Kubiak 2013). The initial condition corresponds to a fully solid state at ambient temperature $T = T_0$, and Dirichlet and Robin boundary conditions are defined on Γ_D and Γ_R, respectively (with $\partial\Omega = \Gamma_D \bigcup \Gamma_R$):

$$T = T_0 \ \text{ on } \Gamma_D, \qquad \text{and} \qquad -\lambda \frac{\partial T}{\partial \mathrm{n}} = \alpha(T - T_0) \ \text{ on } \Gamma_R, \tag{5.2}$$

where α is a convective coefficient and $\partial/\partial \mathrm{n}$ is the normal derivative.

The enthalpy depends on the temperature and on the liquid mass fraction, Y_L, in such a way that $\mathrm{d}h = c\,\mathrm{d}T + H_F\,\mathrm{d}Y_L$, where c is the specific heat capacity and H_F is the latent heat of fusion. For pure metals, melting takes place in welding processes at a constant temperature T_F. In the case of constant values for the latent heat of fusion, H_F, and for the specific heat coefficients at the solid and liquid regions, c_S and c_L, respectively, the relation between enthalpy and temperature is given by

$$h \in h(T) = \begin{cases} c_S(T - T_0), & T < T_F, \\ [h_S,\ h_L], & T = T_F, \\ h_L + c_L(T - T_F), & T > T_F, \end{cases} \tag{5.3}$$

with $h_S = c_S(T_F - T_0)$ and $h_L = h_S + H_F$ the enthalpies of the solid and liquid regions at the melting temperature T_F, respectively. Note the choice $h(T_0) = 0$. Above, the notation $h \in [h_S, h_L]$ means that h may take any value in this interval. That is, the function $h(T)$ is multi-valued at $T = T_F$, and, hence, the state of the metal is not univocally defined by the temperature. The definition of the enthalpy in (5.3) allows the temperature T and the mass fraction Y_L to be calculated as a single function of the enthalpy in a monotonically and univalued way, which is fundamental for the numerical resolution of the equation.

$$Y_L = Y_L(h) := \begin{cases} 0, & h \le h_S, \\ (h - h_S)/H_F, & h_S < h < h_L, \\ 1, & h \ge h_L, \end{cases} \tag{5.4a}$$

$$T = T(h) := \begin{cases} T_0 + h/c_S, & h \le h_S, \\ T_F, & h_S < h < h_L, \\ T_F + (h - h_L)/c_L, & h \ge h_L. \end{cases} \tag{5.4b}$$

Furthermore, to facilitate the convergence of the h-Newton method, it is convenient to define the Kirchhoff's variable u, so that $\mathrm{d}u = \lambda(T)\mathrm{d}T$, which will be defined as:

$$u = u(T) := \begin{cases} \lambda_S(T - T_0), & T \leq T_F, \\ \lambda_S(T_F - T_0) + \lambda_L(T - T_F), & T > T_F. \end{cases} \tag{5.5}$$

5.2.2 Phase Transformations Equations

The Johnson-Mehl-Avrami-Kolmogorov equations describe how solids can transform from one phase to another at constant temperature, being more specific, these describe the crystallization kinetics (Avrami 1939; Avrami 1940; Avrami 1941), generally these expressions are used in the study of phase change of certain materials, chemical reaction rates and even within studies in ecological systems (Avramov 2007). The so-called phase diagram, which shows the steel-phase that corresponds to a given temperature and mass fraction of carbon, is shown in Figure 5.1. The following expression describes the transformation of austenite (a) into ferrite (f), pearlite (p) and bainite (b),

$$\vartheta = 1 - \exp\left(-\mathcal{K}_\vartheta t^{\mathrm{n}_\vartheta}\right), \tag{5.6}$$

where $\vartheta = \{\mathrm{f}, \mathrm{p}, \mathrm{b}\}$ is the transformed steel-phase volume fraction. According to the literature in (Umemoto et al. 1982; Campbell et al. 1991; Fuhrmann et al. 1999; Pereloma and Edmonds 2012; Bhadeshia 2017; Barmak 2018; Wu et al. 2021), the value of the exponent n depends on the type of nucleation, and $\mathcal{K}$ is influenced by the phase transformation mechanism, isothermal temperature and the shape of the isothermal transformation curve. The relationship that exists between the variables $\mathcal{K}$ and T can be modeled according to a Gaussian function (Murugaiyan et al. 2006; Donnay et al. 1996; Wu et al. 2021), as shown in the equation

$$\mathcal{K}_\vartheta(T) = \mathcal{K}_{0\vartheta} \exp\left[-\left(\frac{T - T_{\mathrm{m}\vartheta}}{\mathrm{c}}\right)^{\mathrm{d}}\right], \tag{5.7}$$

where, $T_{m\vartheta}$ is a mean temperature of steel-phase ϑ, that corresponding to the temperature which is obtained from isothermal transformation curves TTT, c is the standard mean square error and d is a constant related to the curvature of the curve.

5.2.2.1 Austenite transformation

Austenite is a solid solution of carbon and other constituents in a particular form of iron known as γ (gamma) iron. This is a face-centred cubic structure formed when iron is heated above 910° C (1,670° F); gamma iron becomes unstable at temperatures above 1,390° C (2,530° F). Austenite is an ingredient of a kind of stainless steel used for making cutlery, hospital and food-service equipment, and tableware, (Mouritz 2012; Encyclopaedia Britannica 2023d). In equation (5.8), a Leblond-Devaux model (Leblond and Devaux 1984; Montalvo-Urquizo et al. 2013; Díaz et al. 2012; Díaz Moreno et al. 2021) is considered to simulate the appear of the austenite transformation a, the rate of change is modeled as:

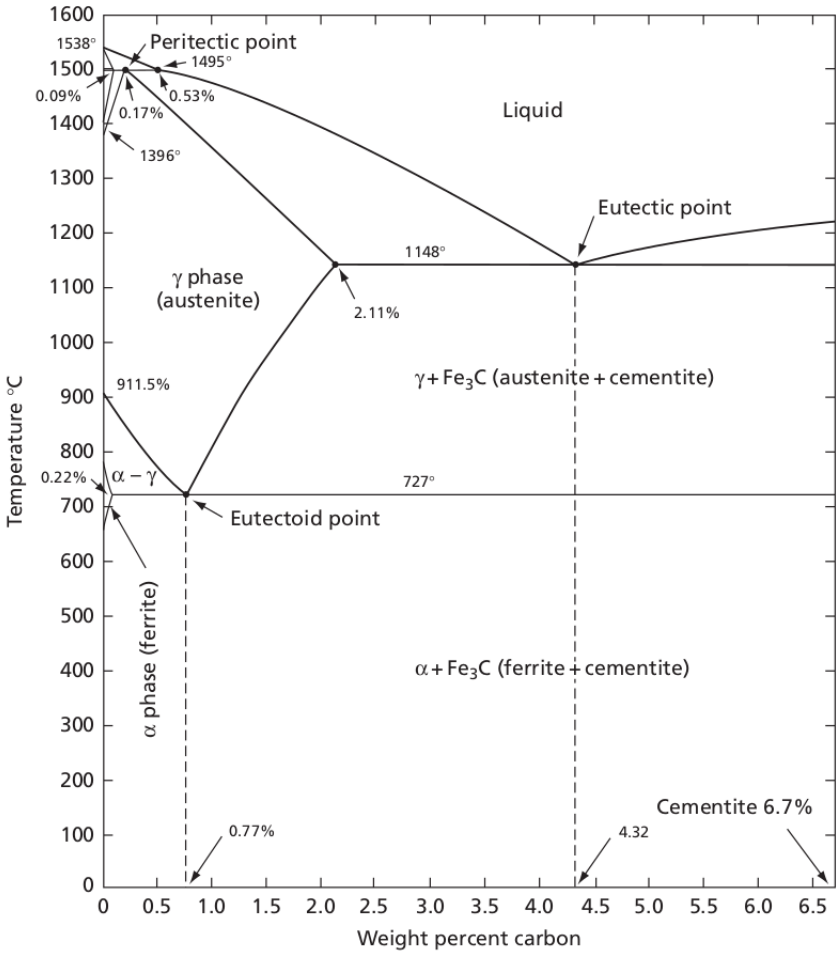

Figure 5.1: Iron-carbide phase diagram

$$\begin{cases} \dfrac{da}{dt} = \dfrac{a_{eq}(T) - a}{\tau_a(T)} \mathscr{H}(T - T_{sa}), & \text{in } \Omega, \\ \\ a(x, 0) = 0, & \text{in } \Omega, \end{cases} \tag{5.8}$$

where, $a_{eq}(T)$ is a stationary solution at constant temperature with a time constant equal to $\tau_a(T)$, $\mathscr{H}$ is the Heaviside function, T_{sa} is an austenite starting temperature. T_{aa} is an austenite auxiliar temperature. T_{fa} is an austenite finishing temperature. The $a_{eq}(T)$ and $\tau_a(T)$ relations are functions of an experimental nature that have been obtained and are expressed in the literature (Díaz et al. 2012; Díaz Moreno et al. 2021). The analytical solution of (5.8) is

$$a(x, t) = a_{eq}(T) \left[1 - \exp\left(-\frac{t}{\tau_a(T)} \right) \right] \mathscr{H}(T - T_{sa}) \tag{5.9}$$

$$a_{eq}(T) = \begin{cases} 0, & T < T_{sa}, \\ \dfrac{T - T_{sa}}{T_{fa} - T_{sa}}, & T_{sa} \leq T \leq T_{fa}, \\ 1, & T > T_{fa}, \end{cases} \tag{5.10a}$$

$$\tau_a(T) = \begin{cases} 1, & T < T_{sa}, \\ 1 - \dfrac{0.8(T - T_{sa})}{T_{aa} - T_{sa}}, & T_{sa} \leq T < T_{aa}, \\ 0.2 - \dfrac{0.15(T - T_{aa})}{T_{fa} - T_{aa}}, & T_{aa} \leq T < T_{fa}, \\ 0.05, & T \geq T_{fa}. \end{cases} \tag{5.10b}$$

5.2.2.2 Ferrite-Pearlite-Bainite transformation

Ferrite is a body-centered cubic (BCC) crystal structure of iron. It is the most common phase in steel, and it is responsible for the magnetic properties of steel. Ferrite is also relatively soft and ductile, making it easy to form and fabricate. The amount of ferrite in steel depends on the carbon content and the cooling rate. Steels with low carbon content (less than 0.25%) are mostly ferritic. As the carbon content increases, the amount of ferrite decreases. Steels with high carbon content (greater than 0.75%) are mostly pearlitic, which is a mixture of ferrite and cementite (iron carbide). Ferrite is formed when austenite (a high-temperature phase of iron) transforms to ferrite upon cooling. The transformation temperature depends on the carbon content and the alloying elements in the steel. In low-carbon steels, the transformation temperature is around 910 °C (1670 °F). The cooling rate also affects the amount and morphology of ferrite in steel. Slow cooling promotes the formation of large ferrite grains, while fast cooling promotes the formation of small ferrite grains (Abbaschian and Reed-Hill 2009).

Pearlite is the product of the decomposition of austenite by a eutectoid reaction (a eutectoid reaction is a metallurgical process that occurs in binary alloys with a certain concentration of the alloys. It is similar to the eutectic reaction but instead of being a liquid, what is transformed is a solid), and comprises a lamellar arrangement of ferrite and cementite. The pearlite reaction provides an excellent example of the historical development of physical metallurgy and the importance of the interaction of experimental observations and the development of quantitative models (Embury 2012).

Bainite, named for E. C. Bain (Davenport and Bain 1970) is the generic term for fine aggregates of ferrite α platelets (or laths) separated by regions of residual phases, untransformed austenite γ, or cementite θ. The transformation occurs from austenite γ at temperatures between those at which pearlite and martensite form. The aggregates of plates that share common crystallographic orientations are designated as *sheaves*, whereas individual plates are also called subunits (Garcia-Mateo and Caballero 2014).

The values of k and n in the Johnson-Mehl-Avrami-Kolmogorov (JMAK) equations (5.6) and (5.7) for ferrite phase in steels vary depending on a number of factors, including the carbon content, alloying elements, and cooling rate. However, in general, the value of exponents F is typically between 1 and 3 for the ferrite phase in steels. This indicates that the ferrite transformation is a nucleation and growth process. The value of $\mathcal{K}$ is the rate constant for

the transformation, and it is typically higher for steels with higher carbon content and faster cooling rates.

5.2.2.3 Martensite transformation

Martensite, the hardening constituent in quenched steels, is formed at temperatures below about 200 °C The regions of the austenite which have transformed to martensite are lenticular in shape and may easily be recognized by etching, or from the distortion they produce on the polished surface of the alloy. The lenticular shape of a martensite needle is a direct consequence of the stresses produced in the surrounding matrix by the shear mechanism of the transformation and is exactly analogous to the similar effect found in mechanical twinning.

The strain energy associated with martensite is tolerated because the growth of such sheared regions does not depend on diffusion, and since the regions are coherent with the matrix they are able to spread at great speed through the crystal. The large free energy change associated with the rapid formation of the new phase outweighs the strain energy, so that there is a net lowering of free energy (Smallman and Bishop 1999).

Fraction of martensite is obtained below T_{sm} temperature, which expression is calculated from Koistinen-Marburger formula (Koistinen and Marburger 1959).

$$\mathrm{m}(x,t) = 1 - \exp\left(\frac{T_{\mathrm{sm}} - T}{\varphi}\right), \tag{5.11}$$

where m is the fraction of martensite, T_{sm} is the martensite starting temperature and φ is an experimental constant.

5.2.3 Non-Dimensional Formulation

To have a better understanding of the physical phenomenon, it is always convenient to formulate the problem in a non-dimensional form. In this way, we can evaluate the order of magnitude of each term in the equations and see which are the relevant (non-dimensional) parameters that characterize the problem. The non-dimensional variables are denoted with the asterisk (*) symbol and defined as

$$\begin{cases} \mathbf{x}^* = \dfrac{\mathbf{x}}{L_0},\ t^* = \dfrac{U_0}{L_0}t,\ \mathcal{K}_\vartheta^* = \dfrac{\mathcal{K}_\vartheta}{\mathcal{K}_{0\vartheta}}, \\ \theta = \dfrac{T - T_0}{T_F - T_0},\ u^* = \dfrac{u}{\lambda_S(T_F - T_0)},\ h^* = \dfrac{h}{c_S(T_F - T_0)},\ Q^* = \dfrac{QL_0}{\rho c_S(T_F - T_0)U_0}, \end{cases} \tag{5.12}$$

where L_0 is a characteristic length (i.e. that of the longest boundary) and U_0 is a characteristic velocity (i.e. that of the moving source). With the definitions established in (5.12), the equations (5.1), (5.2), (5.4), (5.5), (5.6), (5.8), (5.10a), (5.10b) and (5.11) are written in the following dimensionless form:

5.2.3.1 Heating stage

In this heating stage, the enthalpy h and therefore the temperature θ of the steel plate is raised due to the heat source Q, starting from an initial time $t_0 = 0$ until a final heating time t_H, in this stage, the austenite–a phase is developed. The equations involved in this stage are the following

$$\frac{\partial h^*}{\partial t^*} = \frac{1}{\mathrm{Pe}}\Delta^* u^* + Q^* \qquad \text{in } \Omega \times [t_0, t_H), \tag{5.13}$$

$$\frac{d\mathrm{a}^*}{dt^*} = \frac{\mathrm{a}^*_{\mathrm{eq}} - \mathrm{a}^*}{\tau^*_{\mathrm{a}}}\mathscr{H}(\theta - \theta_{\mathrm{sa}}) \qquad \text{in } \Omega \times [t_0, t_H), \tag{5.14}$$

$$\theta\Big|_{t^*=0} = 0 \qquad \text{in } \Omega, \tag{5.15}$$

$$\mathrm{a}^*\Big|_{t^*=0} = 0 \qquad \text{in } \Omega, \tag{5.16}$$

$$\theta = 0 \qquad \text{on } \Gamma_D \times [t_0, t_H), \tag{5.17}$$

$$-\frac{\partial u^*}{\partial \mathrm{n}^*} = \mathrm{Nu}\ \theta \qquad \text{on } \Gamma_R \times [t_0, t_H). \tag{5.18}$$

5.2.3.2 Cooling stage

In the cooling stage, the austenite created during the heating stage is transformed step by step into the other steel-phases, e.g. ferrite, pearlite, bainite and martensite, it is important to mention that this stage begins immediately after the end of the heating stage, that is, it begins at time t_H and ends at time t_f. The equations involved in this stage are the following

$$\frac{\partial h^*}{\partial t^*} = \frac{1}{\mathrm{Pe}}\Delta^* u^* + Q^* \qquad \text{in } \Omega \times [t_H, t_f), \tag{5.19}$$

$$\frac{d\mathrm{a}^*}{dt^*} = \frac{\mathrm{a}^*_{\mathrm{eq}} - \mathrm{a}^*}{\tau^*_{\mathrm{a}}}\mathscr{H}(\theta - \theta_{\mathrm{sa}}) \qquad \text{in } \Omega \times [t_H, t_f), \tag{5.20}$$

$$\mathrm{f}^* = 1 - \exp\left(-\mathrm{F}\mathcal{K}^*_{\mathrm{f}} t^{*\mathrm{n_f}}\right) \qquad \text{in } \Omega \times [t_H, t_f), \tag{5.21}$$

$$\mathrm{p}^* = 1 - \exp\left(-\mathrm{P}\mathcal{K}^*_{\mathrm{p}} t^{*\mathrm{n_p}}\right) \qquad \text{in } \Omega \times [t_H, t_f), \tag{5.22}$$

$$\mathrm{b}^* = 1 - \exp\left(-\mathrm{B}\mathcal{K}^*_{\mathrm{b}} t^{*\mathrm{n_b}}\right) \qquad \text{in } \Omega \times [t_H, t_f), \tag{5.23}$$

$$\mathrm{m}^* = 1 - \exp\left[\mathrm{M}(\theta_{\mathrm{sm}} - \theta)\right], \qquad \text{in } \Omega \times [t_H, t_f), \tag{5.24}$$

$$\theta\Big|_{t^*=t_H} = \theta_H \qquad \text{in } \Omega, \tag{5.25}$$

$$\mathrm{a}\Big|_{t^*=t_H} = \mathrm{a}_H \qquad \text{in } \Omega, \tag{5.26}$$

$$\theta = 0 \qquad \text{on } \Gamma_D \times [t_H, t_f), \tag{5.27}$$

$$-\frac{\partial u^*}{\partial \mathrm{n}^*} = \mathrm{Nu}\ \theta \qquad \text{on } \Gamma_R \times [t_H, t_f), \tag{5.28}$$

where the Péclet and Nusselt numbers are defined as

$$\mathrm{Pe} = \frac{\rho c_S L_0 U_0}{\lambda_S}, \qquad \mathrm{Nu} = \frac{\alpha L_0}{\lambda_S}, \tag{5.29}$$

and the constants directly related to the steel-phases

$$\mathrm{F} = \frac{\mathcal{K}_{0\mathrm{f}} L^{\mathrm{n_f}}}{U_0^{\mathrm{n_f}}}, \qquad \mathrm{P} = \frac{\mathcal{K}_{0\mathrm{p}} L^{\mathrm{n_p}}}{U_0^{\mathrm{n_p}}}, \qquad \mathrm{B} = \frac{\mathcal{K}_{0\mathrm{b}} L^{\mathrm{n_b}}}{U_0^{\mathrm{n_b}}}, \qquad \mathrm{M} = \frac{T_F - T_0}{\varphi}. \tag{5.30}$$

Two more dimensionless numbers have transcendental importance in thermal processes involving a change in phase: the Stefan number, Ste, defined as the ratio of the sensible heat.

$$\mathrm{Ste} = \frac{c_S (T_F - T_0)}{H_F}, \tag{5.31}$$

With the definitions above, the equations (5.4a), (5.4b) and (5.5), are rewritten as

$$Y_L = Y_L(h^*) := \begin{cases} 0, & h^* \leq 1, \\ \mathrm{Ste}\,(h^* - 1), & 1 < h^* < 1 + \dfrac{1}{\mathrm{Ste}}, \\ 1, & h^* \geq 1 + \dfrac{1}{\mathrm{Ste}}, \end{cases} \tag{5.32a}$$

$$\theta = \Theta(h^*) = \begin{cases} h^*, & h^* \leq 1 \\ 1, & 1 < h^* < 1 + \dfrac{1}{\mathrm{Ste}}, \\ \left(h^* - 1 - \dfrac{1}{\mathrm{Ste}}\right) \dfrac{c_S}{c_L} + 1, & h^* \geq 1 + \dfrac{1}{\mathrm{Ste}}, \end{cases} \tag{5.32b}$$

$$u^* = U(\theta) = \begin{cases} \theta, & \theta \leq 1, \\ \dfrac{\lambda_L}{\lambda_S}(\theta - 1) + 1, & \theta > 1. \end{cases} \tag{5.33}$$

On the other hand, the equations (5.7), (5.9) (5.10), are also rewritten in a dimensionless form,

$$\mathcal{K}^*_\vartheta = \exp\left[-\kappa_\vartheta (\theta - \theta_{\mathrm{m}\vartheta})^{\mathrm{d}_\vartheta}\right], \quad \text{with} \quad \kappa_\vartheta = \left(\frac{T_F - T_0}{\mathrm{c}_\vartheta}\right)^{\mathrm{d}_\vartheta} \tag{5.34}$$

$$\mathrm{a} = \mathrm{a_{eq}}(\theta) \left[1 - \exp\left(-\frac{t^*}{\tau_{\mathrm{a}}(\theta)}\right)\right] \mathscr{H}(\theta - \theta_{\mathrm{sa}}) \tag{5.35}$$

$$\mathrm{a_{eq}}(\theta) = \begin{cases} 0, & \theta < \theta_{\mathrm{sa}}, \\ \dfrac{\theta - \theta_{\mathrm{sa}}}{\theta_{\mathrm{fa}} - \theta_{\mathrm{sa}}}, & \theta_{\mathrm{sa}} \leq \theta \leq \theta_{\mathrm{fa}}, \\ 1, & \theta > \theta_{\mathrm{fa}}, \end{cases} \tag{5.36a}$$

$$\tau_{\mathrm{a}}(\theta) = \begin{cases} 1, & \theta < \theta_{\mathrm{sa}}, \\ 1 - \dfrac{0.8(\theta - \theta_{\mathrm{sa}})}{\theta_{\mathrm{aa}} - \theta_{\mathrm{sa}}}, & \theta_{\mathrm{sa}} \leq \theta < \theta_{\mathrm{aa}}, \\ 0.2 - \dfrac{0.15(\theta - \theta_{\mathrm{aa}})}{\theta_{\mathrm{fa}} - \theta_{\mathrm{aa}}}, & \theta_{\mathrm{aa}} \leq \theta < \theta_{\mathrm{fa}}, \\ 0.05, & \theta \geq \theta_{\mathrm{fa}}. \end{cases} \tag{5.36b}$$

5.3 Numerical results

In this section, we show the results of several numerical experiments to address the performance of the present method. All tests were carried out on an i7-8700 CPU computer with 16GB DDR3 RAM @1.3 GHz under Ubuntu 20.02.4 LTS operating system, and the codes were written in C programming language. In addition, an anisotropic mesh adaptation was used, as detailed in (Carpio and Prieto 2014; Carpio et al. 2016; Carpio et al. 2019; Freire-Torres et al. 2023).

5.3.1 Test I: Fixed Gaussian-Type Heat Source

To carry out Tests I and II, we evaluate the h-Newton method for solving the energy equation, we present an example defined by the rectangular domain $\Omega = [0, 2.5] \times [-1, 0]$, with boundary $\partial\Omega \equiv \Gamma_1 \cup \Gamma_2 \cup \Gamma_3 \cup \Gamma_4$, as can be seen in Figure (5.2). We consider an initial condition $\theta = 0$, Dirichlet boundary conditions on $\Gamma_D \equiv \Gamma_1 \cup \Gamma_2 \cup \Gamma_4$, where the temperature is set to the ambient one, and a Robin condition on $\Gamma_R \equiv \Gamma_3$, where there is a loss of heat by convection; recall Equations (5.25)– (5.28). The numerical integration will take place for $0 \leq t \leq 30.0$ with the details $\Delta t = 0.01$, $\mathrm{Tol} = 1 \times 10^{-2}$ and $\mathrm{h_{max}} = 0.05$.

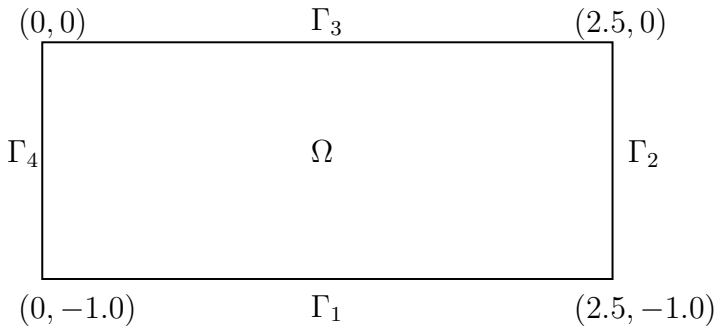

Figure 5.2: Domain and boundaries associated with the welding problem.

To apply test I, we apply the heat source Q, we take a fixed Gaussian-type function. Furthermore, to obtain more valuable information on the physical process under study, We consider the following interval $(0 < t \leq 10.0)$ for the heating stage and the interval $(10.0 < t \leq 30.0)$;

$$Q(x_1,x_2,t)=\begin{cases} Q^0\exp\left(-10\left(x_1-\left(x_1^0+v^0t\right)\right)^2-\left(x_2-x_2^0\right)^2\right)\left(1-e^{-5t}\right), & 0\le t\le 10.0,\\ 0, & 10.0<t\le 30.0,\end{cases} \tag{5.37}$$

with $Q^0=1.0$, $v^0=0.0$, $x_1^0=0.5$, and $x_2^0=-0.5$.

Finally, the values of dimensionless parameters are computed from the physical magnitudes of (Piekarska and Kubiak 2011; Piekarska and Kubiak 2013; Montalvo-Urquizo et al. 2013; Wu et al. 2021; Díaz Moreno et al. 2021):

$$\begin{gathered}\mathrm{Re}=200,\quad \mathrm{Gr}=10^{-8},\quad \mathrm{Da}=10^{-4},\quad \mathrm{Pe}=40,\quad \mathrm{Nu}=10,\quad \mathrm{Ste}=0.25,\\ c_S/c_L=0.75,\quad \lambda_S/\lambda_L=1.5,\quad \mathrm{F}=\mathrm{P}=\mathrm{B}=1.0,\quad \mathrm{M}=16.0,\\ \mathrm{n_b}=2.0,\quad \mathrm{n_f}=\mathrm{n_p}=1.43,\quad \mathrm{d_f}=\mathrm{d_p}=\mathrm{d_b}=2,\quad \kappa_\mathrm{f}=\kappa_\mathrm{p}=\kappa_\mathrm{b}=625,\\ \theta_{\mathrm{sa}}=0.4848,\quad \theta_{\mathrm{aa}}=0.5417,\quad \theta_{\mathrm{fa}}=0.5607,\quad \theta_{\mathrm{sf}}=0.4986,\quad \theta_{\mathrm{mf}}=0.4400,\quad \theta_{\mathrm{ff}}=0.3814,\\ \theta_{\mathrm{sp}}=0.4986,\quad \theta_{\mathrm{mp}}=0.4400,\quad \theta_{\mathrm{fp}}=0.3814,\quad \theta_{\mathrm{sb}}=0.3952,\quad \theta_{\mathrm{mb}}=0.2366,\quad \theta_{\mathrm{fb}}=0.0779,\\ \theta_{\mathrm{sm}}=0.2159,\quad \theta_{\mathrm{fm}}=0.0779\end{gathered} \tag{5.38}$$

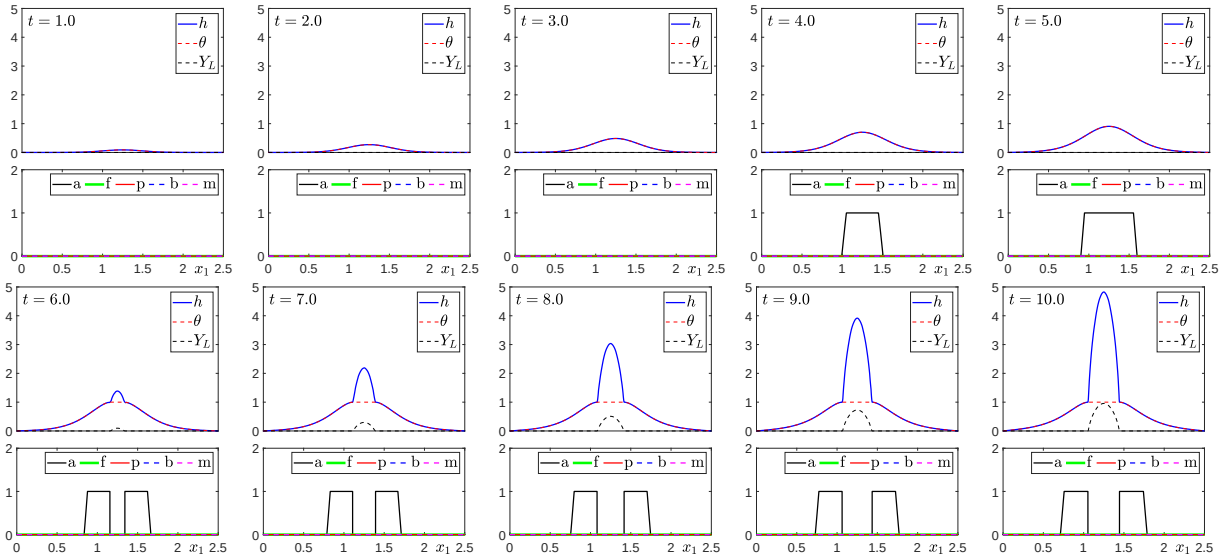

Figure 5.3: Heating stage of Test I, $t\le 10.0$, where the development of the austenite–a phase, takes place as time passes, and the enthalpy and temperature increase.

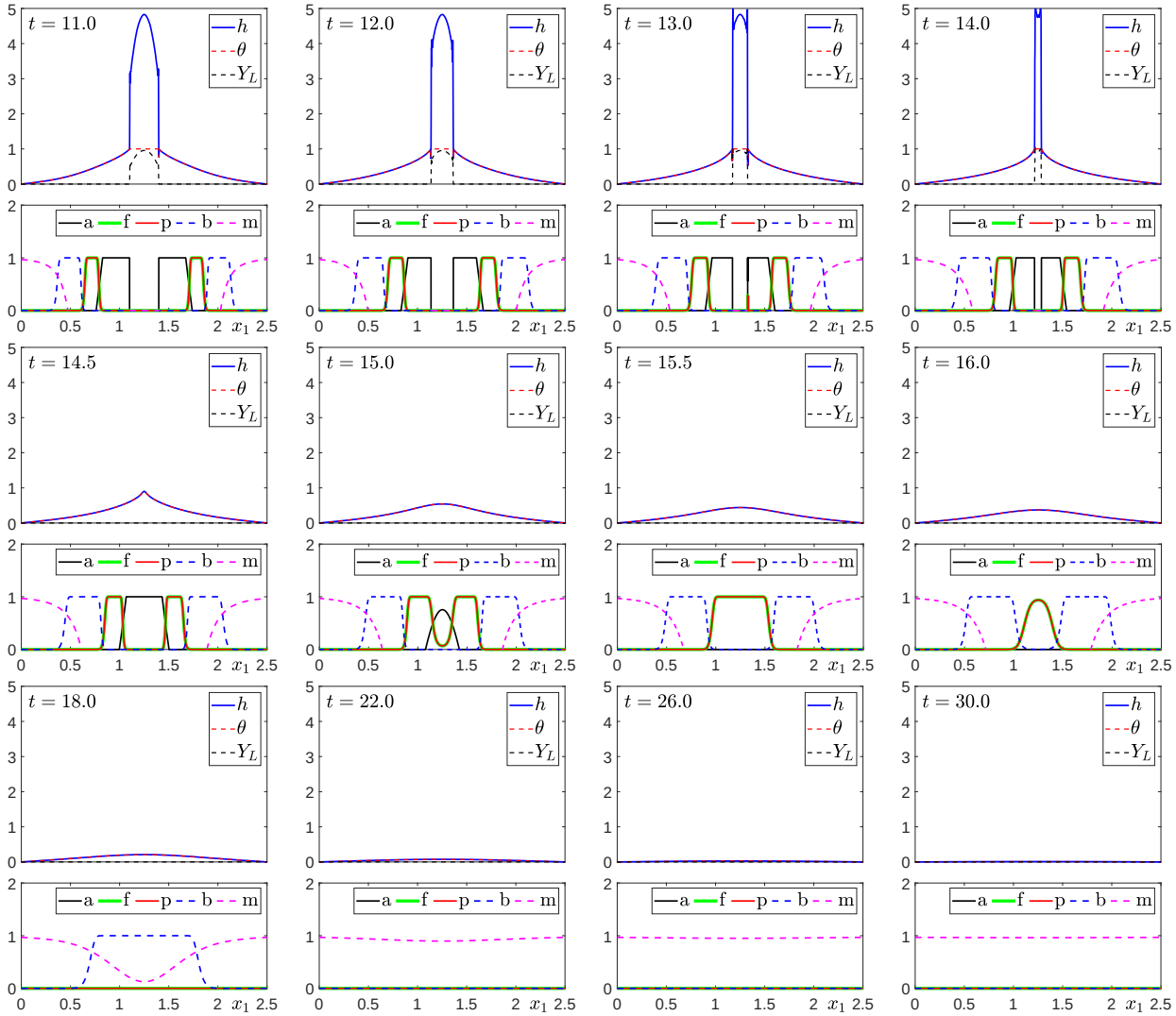

Figure 5.4: Cooling stage of Test I, $t > 10.0$, where the development of the ferrite–f, pearlite–p, bainite–b and martensite–m phases, takes place as time passes, and the enthalpy and temperature decrease.

In the Figure 5.3, during the heating stage, we can observe the development of austenite–a according to (5.36) and increase in enthalpy and temperature due to the application of the heat source. It is worth mentioning that when the steel reaches the liquid stage, neither austenite nor any steel-phase can occur.

On the other hand, during the cooling stage. In Figure 5.4, we can observe the development of the phases: ferrite–f, pearlite–p and bainite–b phases, according to the Johnson-Mehl-Avrami-Kolmogorov equations, we can also observe the stabilization of martensite b at $t \sim 30.0$ according to the Koistinen-Marburger equation. In addition, we observe the decrease in austenite–a as time passes. Its decrease is justified because part of the austenite created during the heating stage is transformed into ferrite, pearlite, bainite and/or martensite during the cooling stage.

5.3.2 Test II: Moving Gaussian-Type Heat Source

To apply test II, we apply the heat source Q, we take a Gaussian-type function moving from left to right with constant velocity v^0. Furthermore, to obtain more valuable information on the physical process under study. We consider the following interval $(0 < t \leq 1.0)$ for the heating stage and the interval $(1.0 < t \leq 5.0)$;

$$Q(x_1, x_2, t) = \begin{cases} Q^0 \exp\left(-100\left(x_1 - \left(x_1^0 + v^0 t\right)\right)^2 - 25\left(x_2 - x_2^0\right)^2\right)\left(1 - e^{-5t}\right), & 0 \leq t \leq 1.0, \\ 0, & 1.0 < t \leq 5.0, \end{cases} \tag{5.39}$$

with $Q^0 = 25.0$, $v^0 = 1.5$, $x_1^0 = 0.5$, and $x_2^0 = -0.5$.

Finally, the values of dimensionless parameters are computed from the physical magnitudes of (Piekarska and Kubiak 2011; Piekarska and Kubiak 2013; Montalvo-Urquizo et al. 2013; Wu et al. 2021; Díaz Moreno et al. 2021):

$$\begin{gathered} \mathrm{Re} = 200, \quad \mathrm{Gr} = 10^{-8}, \quad \mathrm{Da} = 10^{-4}, \quad \mathrm{Pe} = 40, \quad \mathrm{Nu} = 10, \quad \mathrm{Ste} = 0.25, \\ c_S/c_L = 0.75, \quad \lambda_S/\lambda_L = 1.5, \quad \mathrm{F} = \mathrm{P} = \mathrm{B} = 1.0, \quad \mathrm{M} = 16.0, \\ \mathrm{n_b} = 2.0, \quad \mathrm{n_f} = \mathrm{n_p} = 1.43, \quad \mathrm{d_f} = \mathrm{d_p} = \mathrm{d_b} = 2, \quad \kappa_\mathrm{f} = \kappa_\mathrm{p} = \kappa_\mathrm{b} = 625, \\ \theta_{\mathrm{sa}} = 0.4848, \quad \theta_{\mathrm{aa}} = 0.5417, \quad \theta_{\mathrm{fa}} = 0.5607, \quad \theta_{\mathrm{sf}} = 0.4986, \quad \theta_{\mathrm{mf}} = 0.4400, \quad \theta_{\mathrm{ff}} = 0.3814, \\ \theta_{\mathrm{sp}} = 0.4986, \quad \theta_{\mathrm{mp}} = 0.4400, \quad \theta_{\mathrm{fp}} = 0.3814, \quad \theta_{\mathrm{sb}} = 0.3952, \quad \theta_{\mathrm{mb}} = 0.2366, \quad \theta_{\mathrm{fb}} = 0.0779, \\ \theta_{\mathrm{sm}} = 0.2159, \quad \theta_{\mathrm{fm}} = 0.0779 \end{gathered} \tag{5.40}$$

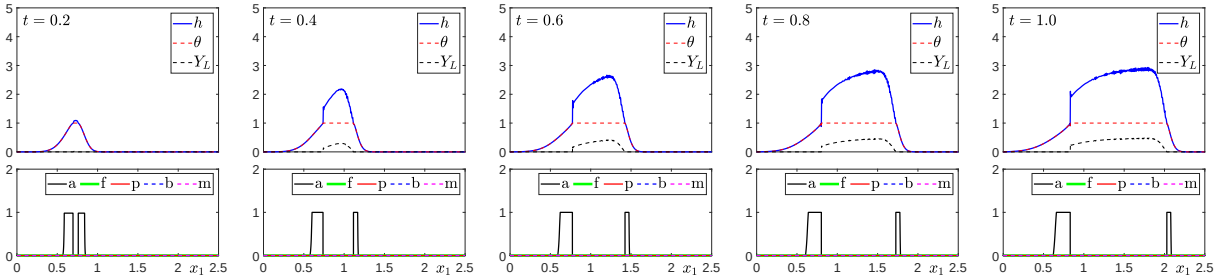

Figure 5.5: Heating stage of Test II, $t \leq 1.0$, where the development of the austenite–a phase, takes place as time passes, and the enthalpy and temperature increase.

In the Figure 5.5, during the heating stage, we can observe the development of austenite–a according to the indicated conditions and the Equation (5.36), neither austenite nor any other

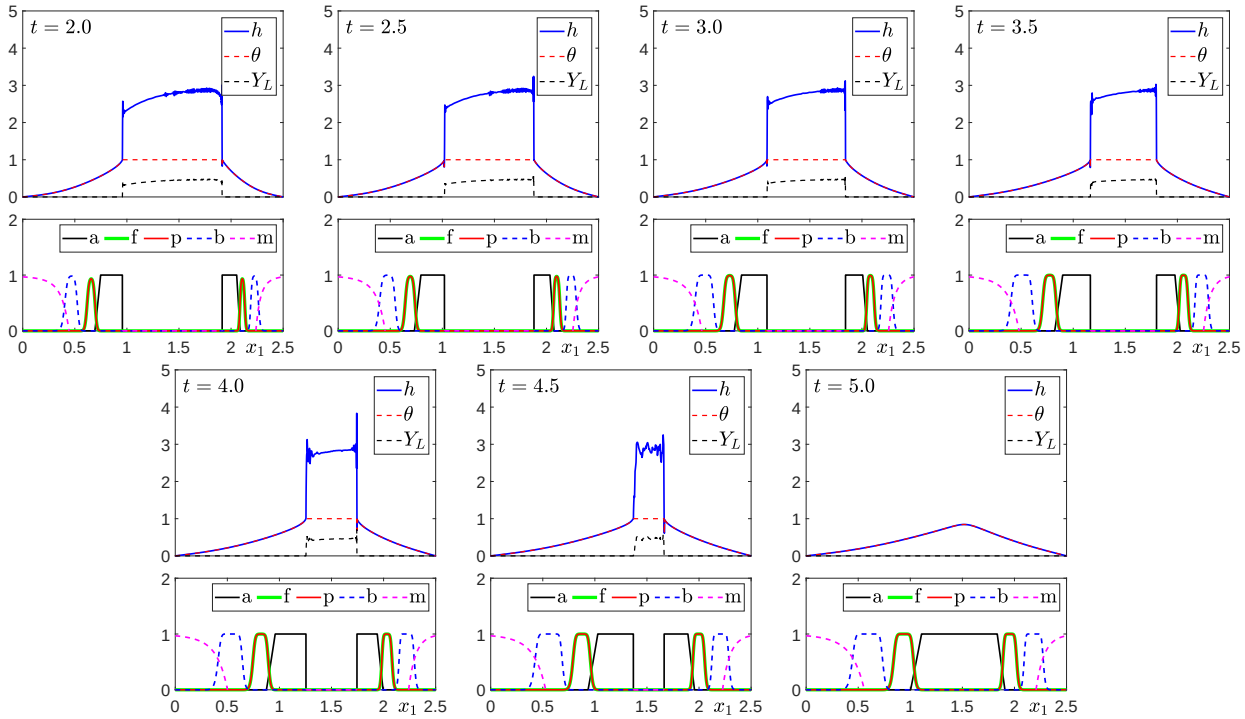

Figure 5.6: Cooling stage of Test II, $t > 1.0$, where the development of the ferrite–f, pearlite–p, bainite–b and martensite–m phases, takes place as time passes, and the enthalpy and temperature decrease.

steel-phase can occur when the steel reaches the liquid phases The peaks in the austenite curve are due to the nature of the mobile heat source and the Stefan number Ste = 0.25.

On the other hand, during the cooling stage, Figure 5.6, we can observe the development of the phases: ferrite–f, pearlite–p and bainite–b, according to the Johnson-Mehl-Avrami-Kolmogorov equations, we can also observe the development of martensite–m according to the Koistinen-Marburger equation. It is important to highlight that in the two stages developed, both in the heating stage and in the cooling stage, the enthalpy and temperature presented several oscillations, this was mainly due to the very low Stefan number Ste = 0.25 which caused the increase in the iterations necessary to solve the energy conservation equation, and also to the presence of the velocity of the heat source.

Chapter 6

Conclusions and Future Work

In the Chapter 2 we present the backbone of this thesis, that consists of the presentation of a new finite element method to solve thermal variables in welding problems. First, we define the enthalpy formulation for the energy equation, which is valid for the entire domain and allows the monitoring of phase interfaces by using the enthalpy variable. This chapter considers both models for non-isothermal and isothermal fusion problems, through their constitutive equations. The energy conservation equation is discretized using quadratic polynomials in space and a BDF2 type scheme for time, which has a higher order of convergence than the first-order schemes widely developed in the literature. This study also develops local anisotropic mesh adaptation. To solve the nonlinear equations, we developed a Newton-type method in two ways: first, considering the temperature θ as the main unknown variable (θ-Newton method), and second, considering enthalpy h as the main unknown variable (h-Newton method).

The h-Newton method above mentioned is the main new contribution of this chapter. It considers the two main cases found in the literature: isothermal and non-isothermal fusion models. This is a more viable option than the enthalpy-based methods presented in the literature, as demonstrated in (Nedjar 2002; Barral et al. 2003; Bermúdez and Otero 2004). This makes the h-Newton method a more robust method than temperature-based methods. Indeed, the numerical experiments carried out demonstrate that the h-Newton method converges in all the cases considered in our corresponding experiments. However, the θ-Newton method only works for non-isothermal fusion problems and fails unless the time step is very small or the temperature variation range ΔT is very large. For this reason, we have proven numerically that using enthalpy as the main study variable is much better from a computational point of view.

In the Chapter 3 we compare three different solution strategies for the nonlinear system of equations that arise in implicit enthalpy methods, namely (i) the h-Newton method (Freire-Torres et al. 2023), (ii) Nedjar's scheme (Nedjar 2002) and (iii) Bermúdez–Moreno algorithm (Bermúdez and Otero 2004; Bermúdez and Moreno 1981). One advantage of the h-Newton is that it is parameter-free, whereas Nedjar and Bermúdez–Moreno algorithms depend on user-defined parameters μ and ω, respectively.

The h-Newton results to be far more efficient, in terms of computation time, due to several reasons. First, it is well-known that its convergence rate is quadratic, so it requires very few iterations. In other nonlinear problems, this advantage is overcome by the fact that recomputing the Jacobian is expensive. However, this is not the case due to the introduction of Kirchhoff's variable (see Equation (3.5)). Therefore, we have a method that requires very few iterations at a very small cost. Nedjar's and Bermúdez–Moreno algorithms perform similarly, with the latter requiring less iterations if the parameter ω is close to the optimal. Both methods have only linear convergence, so they require far more iterations than the h-Newton method.

Furthermore, the h-Newton method seems much straightforward to implement, especially in comparison with Bermúdez–Moreno algorithm. The h-Newton method just sets the enthalpy as main unknown, since the latter univocally defines the state of the physical body, and applies a standard Newton method. Nedjar's does not iterate on the enthalpy, but on the temperature, and has to relax some linear expressions in order to avoid singularities at melting points. On the other hand, the Bermúdez–Moreno algorithm requires to introduce several operators that are tedious to manipulate and lack physical meaning.

An additional drawback of the Bermúdez–Moreno algorithm is that it is very sensitive to the choice of the parameter ω. There are some works (Parés et al. 2001) on the optimal choice; however, these add even more complexity to its implementation. The Nedjar method with $\mu = \min\{1,\ c_L/c_S\}$ seems to yield the best results. In contrast, as said before, the h-Newton is parameter-free.

In Chapter 4, we improve the model built in Chapter 2, incorporating the equations of conservation of mass and conservation of momentum (Navier-Stokes Equations) in order to solve the hydrodynamic variables: velocity $\mathbf{v}$ and pressure p, both in the pure liquid zone and in the so-called mushy zone. In the latter, to further improve the previously constructed model, we incorporate two important terms to the momentum conservation equation, the Darcy term that allows the simulation of fluids in porous media, and the Boussinesq term that allows the simulation of fluid movement through the phenomenon of natural convection.

Finally, in Chapter 5, we use the h-Newton method, to solve another important problem in metallurgy, the heat treatment. We use the theory presented in (Avrami 1939; Avrami 1940; Avrami 1941; Umemoto et al. 1982; Campbell et al. 1991; Fuhrmann et al. 1999; Pereloma and Edmonds 2012; Bhadeshia 2017; Barmak 2018; Murugaiyan et al. 2006; Avramov 2007; Donnay et al. 1996; Wu et al. 2021), to establish the equations that describe the various stages of steel transformation, both during the heating phase (appearance of austenite) and during the cooling phase (appearance of ferrite-pearlite, bainite, and martensite phases).

For future work, we will consider improving the developed model based on enthalpy for both isothermal and non-isothermal schemes. To this end, we can make the following contributions and optimizations to the model:

- Implement the density ρ as another state variable to calculate, according to the continuity equation.
- Coupling the family of established equations, the equations of electromagnetism (Maxwell's

equations), which will more accurately model the heating due to the Joule effect.

- Also couple to the family of established equations, the equations of the elasticity (Lamé-Hooke constitutive equations and equilibrium equations), to find the deformations caused by the change in temperature in the metal.
- Consider evaporation and radiation as phenomena linked to the energy conservation equation to improve the quantification of energy losses due to these phenomena.
- Furthermore, it is important to incorporate the effects of surface shear stresses between the various phases existing in the problem, e.g. Marangoni Effect.
- Improve the model to consider metal casting problems, with mass input and output over time.
- Finally, extend the developed enthalpy-based method for three-dimensional metallurgical problems.

References

Abbaschian, R. and R. Reed-Hill (2009). *Physical Metallurgy Principles - SI Version*. Cengage Learning. ISBN: 9781111805036.

Álvarez-Hostos, J. C., A. D. Bencomo, E. S. Puchi-Cabrera, V. D. Fachinotti, B. Tourn, and J. C. Salazar-Bove (Sept. 2019). "Implementation of a standard stream-upwind stabilization scheme in the element-free Galerkin based solution of advection-dominated heat transfer problems during solidification in direct chill casting processes". In: *Engineering Analysis with Boundary Elements* 106, pp. 170–181. ISSN: 09557997. DOI: 10.1016/j.enganabound.2019.05.008.

Anca, A., A. Cardona, J. Risso, and V. D. Fachinotti (Feb. 2011). "Finite element modeling of welding processes". In: *Applied Mathematical Modelling* 35 (2), pp. 688–707. ISSN: 0307904X. DOI: 10.1016/j.apm.2010.07.026.

Asociación Española de Metalurgia y Materiales (2023). *La metalurgia en la sociedad moderna*. Madrid: AIMME.

Atta, D. (2022). "Thermal Diffusion Responses in an Infinite Medium with a Spherical Cavity using the Atangana-Baleanu Fractional Operator". In: *Journal of Applied and Computational Mechanics* 8.4, pp. 1358–1369. ISSN: 2383-4536. DOI: 10.22055/jacm.2022.40318.3556. URL: https://jacm.scu.ac.ir/article_17514.html.

Atthey, D. R. (1975). "A finite difference scheme for melting problems". In: *J. Inst. Math. Appl.* 354.

Avrami, M. (Dec. 1939). "Kinetics of Phase Change. I General Theory". In: *The Journal of Chemical Physics* 7 (12), pp. 1103–1112. ISSN: 0021-9606. DOI: 10.1063/1.1750380.

– (Feb. 1940). "Kinetics of Phase Change. II Transformation-Time Relations for Random Distribution of Nuclei". In: *The Journal of Chemical Physics* 8 (2), pp. 212–224. ISSN: 0021-9606. DOI: 10.1063/1.1750631.

– (Feb. 1941). "Granulation, Phase Change, and Microstructure Kinetics of Phase Change. III". In: *The Journal of Chemical Physics* 9 (2), pp. 177–184. ISSN: 0021-9606. DOI: 10.1063/1.1750872.

Avramov, I. (June 2007). "Kinetics of distribution of infections in networks". In: *Physica A: Statistical Mechanics and its Applications* 379 (2), pp. 615–620. ISSN: 03784371. DOI: 10.1016/j.physa.2007.02.002.

Barbu, V. (Apr. 2021). "Boundary controllability of phase-transition region of a two-phase Stefan problem". In: *Systems and Control Letters* 150. ISSN: 01676911. DOI: 10.1016/j.sysconle.2021.104896.

Barmak, K. (Dec. 2018). "A Commentary on: "Reaction Kinetics in Processes of Nucleation and Growth"*". In: *Metallurgical and Materials Transactions B* 49 (6), pp. 3616–3680. ISSN: 1073-5615. DOI: 10.1007/s11663-010-9421-1.

Barral, P., A. Bermúdez, M. C. Muñiz, M. V. Otero, P. Quintela, and P. Salgado (2003). "Numerical simulation of some problems related to aluminium casting". In: *J. Mater. Process. Technol.* 142(2), pp. 383–399. DOI: 10.1016/S0924-0136(03)00602-2.

Bermúdez, A and C Moreno (1981). "Duality Methods for Solving Variational Inequalities". In: *Computers & Mathematics with Applications* 7, pp. 43–58.

Bermúdez, A and M. V. Otero (2004). "Numerical solution of a three-dimensional solidification problem in aluminium casting". In: *Finite Elements in Analysis and Design* 40, pp. 1885–1906. DOI: 10.1016/j.finel.2003.11.010. URL: www.elsevier.com/locate/finel.

Bhadeshia Harshad; Honeycombe, R. (2017). *Steels: Microstructure and Properties, Fourth Edition*. Fourth Edition. Elsevier Science and Technology Books, Inc. ISBN: 978-0-08-100270-4,9780081002728,0081002726.

Brandt, D. A. and J. C. Warner (2004). *Metallurgy Fundamentals*. Goodheart-Wilcox Publisher. ISBN: 1590703456,9781590703458.

Caldwell, J. and Y. Y. Kwan (Apr. 2004). "Numerical methods for one-dimensional Stefan problems". In: *Communications in Numerical Methods in Engineering* 20.7, pp. 535–545. ISSN: 10698299. DOI: 10.1002/cnm.691. (Visited on 07/18/2023).

Caldwell, J. and C.-C. Chan (Jan. 2000). "Spherical solidification by the enthalpy method and the heat balance integral method". In: *Applied Mathematical Modelling* 24.1, pp. 45–53. ISSN: 0307-904X. DOI: 10.1016/S0307-904X(99)00031-1. (Visited on 07/25/2023).

Campbell, P. C., E. B. Hawbolt, and J. K. Brimacombe (Nov. 1991). "Microstructural engineering applied to the controlled cooling of steel wire rod: Part II. Microstructural evolution and mechanical properties correlations". In: *Metallurgical Transactions A* 22 (11), pp. 2779–2790. ISSN: 0360-2133. DOI: 10.1007/BF02851372.

Carpio, J. and J. L. Prieto (May 2014). "An anisotropic, fully adaptive algorithm for the solution of convection-dominated equations with semi-Lagrangian schemes". In: *Computer Methods in Applied Mechanics and Engineering* 273, pp. 77–99. ISSN: 00457825. DOI: 10.1016/j.cma.2014.01.025.

Carpio, J., J. L. Prieto, and P. G. del Sastre (Mar. 2019). "An anisotropic adaptive, Lagrange-Galerkin numerical method for spray combustion". In: *Journal of Computational Physics* 381, pp. 246–274. ISSN: 10902716. DOI: 10.1016/j.jcp.2018.12.022.

Carpio, J., J. L. Prieto, and M. Vera (Feb. 2016). "A local anisotropic adaptive algorithm for the solution of low-Mach transient combustion problems". In: *Journal of Computational Physics* 306, pp. 19–42. ISSN: 10902716. DOI: 10.1016/j.jcp.2015.11.011.

Casella, E. and M. Giangi (2001). "An analytical and numerical study of the Stefan problem with convection by means of an enthalpy method". In: *Mathematical Methods in the Applied Sciences* 24.9, pp. 623–639. ISSN: 1099-1476. DOI: 10.1002/mma.233. (Visited on 07/14/2023).

Cho, J.-H and S.-J Na (2009). "Three-Dimensional Analysis of Molten Pool in GMA-Laser Hybrid Welding Analytical models of GMA and laser keyhole welding are merged to achieve the simulation of hybrid welding considering the multiple reflections of laser and the Fresnel absorption theory". In: *Welding Journal*.

Colera, M., J. Carpio, and R. Bermejo (Dec. 2020). "A nearly-conservative high-order Lagrange–Galerkin method for the resolution of scalar convection-dominated equations in non-divergence-free velocity fields". In: *Computer Methods in Applied Mechanics and Engineering* 372, p. 113366. ISSN: 0045-7825. DOI: https://doi.org/10.1016/j.cma.2020.113366. URL: https://www.sciencedirect.com/science/article/pii/S004578252030551X.

– (Apr. 2021). "A nearly-conservative, high-order, forward Lagrange–Galerkin method for the resolution of scalar hyperbolic conservation laws". In: *Computer Methods in Applied Mechanics and Engineering* 376, p. 113654. ISSN: 0045-7825. DOI: https://doi.org/10.1016/j.cma.2020.113654. URL: https://www.sciencedirect.com/science/article/pii/S0045782520308392.

– (Oct. 2022). "A nearly-conservative, high-order, forward Lagrange–Galerkin method for the resolution of compressible flows on unstructured triangular meshes". In: *Journal of Computational Physics* 467, p. 111471. ISSN: 0021-9991. DOI: https://doi.org/10.1016/j.jcp.2022.111471. URL: https://www.sciencedirect.com/science/article/pii/S0021999122005332.

Danaila, I., R. Moglan, F. Hecht, and S. L. Masson (Oct. 2014). "A Newton method with adaptive finite elements for solving phase-change problems with natural convection". In: *Journal of Computational Physics* 274, pp. 826–840. ISSN: 10902716. DOI: 10.1016/j.jcp.2014.06.036.

Davenport, E. S. and E. C. Bain (Dec. 1970). "Transformation of austenite at constant subcritical temperatures". In: *Metallurgical Transactions* 1 (12), pp. 3503–3530. ISSN: 0026-086X. DOI: 10.1007/BF03037892.

Dieter, G. E. (1988). *Mechanical Metallurgy*. 3rd edition. McGraw-Hill. ISBN: 007084187X.

Dolejší, V. and G. May (2022). *Anisotropic hp-Mesh Adaptation Methods: Theory, implementation and applications*. Nečas Center Series. Cham: Springer International Publishing. ISBN: 978-3-031-04278-2 978-3-031-04279-9. DOI: 10.1007/978-3-031-04279-9. (Visited on 10/19/2022).

Donnay, B, J Herman, V Leroy, B. Crm, U Lotter, R Grossterlinden, H Pircher, and T. Stahl (Jan. 1996). "Microstructure evolution of C-Mn steels in the hot deformation process". In: *2nd International Conference on Modeling of Metal Rolling Processes*.

Díaz Moreno, J. M., C. García Vázquez, M. T. González Montesinos, F. Ortegón Gallego, and G. Viglialoro (2021). "Industrial Steel Heat Treating: Numerical Simulation of Induction Heating and Aquaquenching Cooling with Mechanical Effects". In: *Mathematics* 9.11. ISSN: 2227-7390. DOI: 10.3390/math9111203. URL: https://www.mdpi.com/2227-7390/9/11/1203.

Díaz, J. M., C. García, M. T. González, F. Ortegón, and G. Viglialoro (Jan. 2012). "Mathematical modeling of heat treatment for a steering rack including mechanical effects". In: *Journal of Numerical Mathematics* 20 (3-4). ISSN: 1569-3953. DOI: 10.1515/jnum-2012-0011.

Easterling, K. E. (1992). *Introduction to the physical metallurgy of welding*. 2nd ed. Butterworth Heinemann. ISBN: 0750603941,9780750603942.

Embury, D. (2012). "The formation of pearlite in steels". In: Elsevier, pp. 276–310. DOI: 10.1533/9780857096104.2.276.

Encyclopaedia Britannica (Oct. 2023a). *Casting*. URL: https://www.britannica.com/science/metallurgy/Casting.

Encyclopaedia Britannica (Oct. 2023b). *Heat Treatment*. URL: https://www.britannica.com/technology/heat-treating.
– (Oct. 2023c). *Steel*. URL: https://www.britannica.com/technology/steel.
– (Oct. 2023d). *Steel*. URL: https://www.britannica.com/technology/austenite.
– (Oct. 2023e). *Welding*. URL: https://www.britannica.com/technology/welding.
Esen, A and S Kutluay (Jan. 2004). "A numerical solution of the Stefan problem with a Neumann-type boundary condition by enthalpy method". In: *Applied Mathematics and Computation* 148.2, pp. 321–329. ISSN: 00963003. DOI: 10.1016/S0096-3003(02)00846-9. (Visited on 07/18/2023).
Freire-Torres, M. and J. Carpio (2022). "Contribución al modelado matemático y la simulación numérica de procesos de soldadura". In: Universidad Nacional de Educación a Distancia (España). DOI: 10.5944/bicim2022.306.
– (2023). "Contribution to Mathematical Modeling and Numerical Simulation of Welding Processes". In: Springer International Publishing, pp. 24–29. DOI: 10.1007/978-3-031-38563-6_4.
Freire-Torres, M., M. Colera, and J. Carpio (July 2023). "Numerical Solution of Thermal Phenomena in Welding Problems". In: *Mathematics* 11 (13), p. 3009. ISSN: 2227-7390. DOI: 10.3390/math11133009.
Fried, M. and A. Veeser (2001). "Simulation and Numerical Analysis of Dendritic Growth". In: *Ergodic Theory, Analysis, and Efficient Simulation of Dynamical Systems*. Ed. by B. Fiedler. Berlin, Heidelberg: Springer, pp. 225–252. ISBN: 978-3-642-56589-2. DOI: 10.1007/978-3-642-56589-2_10.
Fuhrmann, J., D. Hömberg, and M. Uhle (Sept. 1999). "Numerical simulation of induction hardening of steel". In: *COMPEL - The international journal for computation and mathematics in electrical and electronic engineering* 18 (3), pp. 482–493. ISSN: 0332-1649. DOI: 10.1108/03321649910275161.
Garcia-Mateo, C. and F. Caballero (2014). "Advanced High Strength Bainitic Steels". In: Elsevier, pp. 165–190. DOI: 10.1016/B978-0-08-096532-1.00114-X.
Glowinski, R and O Pironneau (1979). "Numerische Mathematik On a Mixed Finite Element Approximation of the Stokes Problem (I) Convergence of the Approximate Solutions". In: *Numer. Math* 33, pp. 397–424.
Griewank, P. J. and D. Notz (2013). "Insights into brine dynamics and sea ice desalination from a 1-D model study of gravity drainage". In: *Journal of Geophysical Research: Oceans* 118.7, pp. 3370–3386. ISSN: 2169-9291. DOI: 10.1002/jgrc.20247. (Visited on 07/21/2023).
Gupta, S. C., ed. (Jan. 2018). *The Classical Stefan Problem*. 2nd. Amsterdam: Elsevier. ISBN: 978-0-444-63581-5. DOI: 10.1016/B978-0-444-63581-5.09984-X. (Visited on 07/25/2023).
Hecht, F. (2006). "BAMG: Bidimensional Anisotropic Mesh Generator". In: URL: www.freefem.org/ff++.
Hutter, K., A. Zryd, and H. Röthlisberger (1990). "On the Numerical Solution of Stefan Problems in Temperate Ice". In: *Journal of Glaciology* 36.122, pp. 41–48. ISSN: 0022-1430, 1727-5652. DOI: 10.3189/S0022143000005530. (Visited on 07/21/2023).
Instituto Nacional de Ciencia y Tecnología Metalúrgicas (2022). *La investigación metalúrgica en España*. Madrid: INCyTM.

Javierre, E., C. Vuik, F. J. Vermolen, and S. van der Zwaag (Aug. 2006). "A comparison of numerical models for one-dimensional Stefan problems". In: *Journal of Computational and Applied Mathematics* 192.2, pp. 445–459. ISSN: 0377-0427. DOI: 10.1016/j.cam.2005.04.062. (Visited on 07/21/2023).

Kamenomostskaya, S. L. (1961). "On the stefan problem". In: *Mat. Sbornik*, pp. 489–514.

Karkhin, V. A. (2018). *Engineering Materials Thermal Processes in Welding*. Springer. URL: http://www.springer.com/series/4288.

Koistinen, D. and R. Marburger (Jan. 1959). "A general equation prescribing the extent of the austenite-martensite transformation in pure iron-carbon alloys and plain carbon steels". In: *Acta Metallurgica* 7 (1), pp. 59–60. ISSN: 00016160. DOI: 10.1016/0001-6160(59)90170-1.

Kubiak, M. and W. Piekarska (Aug. 2016). "Comprehensive model of thermal phenomena and phase transformations in laser welding process". In: *Computers and Structures* 172, pp. 29–39. ISSN: 00457949. DOI: 10.1016/j.compstruc.2016.05.014.

Kutluay, S., A. R. Bahadir, and A. Özdeş (June 1997). "The numerical solution of one-phase classical Stefan problem". In: *Journal of Computational and Applied Mathematics* 81.1, pp. 135–144. ISSN: 0377-0427. DOI: 10.1016/S0377-0427(97)00034-4. (Visited on 07/25/2023).

Kutluay, S and A Esen (Feb. 2004). "An isotherm migration formulation for one-phase Stefan problem with a time dependent Neumann condition". In: *Applied Mathematics and Computation* 150.1, pp. 59–67. ISSN: 0096-3003. DOI: 10.1016/S0096-3003(03)00197-8. (Visited on 07/21/2023).

Leblond, J. and J. Devaux (Jan. 1984). "A new kinetic model for anisothermal metallurgical transformations in steels including effect of austenite grain size". In: *Acta Metallurgica* 32 (1), pp. 137–146. ISSN: 00016160. DOI: 10.1016/0001-6160(84)90211-6.

McBride, B. J., M. J. Zehe, and S. Gordon (2002). *NASA Glenn Coefficients for Calculating Thermodynamic Properties of Individual Species*. Tech. rep. NASA/TP-2002-211556. NASA. URL: https://ntrs.nasa.gov/api/citations/20020085330/downloads/20020085330.pdf.

Meirmanov, M. A. (1992). "The Stefan Problem". In: *Walter de Gruyter Expositions in Mathematics, Berlin*.

Mitchell, S. L. and M. Vynnycky (July 2014). "On the numerical solution of two-phase Stefan problems with heat-flux boundary conditions". In: *Journal of Computational and Applied Mathematics* 264, pp. 49–64. ISSN: 0377-0427. DOI: 10.1016/j.cam.2014.01.003. (Visited on 07/14/2023).

Mitchell, S. L., M. Vynnycky, I. G. Gusev, and S. S. Sazhin (July 2011). "An accurate numerical solution for the transient heating of an evaporating spherical droplet". In: *Applied Mathematics and Computation* 217.22, pp. 9219–9233. ISSN: 0096-3003. DOI: 10.1016/j.amc.2011.03.161. (Visited on 07/21/2023).

Montalvo-Urquizo, J., Q. Liu, and A. Schmidt (Nov. 2013). "Simulation of quenching involved in induction hardening including mechanical effects". In: *Computational Materials Science* 79, pp. 639–649. ISSN: 09270256. DOI: 10.1016/j.commatsci.2013.06.058.

"11 - Steels for aircraft structures" (2012). In: *Introduction to Aerospace Materials*. Ed. by A. P. Mouritz. Woodhead Publishing, pp. 232–250. ISBN: 978-1-85573-946-8. DOI: https://doi.org/10.1533/9780857095152.232. URL: https://www.sciencedirect.com/science/article/pii/B978185573946850011X.

Muelas, Á., J. Carpio, J. Ballester, A. L. Sánchez, and F. A. Williams (July 2020). "Pyrolysis effects during high-temperature vaporization of alkane droplets". In: *Combustion and Flame* 217, pp. 38–47. ISSN: 0010-2180. DOI: 10.1016/j.combustflame.2020.03.033. (Visited on 07/25/2023).

Murugaiyan, A., A. S. Podder, A. Pandit, S. Chandra, D. Bhattacharjee, and R. K. Ray (2006). "Phase Transformations in Two C–Mn–Si–Cr Dual Phase Steels". In: *ISIJ International* 46 (10), pp. 1489–1494. ISSN: 0915-1559. DOI: 10.2355/isijinternational.46.1489.

Nazzi Ehms, J. H., R. De Césaro Oliveski, L. A. Oliveira Rocha, C. Biserni, and M. Garai (Jan. 2019). "Fixed Grid Numerical Models for Solidification and Melting of Phase Change Materials (PCMs)". In: *Applied Sciences* 9.20, p. 4334. ISSN: 2076-3417. DOI: 10.3390/app9204334. (Visited on 07/21/2023).

Nedjar, B (2002). "An enthalpy-based finite element method for nonlinear heat problems involving phase change". In: *Computers & Structures* 80(1), pp. 9–21. DOI: 10.1016/S0045-7949(01)00165-1. URL: www.elsevier.com/locate/compstruc.

Oleinik, O. A. (1960). "A method of solution of the general Stefan problem". In: *Soviet Math. Doklady* 1, pp. 1350–1354.

Onyejekwe, O. O. and O. N. Onyejekwe (Oct. 2011). "Numerical solutions of the one-phase classical Stefan problem using an enthalpy green element formulation". In: *Advances in Engineering Software* 42.10, pp. 743–749. ISSN: 09659978. DOI: 10.1016/j.advengsoft.2011.05.012. (Visited on 07/18/2023).

Özisik, M. N. (1989). "Boundary Value Problems of Heat Conduction". In: *Dover Publications Inc., New York*.

Parés, C., M. Castro, and J. Macías (July 2002). "On the convergence of the Bermúdez-Moreno algorithm with constant parameters". In: *Numerische Mathematik* 92.1, pp. 113–128. ISSN: 0945-3245. DOI: 10.1007/s002110100352. (Visited on 01/14/2022).

Parés, C., J. Macías, and M. Castro (2001). "Duality methods with an automatic choice of parameters. Application to shallow water equations in conservative form". In: *Numerische Mathematik* 89, pp. 161–189. DOI: 10.1007/s002110000219.

Pegler, S. S. and M. S. D. Wykes (2021). "The convective Stefan problem: shaping under natural convection". In: *Journal of Fluid Mechanics* 915. ISSN: 14697645. DOI: 10.1017/jfm.2021.86.

Pereloma, E. and D. Edmonds (2012). *Phase transformations in steels: Volume 1: Fundamentals and diffusion-controlled transformations*. Woodhead Publishing. ISBN: 184569970X.

Piekarska, W. and M. Kubiak (Nov. 2011). "Three-dimensional model for numerical analysis of thermal phenomena in laser-arc hybrid welding process". In: *International Journal of Heat and Mass Transfer* 54 (23-24), pp. 4966–4974. ISSN: 00179310. DOI: 10.1016/j.ijheatmasstransfer.2011.07.010.

– (Feb. 2013). "Modeling of thermal phenomena in single laser beam and laser-arc hybrid welding processes using projection method". In: *Applied Mathematical Modelling* 37 (4), pp. 2051–2062. ISSN: 0307904X. DOI: 10.1016/j.apm.2012.04.052.

Piekarska, W., M. Kubiak, and A. Bokota (Jan. 2011). "Numerical Simulation of Thermal Phenomena and Phase Transformations in Laser-Arc Hybrid Welded Joints". In: *Archives of Metallurgy and Materials* 56 (2). ISSN: 1733-3490. DOI: 10.2478/v10172-011-0044-6.

Piqueras, M. A., R. Company, and L. Jódar (Sept. 2020). "Solving two-phase freezing Stefan problems: Stability and monotonicity". In: *Mathematical Methods in the Applied Sciences*

43.14, pp. 7948–7960. ISSN: 0170-4214, 1099-1476. DOI: 10.1002/mma.5787. (Visited on 07/18/2023).

Prakash, S. A., C. Hariharan, R. Arivazhagan, R. Sheeja, V. A. A. Raj, and R. Velraj (Apr. 2021). "Review on numerical algorithms for melting and solidification studies and their implementation in general purpose computational fluid dynamic software". In: *Journal of Energy Storage* 36, p. 102341. ISSN: 2352152X. DOI: 10.1016/j.est.2021.102341. (Visited on 07/21/2023).

Pudjaprasetya, D. T. S. (June 2013). "Godunov Method for Stefan Problems with Enthalpy Formulations". In: *East Asian Journal on Applied Mathematics* 3.2, pp. 107–119. ISSN: 2079-7362, 2079-7370. DOI: 10.4208/eajam.030513.200513a. (Visited on 07/21/2023).

R.W. Cahn Kazuhiro Hono, P. H. (1996a). *Physical Metallurgy*. 4th, rev. and enhanced ed. Vol. Volume 1. Three Volume Set. North-Holland. ISBN: 9780444898753,0444898751.

– (1996b). *Physical Metallurgy*. 4th, rev. and enhanced ed. Vol. Volume 2. Three Volume Set. North-Holland. ISBN: 9780444898753,0444898751.

– (1996c). *Physical Metallurgy*. 4th, rev. and enhanced ed. Vol. Volume 3. Three Volume Set. North-Holland. ISBN: 9780444898753,0444898751.

Rakotondrandisa, A., G. Sadaka, and I. Danaila (2020). "A finite-element toolbox for the simulation of solid-liquid phase-change systems with natural convection". In: *Computer Physics Communications* 253, p. 107188. DOI: 10.17632/phby62rhgv.1. URL: http://dx.doi.org/10.17632/phby62rhgv.1.

Seetharaman, S. (2005). *Fundamentals of Metallurgy*. Woodhead Publishing Ltd. ISBN: 1855739275,9781855739277,9781845690946.

Shibahara, M. and S. N. Atluri (June 2011). "The meshless local Petrov-Galerkin method for the analysis of heat conduction due to a moving heat source, in welding". In: *International Journal of Thermal Sciences* 50 (6), pp. 984–992. ISSN: 12900729. DOI: 10.1016/j.ijthermalsci.2010.12.012.

Shu, Y., J. Li, and C. Zhang (Dec. 2020). "A local and parallel Uzawa finite element method for the generalized Navier-Stokes equations". In: *Applied Mathematics and Computation* 387. ISSN: 00963003. DOI: 10.1016/j.amc.2019.124671.

Sleptsov, S. D., N. A. Rubtsov, and N. A. Savvinova (Nov. 2018). "Simulation of ice melting in a single-phase statement of the Stefan problem". In: *Journal of Physics: Conference Series* 1105, p. 012145. ISSN: 1742-6588, 1742-6596. DOI: 10.1088/1742-6596/1105/1/012145. (Visited on 07/21/2023).

Smallman, R. and R. Bishop (1999). "Strengthening and toughening". In: Elsevier, pp. 259–296. DOI: 10.1016/B978-075064564-5/50008-2.

Son, J. H. and I. S. Park (Mar. 2021). "Temperature changes around interface cells in a one-dimensional Stefan condensation problem using four well-known phase-change models". In: *International Journal of Thermal Sciences* 161. ISSN: 12900729. DOI: 10.1016/j.ijthermalsci.2020.106718.

Tarwidi, D. (Mar. 2019). "An enthalpy-based finite element method for solving two-phase Stefan problem". In: *Indonesian Journal on Computing (Indo-JC)* 4.1, p. 43. ISSN: 2460-9056, 2460-9234. DOI: 10.21108/INDOJC.2019.4.1.252. (Visited on 07/18/2023).

Turichin, G., D. Mukin, E. Valdaytseva, and M. Sannikov (2022). "Influence of Latent Heat of Fusion on the Melt Pool Shape and Size in the Direct Laser Deposition Process". In: *Materials*

15.23. ISSN: 1996-1944. DOI: 10.3390/ma15238349. URL: https://www.mdpi.com/1996-1944/15/23/8349.

Umemoto, M., N. Nishioka, and I. Tamura (1982). "Prediction of Hardenability from Isothermal Transformation Diagrams". In: *Transactions of the Iron and Steel Institute of Japan* 22 (8), pp. 629–636. ISSN: 0021-1583. DOI: 10.2355/isijinternational1966.22.629.

Voller, V. R. (Jan. 1990). "Fast implicit finite-difference method for the analysis of phase change problems". In: *Numerical Heat Transfer, Part B: Fundamentals* 17.2, pp. 155–169. ISSN: 1040-7790, 1521-0626. DOI: 10.1080/10407799008961737. (Visited on 07/21/2023).

Voller, V. R., C. R. Swaminathan, and B. G. Thomas (Sept. 1990). "Fixed grid techniques for phase change problems: A review". In: *International Journal for Numerical Methods in Engineering* 30.4, pp. 875–898. ISSN: 0029-5981, 1097-0207. DOI: 10.1002/nme.1620300419. (Visited on 07/18/2023).

Voller, V. and M. Cross (Mar. 1981). "Accurate solutions of moving boundary problems using the enthalpy method". In: *International Journal of Heat and Mass Transfer* 24.3, pp. 545–556. ISSN: 00179310. DOI: 10.1016/0017-9310(81)90062-4. (Visited on 07/18/2023).

Vuik, C and C Cuvelier (June 1985). "Numerical solution of an etching problem". In: *Journal of Computational Physics* 59.2, pp. 247–263. ISSN: 0021-9991. DOI: 10.1016/0021-9991(85)90145-7. (Visited on 07/21/2023).

Walker, H. F. and P. Ni (Jan. 2011). "Anderson Acceleration for Fixed-Point Iterations". In: *SIAM Journal on Numerical Analysis* 49.4, pp. 1715–1735. ISSN: 0036-1429, 1095-7170. DOI: 10.1137/10078356X. (Visited on 01/07/2021).

Waters, L. K., G. J. Fix, and C. L. Cox (Oct. 2004). "The method of Glowinski and Pironneau for the unsteady stokes problem". In: *Computers and Mathematics with Applications* 48 (7-8), pp. 1191–1211. ISSN: 08981221. DOI: 10.1016/j.camwa.2004.10.015.

White, E. R. (1982). "An enthalpy formulation of the Stefan problem". In: *SIAM J. Numer. Anal.* 19(6), pp. 1129–1157. DOI: 10.1137/0719082.

Wu, J., H. Zhang, Y. Feng, and B. Luo (2018). "3D Multiphysical Modelling of Fluid Dynamics and Mass Transfer in Laser Welding of Dissimilar Materials". In: *Metals* 8.6. ISSN: 2075-4701. DOI: 10.3390/met8060443. URL: https://www.mdpi.com/2075-4701/8/6/443.

Wu, L., K. Liu, and Y. Zhou (Dec. 2021). "The Kinetics of Phase Transition of Austenite to Ferrite in Medium-Carbon Microalloy Steel". In: *Metals* 11 (12), p. 1986. ISSN: 2075-4701. DOI: 10.3390/met11121986.

Zhou, J. and H. L. Tsai (Aug. 2008). "Modeling of transport phenomena in hybrid laser-MIG keyhole welding". In: *International Journal of Heat and Mass Transfer* 51 (17-18), pp. 4353–4366. ISSN: 00179310. DOI: 10.1016/j.ijheatmasstransfer.2008.02.011.